Adam Mickiewicz University

Faculty of Physics

PhD thesis

Investigation of spin dynamics in planar magnonic devices

M.Sc. Mykhaylo L. Sokolovskyy

Supervisor:
dr hab. Maciej Krawczyk
Adam Mickiewicz University

Co-Supervisor:
prof. Doctor of Sciences Andriy M. Kuchko
Donetsk National University

Poznań 2012

To my uncle Mikhail U. Khait,
for helping me to realize
my own potential but most of
all for always being my friend

Abstract

Much attention in the field of electromagnetism has been paid recently to the theory of wave propagation in structures known as *electromagnetic metamaterials*. The interest in these materials is raised by the discovered possibility of modeling their unusual properties by controlling the geometry and the structure of the constituent materials. A metamaterial is composed of conventional materials; the prefix "meta" refers to the higher level of its structural organization. The research in metamaterials was initiated by Veselago, whose pioneer study [V. G. Veselago, Sov. Phys. Usp. **10**, 509 (1968)] presents a systematic theoretical development of the concept of materials in which both the permeability and the permittivity have negative values. Negative refractive indices occur in the frequency range in which the real parts of both the permittivity and the permeability are negative; this, however, is not a rigorously necessary condition.

From the point of view of technological applications hopes are placed on structures referred to as *bandgap metamaterials*, the properties of which are periodically modulated in space; these metamaterials seem very promising because of the possibility of tuning their band structure. For example, in the artificial materials known as *photonic crystals* the refractive index is modulated with a periodicity comparable to the wavelength of electromagnetic waves. Characteristic of periodic structures is the presence of bandgaps, or forbidden frequency ranges for propagating waves, in their spectrum. Periodically modulated magnetic materials have been shown to form *magnonic crystals*, a magnetic counterpart of photonic crystals with spin waves acting as information carriers. Photonic crystals are better studied and have more technological applications than magnonic crystals. However, the latter are better fit for miniaturization, since the wavelength of spin waves is several orders of magnitude shorter than that of electromagnetic waves of the same frequency.

The spectrum of a magnonic crystal, as that of any other system with a discrete translational symmetry, shows bandgaps, in this case referred to as magnonic bandgaps, in which no magnonic states are allowed to occur. Such bandgaps have been very recently observed in experimental studies using Brillouin light scattering spectroscopy [S. Tacchi *et al.*, Phys. Rev. B **82**, 024401 (2010); S. Tacchi *et al.*, Phys. Rev. B **82**, 184408 (2010)], time-resolved scanning Kerr microscopy [V. V. Kruglyak *et al.*, Phys. Rev. Lett. **104**, 027201 (2010)] and transmission measurements [A. V. Chumak *et al.*, Appl. Phys. Lett. **94**, 172511 (2009)].

The concept of magnonic crystal was first proposed in [J. O. Vasseur *et al.*, Phys. Rev. B **54**, 1043 (1996)], a study of a periodic array of ferromagnetic cylindrical rods embedded in a magnetic matrix. The theory of such systems was developed in later publications,

such as [M. Krawczyk and H. Puszkarski, Acta Phys. Pol. A **93**, 805 (1998); H. Puszkarski and M. Krawczyk, Solid State Phenom. **94**, 125 (2003)]. In these papers the position and width of bandgaps in the spin-wave spectrum were investigated versus the period of the structure and the contrast, or degree of modulation, of magnetic parameters. The depth of modulation of the exchange constant was found to have a drastic effect on the position and width of the bandgaps.

Magnonic devices with a planar geometry, ideally made of a single magnetic material, are the most advantageous from the point of view of fabrication and practical applications. However, the spin dynamics in such structures is poorly investigated due to mathematical problems related to the confined geometry of the sample. One of the challenges in the calculation of the spin-wave spectrum is the incorporation of the magnetostatic field. The Green's function formalism has proved suitable for its treatment. For example, in the theory of dispersion characteristics of dipolar-exchange spin waves in planar one-dimensional periodic structures based on thin ferromagnetic films with an array of metallic strips on its surface, developed in [N. Y. Grigorieva and B. A. Kalinikos, Tech. Phys. **54**, 1196 (2009)], the Green's function method was employed in the calculation of the dipolar field. The spin-wave spectrum of a planar array of interacting submicron square magnetic dots was calculated by means of the averaged Green's function of the demagnetizing field and measured by the Brillouin light scattering technique in [S. Tacchi *et al.*, Phys. Rev. B **82**, 024401 (2010)].

A popular analytical method of investigating the band structure of two- and three-dimensional periodic systems is the plane wave method, successfully adapted for and applied to electronic [T. Maehira *et al.*, Phys. Rev. Lett. **90**, 207007 (2003); M. Topsakal and S. Ciraci, Phys. Rev. B **85**, 045121 (2012)], photonic [J. Joannopoulos, *Photonic Crystals: Molding the Flow of Light* (Princeton University Press, 2008)], phononic [T.-T. Wu, Z.-G. Huang, and S. Lin, Phys. Rev. B **69**, 094301 (2004); S.-C. S. Lin and T. J. Huang, Phys. Rev. B **83**, 174303 (2011)] and magnonic crystals [H. Puszkarski and M. Krawczyk, Solid State Phenom. **94**, 125 (2003); M. Krawczyk and H. Puszkarski, Phys. Rev. B **77**, 054437 (2008)]. Following the main idea of the plane wave method, the equation of motion for a periodic structure is transformed into the reciprocal space with the use of the Fourier transformation and Bloch's theorem. The resulting eigenvalue problem can be solved by standard numerical routines, and its solution yields eigenfrequencies that form the band structure of the considered crystal.

Only the dynamic component of the demagnetizing field has been taken into account in the plane wave method so far (see, e.g., [H. Puszkarski and M. Krawczyk, Solid State Phenom. **94**, 125 (2003); M. Krawczyk and H. Puszkarski, Phys. Rev. B **77**, 054437 (2008); M. Krawczyk *et al.*, J. Appl. Phys. **108**, 093909 (2010)]). One of the

main objectives of this thesis is to adapt the plane wave method for the calculation of the magnonic band structure in thin magnonic crystals by taking into account the nonuniformity of the total magnetostatic field in the system. This task has been done in three stages: 1) the magnetostatic field has been calculated analytically for the most general case of a two-dimensional magnonic crystal with a planar geometry; 2) with several approximations used, the calculation results have been implemented in the equation of motion for magnetic systems; 3) the final eigenvalue problem has been obtained and solved by using appropriate numerical routines. Thus, the plane wave method has been adapted to the investigation of the spin-wave spectrum of magnonic crystals with a planar geometry in the mixed exchange-dipolar regime in which the exchange and magnetostatic energies are comparable, as well as in regimes in which one of them predominates.

Also problematic in the plane wave method is the lack of convergence of solutions of the eigenvalue problem in the case of a magnonic crystal with nonmagnetic inclusions. The problem stems from the very formulation of the equation of motion for inhomogeneous media. The equation of motion describes the dynamics of the magnetization vector in magnetic materials; in nonmagnetic media the magnetization is zero, and the equation becomes undefined. This implies the occurrence of nonphysical solutions, describing the dynamic components of the magnetization vector in the nonmagnetic material, in the total set of solutions. A simple method that allows to overcome this problem, inherent to the use of the plane wave method for calculating the spin-wave spectrum of planar magnonic crystals, has been proposed and tested in this thesis. The method is based on the idea of replacing the nonmagnetic inclusions with an artificial material in which the value of saturation magnetization is ten times lower than in the bulk magnetic medium. This allows to reproduce the magnitude of the demagnetizing field within the structure with an error of less than 10%. Other major assumptions related to the magnetostatic field and used in the calculations have been analyzed and discussed in detail in the present dissertation.

The improved plane wave method has been tested on many examples of one- and two-dimensional planar periodic structures, with the results compared to various experimental data. For example, in a one-dimensional magnonic crystal composed of alternate permalloy and cobalt nanostripes in direct contact forming a periodic structure with a period of 500 nm the observed spin waves have been verified to be of magnetostatic nature. The magnetostatic coupling of edge modes in square antidot lattice structures, represented by a homogeneous magnetic film with nanoholes periodically drilled on the surface, has been found to create minibands with strikingly large propagation velocities. This opens up interesting vistas in the field of nanoscale magnonic devices.

An important role in the formation of the band structure of a planar magnonic crystal is played by the boundary conditions on its external surfaces. One of the ways of controlling these boundary conditions is to use substrates or overlayers of different types, e.g. metallic, dielectric etc. In this thesis the plane wave method has been adapted for the calculation of the spin-wave spectrum of thin magnonic crystals with a metallic screen on top. A significant increase in group velocity of the spin waves and a shift of the first bandgap to higher frequencies have been observed in the considered structures. These features could be exploited in magnonic devices based on the phase shift of spin waves, for example, in a spin-wave Mach-Zehnder interferometer.

In magnetically ordered materials a fundamental role is played by the exchange interactions. The derivation of the exchange field in a homogeneous ferromagnetic material in the microscopic models can be found in a number of textbooks. Following those well-known ideas, this dissertation presents the derivation of the exchange field in composite materials with two or more ferromagnetic constituent materials in direct contact in the linear approximation. For large lattice constants the magnonic band structure proves independent of the formulation used. This is due to the predomination of the magnetostatic interactions over the exchange ones. The situation changes in the range of small lattice constants, in which, depending on the form of the exchange field, the bandgap can occur or not in the magnonic band structure. As shown by numerical calculations, various formulations of the exchange field are closely related to the boundary conditions at the interfaces between two ferromagnetic materials. Further investigation is necessary to establish the proper form of the exchange field fulfilling the physical boundary conditions imposed on the dynamic components of the magnetization vector in magnonic crystals.

The continued search for alternative logic paradigms beyond those based on semiconductors has led to the suggestion that propagating spin waves could provide a basis of logic devices. The Mach-Zehnder interferometer has been used as the basic element of logic gates in optics. A simple spin-wave interferometer of the Mach-Zehnder type employing a local nonuniformity of the effective magnetic field is proposed and studied in this thesis. The limitations imposed on the size and the operation speed of such a device by the requirement that it be controlled with an external uniform magnetic field have been discussed as well.

The research leading to these results has received funding, hereby gratefully acknowledged, from the European Community's Seventh Framework Programme (FP7/2007-2013) under Grant № 228673 (MAGNONICS).

Streszczenie

Ostatnio w dziedzinie elektromagnetyzmu wiele uwagi poświęca się teorii propagacji fal w tzw. *metamateriałach elektromagnetycznych* ze względu na możliwość modelowania ich niezwykłych właściwości przez odpowiedni dobór kształtu i struktury materiałów składnikowych. W skład metamateriału wchodzą materiały konwencjonalne; natomiast przedrostek „meta" odnosi się do wyższego poziomu organizacji strukturalnej. Badania nad metamateriałami zapoczątkował Veselago pionierską pracą [V. G. Veselago, Sov. Phys. Usp. **10**, 509 (1968)], w której wprowadził systematycznie opracowaną teoretyczną koncepcję materiału o ujemnych wartościach zarówno przenikalności magnetycznej, jak i elektrycznej. W przedziale częstotliwości, w którym obie te wielkości mają ujemne części rzeczywiste, ujemny jest też współczynnik załamania, aczkolwiek nie jest to konieczny warunek wystąpienia jego ujemnej wartości.

Z punktu widzenia zastosowań praktycznych duże nadzieje wiąże się z metamateriałami z przerwą energetyczną. Materiały te odznaczają się przestrzenną periodyczną modulacją właściwości fizycznych, a zainteresowanie nimi jest związane z możliwością regulacji ich struktury pasmowej. Przykładem metamateriałów z przerwą energetyczną są *kryształy fotoniczne*, w których sztucznie modulowany współczynnik załamania zmienia się okresowo z okresem porównywalnym z długością fali elektromagnetycznej. Charakterystyczną cechą struktur periodycznych jest obecność w ich widmie przerw stanowiących zakresy częstotliwości wzbronione dla propagacji fal. Badania wykazały, że modulacja periodyczna w materiałach magnetycznych prowadzi do powstania tzw. *kryształów magnonicznych*. Kryształy magnoniczne są magnetycznym odpowiednikiem kryształów fotonicznych, a rolę nośnika informacji odgrywają w nich fale spinowe. Choć lepiej poznane i szerzej stosowane są kryształy fotoniczne, kryształy magnoniczne stwarzają większe możliwości miniaturyzacji ze względu na długość fal spinowych, kilka rzędów wielkości mniejszą niż długość fal elektromagnetycznych o takiej samej częstotliwości.

Widmo energetyczne kryształu magnonicznego, podobnie jak widmo każdego układu o dyskretnej symetrii translacyjnej, ma strukturę pasmową. Występujące w nim przerwy noszą nazwę przerw magnonicznych; są to zakresy częstotliwości, w których nie mogą występować propagujące się fale spinowe. Przerwy takie zaobserwowano ostatnio w badaniach doświadczalnych z zastosowaniem spektroskopii Brillouina (*Brillouin light scattering*, BSL) [S. Tacchi *et al.*, Phys. Rev. B **82**, 024401 (2010); S. Tacchi *et al.*, Phys. Rev. B **82**, 184408 (2010)], mikroskopii skaningowej Kerra z rozdzielczością czasową (*time-resolved scanning Kerr microscopy*) [V. V. Kruglyak *et al.*, Phys. Rev. Lett. **104**, 027201 (2010)] i pomiarów transmisji [A. V. Chumak *et al.*, Appl. Phys. Lett. **94**, 172511 (2009)].

Koncepcja kryształu magnonicznego po raz pierwszy pojawiła się w pracy Vasseura i współpracowników [J. O. Vasseur *et al.*, Phys. Rev. B **54**, 1043 (1996)], przedstawiającej badanie periodycznego układu złożonego z cylindrycznych prętów ferromagnetycznych rozmieszczonych periodycznie w innym materiale magnetycznym. Teorię takich układów opracowywano również w późniejszych publikacjach, m.in. w [M. Krawczyk, H. Puszkarski, Acta Phys. Pol. A **93**, 805 (1998); H. Puszkarski, M. Krawczyk, Solid State Phenom. **94**, 125 (2003)]. W pracach tych badano położenie i szerokość przerw w widmie fal spinowych w zależności od okresu struktury i kontrastu, czyli stopnia modulacji, parametrów magnetycznych. Istotny wpływ na położenie i szerokość przerw okazał się mieć stopień modulacji długości wymiany, zdefiniowanej jako stosunek stałej wymiany do kwadratu magnetyzacji nasycenia.

Z punktu widzenia wytwarzania i zastosowań praktycznych najkorzystniejsze są urządzenia magnetyczne o strukturze planarnej, najlepiej wykonane z jednego materiału magnetycznego. Dynamika spinów w takich układach jest jednak jeszcze słabo zbadana z powodu trudności matematycznych związanych z ograniczonymi rozmiarami próbki. Jednym z wyzwań w obliczeniach widma fal spinowych jest uwzględnienie pola magnetostatycznego. Odpowiednim do tego narzędziem matematycznym okazuje się formalizm funkcji Greena. Metoda funkcji Greena została zastosowana na przykład w obliczeniach pola dipolowego w przedstawionej w pracy [N. Y. Grigorieva, B. A. Kalinikos, Tech. Phys. **54**, 1196 (2009)] teorii właściwości dyspersyjnych dipolowo-wymiennych fal spinowych w jednowymiarowych periodycznych układach planarnych zbudowanych z cienkich warstw ferromagnetycznych z paskami metalu periodycznie rozmieszczonymi na ich powierzchni. Za pomocą uśrednionej funkcji Greena wyznaczono również pola rozmagnesowujące i obliczono widmo fal spinowych planarnego układu oddziałujących ze sobą kwadratowych kropek magnetycznych o rozmiarach poniżej 1 mikrometra; wyniki pomiarów tego widma z zastosowaniem techniki rozpraszania Brillouina zostały przedstawione w pracy [S. Tacchi *et al.*, Phys. Rev. B **82**, 024401 (2010)].

Powszechnie stosowaną techniką analityczną badania struktury pasmowej dwu- i trójwymiarowych układów periodycznych jest metoda fal płaskich, z powodzeniem zaadaptowana i stosowana do badania kryształów półprzewodnikowych [T. Maehira *et al.*, Phys. Rev. Lett. **90**, 207007 (2003); M. Topsakal, S. Ciraci, Phys. Rev. B **85**, 045121 (2012)], fotonicznych [J. Joannopoulos, *Photonic Crystals: Molding the Flow of Light* (Princeton University Press, 2008)], fononicznych [T.-T. Wu, Z.-G. Huang, S. Lin, Phys. Rev. B **69**, 094301 (2004); S.-C. S. Lin, T. J. Huang, Phys. Rev. B **83**, 174303 (2011)] i magnonicznych [H. Puszkarski, M. Krawczyk, Solid State Phenom. **94**, 125 (2003); M. Krawczyk, H. Puszkarski, Phys. Rev. B **77**, 054437 (2008)]. Zgodnie z główną ideą metody fal płaskich w każdym przypadku równanie ruchu dla struktury

periodycznej przekształca się do przestrzeni odwrotnej za pomocą transformacji Fouriera i z zastosowaniem twierdzenia Blocha. W wyniku otrzymuje się zagadnienie własne, które rozwiązuje się za pomocą standardowych procedur numerycznych. Uzyskane w ten sposób częstotliwości własne w zależności od wektora falowego tworzą strukturę pasmową rozważanego kryształu.

W dotychczasowych badaniach z zastosowaniem metody fal płaskich w kryształach magnonicznych uwzględniano tylko składową dynamiczną pola rozmagnesowującego (patrz np. [H. Puszkarski, M. Krawczyk, Solid State Phenom. **94**, 125 (2003); M. Krawczyk, H. Puszkarski, Phys. Rev. B **77**, 054437 (2008); M. Krawczyk *et al.*, J. Appl. Phys. **108**, 093909 (2010)]). Jednym z głównych celów niniejszego doktoratu było przystosowanie metody fal płaskich do obliczeń magnonowej struktury pasmowej kryształów magnonicznych przez uwzględnienie niejednorodności wypadkowego pola magnetostatycznego powstającego w układzie w wyniku złożenia materiałów magnetycznych o różnej wartości magnetyzacji nasycenia. Cel ten osiągnięto w trzech etapach: 1) najpierw obliczono analitycznie pole magnetostatyczne dla ogólnego przypadku dwuwymiarowego kryształu magnonicznego o geometrii planarnej; 2) po szeregu przybliżeń wyniki obliczeń włączono do równania ruchu dla układów magnetycznych; 3) otrzymano ostateczne zagadnienie własne, które rozwiązano za pomocą odpowiednich procedur numerycznych. Otrzymano w ten sposób metodę umożliwiającą badanie widma fal spinowych kryształów magnonicznych o geometrii planarnej przy uwzględnieniu oddziaływań wymienno-dipolowych, w których energia wymiany jest porównywalna z energią oddziaływań magnetostatycznych, a także w warunkach dominacji jednego rodzaju oddziaływań.

Innym problemem pojawiającym się przy stosowaniu metody fal płaskich jest brak zbieżności rozwiązań zagadnienia własnego w przypadku kryształu magnonicznego złożonego z materiałów ferromagnetycznych i niemagnetycznych. Problem ten ma źródło w samym sformułowaniu równania ruchu dla ośrodków niejednorodnych. Równanie to opisuje dynamikę wektora magnetyzacji w materiale magnetycznym; w ośrodku niemagnetycznym magnetyzacja wynosi zero i staje się niezdefiniowana. W rezultacie w zbiorze wszystkich rozwiązań pojawiają się rozwiązania niefizyczne opisujące składowe dynamiczne wektora magnetyzacji w materiale niemagnetycznym. W niniejszym doktoracie zaproponowano i przetestowano prostą metodą pozwalającą rozwiązać ten problem, nieodłącznie związany z zastosowaniem metody fal płaskich do obliczeń widma fal spinowych planarnych kryształów magnonicznych. Główną ideą zaproponowanej metody jest zastąpienie elementów niemagnetycznych sztucznym materiałem o magnetyzacji nasycenia dziesięciokrotnie niższej niż w ośrodku magnetycznym. Pozwala to na odtworzenie wartości pola rozmagnesowania w układzie z marginesem błędu poniżej

10%. Omówiono też szczegółowo i przeanalizowano inne główne założenia związane z polem magnetostatycznym przyjęte w obliczeniach.

Udoskonaloną metodę fal płaskich przetestowano na licznych przykładach jedno- i dwuwymiarowych planarnych struktur periodycznych, porównując wyniki z różnymi danymi doświadczalnymi. Zweryfikowano na przykład magnetostatyczny charakter fal spinowych zaobserwowanych w jednowymiarowym krysztale magnonicznym złożonym z naprzemiennie ułożonych stykających się nanopasków permalojowych i kobaltowych tworzących strukturę periodyczną o okresie 500 nm. Stwierdzono, że w sieciach kwadratowych w postaci jednorodnej warstwy magnetycznej z nawierconymi otworami (antykropkami) o rozmiarach nanoskopowych sprzężenie magnetostatyczne modów brzegowych powoduje występowanie minipasm o zaskakująco wysokich wartościach prędkości propagacji. Wyniki te otwierają interesujące perspektywy w dziedzinie nanoskopowych urządzeń magnonicznych.

Istotną rolę w formowaniu się struktury pasmowej planarnego kryształu magnonicznego odgrywają warunki brzegowe na jego zewnętrznych powierzchniach. Warunki brzegowe można zmieniać między innymi przez stosowanie różnego rodzaju — metalowych, dielektrycznych itp. — podłoży lub warstw wierzchnich. W niniejszej rozprawie metoda fal płaskich została przystosowana do obliczeń widma fal spinowych w cienkich kryształach magnonicznych z metalowym ekranem wierzchnim o nieskończonej przewodnosci. W rozważanych strukturach zaobserwowano znaczny wzrost prędkości grupowej fal spinowych oraz przesunięcie pierwszej przerwy w stronę wyższych częstotliwości. Zaobserwowane efekty mogą być wykorzystane w urządzeniach magnonicznych, których działanie opiera się na przesunięciu fazowym fal spinowych, np. w urządzeniach w rodzaju interferometru Macha-Zehndera.

W materiałach, w których występuje uporządkowanie magnetyczne, zasadniczą rolę odgrywają oddziaływania wymienne. W szeregu podręczników przedstawiono wyprowadzenie wzoru na pole wymiany w jednorodnym materiale ferromagnetycznym wychodząc z modeli mikroskopowych. Rozwinięciem tych koncepcji jest przedstawione w niniejszym doktoracie wyprowadzenie wzoru na pole wymiany w kompozycie złożonym z dwóch lub większej liczby stykających się z sobą ferromagnetycznych materiałów składnikowych w przybliżeniu liniowym. Dla dużych stałych sieciowych magnonowa struktura pasmowa okazuje się niezależna od zastosowanej postaci pola wymiany. Przyczyną tego jest przewaga oddziaływań magnetostatycznych nad wymiennymi w tym zakresie częstotliwości. Sytuacja ulega zmianie w zakresie małych stałych sieciowych, w którym w zależności od przyjętej postaci pola wymiennego przerwa magnoniczna może wystąpić lub nie. Wyniki obliczeń numerycznych świadczą o ścisłym związku pola wymiennego z warunkami brzegowymi na międzywierzchniach na granicy dwóch

materiałów ferromagnetycznych. Wskazanie postaci pola wymiennego odpowiadającej fizycznym warunkom brzegowym, które muszą spełniać składowe dynamiczne wektora magnetyzacji w kryształach magnonicznych, wymaga jednakże dalszych pogłębionych badań.

Nieustanne poszukiwanie nowych paradygmatów logicznych mogących stanowić alternatywę dla modeli półprzewodnikowych skierowało uwagę badaczy na możliwość wykorzystania propagujących się fal spinowych jako podstawy działania urządzeń logicznych. W optyce znalazł zastosowanie interferometr Macha-Zehndera, stosowany jako podstawowy element bramek logicznych. W niniejszej pracy zaproponowano i zbadano prosty model interferometru falowo-spinowego tego samego typu wykorzystującego w działaniu lokalną niejednorodność efektywnego pola magnetycznego. Omówiono również ograniczenia dotyczące rozmiarów i prędkości pracy takiego urządzenia związane z zastosowaniem do sterowania nim jednorodnego zewnętrznego pola magnetycznego.

Badania, których wyniki przedstawiono w niniejszej pracy, otrzymały wsparcie finansowe z grantu № 228673 (MAGNONICS) w ramach Siódmego Programu Ramowego Wspólnoty Europejskiej (FP7/2007-2013).

Acknowledgements

First of all I would like to thank both of my research supervisors — prof. Doctor of Sciences Andriy M. Kuchko and dr hab. Maciej Krawczyk — for their help and support during all these years. Each of them has made an invaluable contribution to my formation as a scientist. They make their best efforts with passion for their subject. They dedicated plenty of their time, strength and energy to help me understand more deeply the nature of physical processes and phenomena occurring in magnetically ordered materials.

Special thanks to Maciej Krawczyk for giving me the opportunity to participate in the MAGNONICS project despite not having a PhD degree, for his generosity providing financial support and covering of all my travel expenses to attend conferences, for his kindness and care about the people around. I hope I have not disappointed him.

I want to express my gratitude to all the staff of our small but very friendly and close-knit Department of Nanomaterials Physics. I am infinitely grateful for this unforgettable time during which I was so fortunate to work with you. Special thanks to my cheerful and outgoing friend from Mexico, Javier Romero Vivas, for his patience and assistance in improving my level of English, for his extraordinary thinking and invaluable life experience which he so generously shares with others.

Many thanks to all my colleagues at the MAGNONICS project for the endless stream of experimental data and fruitful discussions of the results of our calculations.

Of course, an enormous thanks to my parents and sister for their support and valuable advice, which, unfortunately, I rarely follow. I also want to thank my friends who actively contributed to my employment abroad and are always glad to see me again. And of course, words of gratitude to my uncle, who helped me to realize my own potential, had great expectations from me, and always believed in my capabilities and talents.

Everyone who I have remembered and those who, inadvertently, I have forgotten to mention here, to all of you I bow and express gratitude for your support, thanks to which I was able to rise to a new step in my personal and professional evolution.

Contents

List of publications

1. A. N. Kuchko, M. L. Sokolovskii, V. V. Kruglyak, *Spin wave spectrum of a magnonic crystal with an internally structured defect*, Physica B **370**, 73 (2005).

2. A. N. Kuchko, M. L. Sokolovskii, and V. V. Kruglyak, *Spectrum of spin waves in a magnonic crystal with a structure defect*, The Physics of Metals and Metallography **101**, 513 (2006).

3. V. V. Kruglyak, M. L. Sokolovskii, V. S. Tkachenko, and A. N. Kuchko, *Spin-wave spectrum of a magnonic crystal with an isolated defect*, Journal of Applied Physics **99**, 08C906 (2006).

4. S. V. Vasiliev, V. V. Kruglyak, M. L. Sokolovskii, A. N. Kuchko, *Spin wave interferometer employing a local nonuniformity of the effective magnetic field*, Journal of Applied Physics **101**, 113919 (2007).

5. M. Krawczyk, J. Kłos, M. Sokolovskyy, and S. Mamica, *Materials optimization of the magnonic gap in three-dimensional magnonic crystals with spheres in hexagonal structure*, Journal of Applied Physics **108**, 093909 (2010).

6. J. W. Kłos, M. Krawczyk, and Mykhaylo Sokolovskyy, *Bulk and edge modes in two-dimensional magnonic crystal slab*, Journal of Applied Physics **109**, 07D311 (2011).

7. M. L. Sokolovskyy and M. Krawczyk, *The magnetostatic modes in planar one-dimensional magnonic crystals with nanoscale sizes*, Journal of Nanoparticle Research **13**, 6085 (2011).

8. S. Neusser, G. Duerr, S. Tacchi, M. Madami, M. L. Sokolovskyy, G. Gubbiotti, M. Krawczyk, and D. Grundler, *Magnonic minibands in antidot lattices with large spin-wave propagation velocities*, Physical Review B **84**, 094454 (2011).

9. M. L. Sokolovskyy, J. W. Kłos, S. Mamica, and M. Krawczyk, *Calculation of the spin-wave spectra in planar magnonic crystals with metallic overlayers*, Journal of Applied Physics **111**, 07C515 (2012).

10. S. Pal, B. Rana, S. Saha, R. Mandal, O. Hellwig, J. Romero-Vivas, S. Mamica, J. W. Kłos, M. Mruczkiewicz, M. L. Sokolovskyy, M. Krawczyk, and A. Barman,

Time-resolved measurement of spin-wave spectra in CoO capped $[Co(t)/Pt(7[\mathring{A}])]_{n-1}$ $Co(t)$ *multilayer systems*, Journal of Applied Physics **111**, 07C507 (2012).

11. V. V. Kruglyak, M. Dvornik, R. V. Mikhaylovskiy, O. Dmytriiev, G. Gubbiotti, S. Tacchi, M. Madami, G. Carlotti, F. Montoncello, L. Giovannini, R. Zivieri, J. W. Klos, M. L. Sokolovskyy, S. Mamica, M. Krawczyk, M. Okuda, J.-C. Eloi, S. Ward Jones, W. Schwarzacher, T. Schwarze, F. Brandl, D. Grundler, D. V. Berkov, E. Semenova, and N. Gorn, *Magnonic Metamaterials*, published as a chapter in the book *Metamaterial* edited by Xun-Ya Jiang, INTECH, (2012).

12. M. Krawczyk, M. L. Sokolovskyy, J. W. Kłos, S. Mamica, *On the formulation of the exchange field in the Landau-Lifshitz equation for spin-wave calculation in magnonic crystals*, accepted for publication in Advances in Condensed Matter Physics, (2012).

13. S. Tacchi, B. Botters, M. Madami, J. W. Kłos, M. L. Sokolovskyy, M. Krawczyk, G. Gubbiotti, G. Carlotti, A. O. Adeyeye, S. Neusser, and D. Grundler, *Mode conversion from quantized to propagating spin waves in a rhombic antidot lattice supporting spin wave nanochannels*, accepted for publication in Physical Review B, (2012).

14. Yu. S. Dadoenkova, N. N. Dadoenkova, I. L. Lyubchanskii, M. L. Sokolovskyy, J. W. Kłos, J. Romero-Vivas, M. Krawczyk, *Huge Goos-Hänchen effect for spin waves: a promising tool for study magnetic properties at interfaces*, accepted for publication in Applied Physics Letters, (2012).

Total number of the received citations is $44 + 12$, Hirsch index is $h = 3$.

Introduction

The phenomena of magnetic field and its influence on different materials are known for many years. In dependence on reaction of the material to the applied magnetic field one can classify three main types of magnetism: 1) *Diamagnetism*; 2) *Paramagnetism*; 3) *Ferromagnetism*. *Diamagnetics* are the ones that do not contain atoms or ions possessing permanent magnetic moments and do respond to an applied field with an induced magnetization that is opposed to the applied field. This sort of magnetism is intrinsic for all materials in nature. However, in materials containing permanent magnetic moments the diamagnetic contribution is usually overshadowed by the response of those moments. *Paramagnetics* are materials that contain permanent magnetic moments but not spontaneous long-range order. In the absence of an applied magnetic field the moments are randomly oriented so that no net magnetic moment is exhibited. Application of an external field then causes a partial alignment of the moments generating a net magnetic moment. A third type of magnetic materials are *ferromagnets*. In these materials, there are domains in which the magnetic fields of the individual atoms align, but the orientation of the magnetic fields of the domains is random. In equilibrium, these domains orient themselves so as to minimize the net magnetic moment of the macroscopic sample giving rise to no net magnetic field. When an external magnetic field is applied to them, the magnetic fields of the individual domains tend to line up in the direction of this external field.

The origin of the order within the domains can not be explained in the frame of classical electrodynamics, i.e., the magnetic interactions of elementary magnetic moments cannot be the cause of magnetic ordering. This fact simply follows from the comparison of two energies: the thermal energy that destroys the ferromagnetic order, and the energy of magnetic interaction of two magnetic dipoles. First one is of order $10^{-15} \div 10^{-13}$ J whilst the latter one is around 10^{-18} J. The electrostatic energy and Pauli exclusion principle is found to be sufficient to make spins of electrons be parallel within the domains. The part of the Coulomb energy that depends on the mutual orientation of the spins of electrons is called *exchange energy*.

The strong correlation between the directions of atomic spins in magnetically ordered crystals leads to the existence of a particular type of collective mode in such crystals. To understand the origin of these modes let us consider a ferromagnet at $T = 0$. All the

atomic magnetic moments then will be aligned in the same direction in order to minimize the energy of the ferromagnet. Let us now deflect the magnetic moment of a particular atom and let go. This change of direction will not remain localized in the original atom, but owing to the presence of the exchange interaction, it will be propagated through the crystal in the form of a mode of wave motion. Such waves are called *spin waves* (SWs). At the first time they were discovered by Bloch 80 years ago [1].

As in the case of any process of the wave nature SWs can exhibit either wave or "particle" properties in dependence on the scale of a system. When the latter is much larger than the atomic size of a magnetically ordered crystal a SW can be represented as an oscillation in the magnetic moment density, propagating through the entire structure [2, 3]. Considering a discrete model of a ferromagnet, Holstein and Primakoff [4] and Dyson [5] introduced quanta of SWs called *magnons*. They have predicted that magnons should behave as weakly interacting quasiparticles obeying the Bose-Einstein statistics.

Early indirect confirmation of the existence of SWs in nature came from measurements of thermodynamic properties of ferromagnets, proving the famous $T^{3/2}$ Bloch law. At the first time a direct observation of SWs was made using ferromagnetic resonance technique (FMR) in 1946 by Griffiths for the case of uniform precession [6]. In many aspects, a SW can be regarded as a magnetic analogue of a sound or light wave. During last several decades of theoretical and experimental research most of the properties inherent in waves of other origins, e.g., the excitation and propagation [7–11], reflection and refraction [12–16], interference and diffraction [17–19], tunneling [20, 21] of SWs and Doppler effect [22, 23], focusing and self-focusing [24–27] as well as formation of SW envelope solitons [28–30] have been demonstrated for the case of SWs.

Such a broad variety of observations has stimulated the field of *magnonics* - a young field of modern magnetism [31–33]. Its main aim is to investigate the behavior of SWs in nanostructured magnetic materials. These structures are known to possess such unique properties as giant magnetoresistance (GMR) [34, 35], large out-of-plane magnetic anisotropy [36, 37], resonant absorption of microwaves [38] and giant Faraday rotation in systems consisted of multilayered magnetic dielectric films, known as magneto-photonic crystals [39, 40].

Last decade we could see a huge improvement in the fabrication techniques of nanostructured materials. Nowadays the advancements in lithographic and other controlled fabrication techniques allow us to fabricate devices in nanoscale, e.g., modern processors have already reached 32 nm process technology. The situation with fabrication of ferromagnetic materials is slightly different from that with semiconductor devices. Unfortunately, nanostructured magnetic materials haven't found yet a wide application in the modern devices. Their place is still in the experimental labs and theoretical

models. However modern facilities of the labs allow us to fabricate ferromagnetic films with thickness of even a single monolayer and minimal modulation size in the plane of the film in the range of hundreds of nm [41–46]. The recent achievements offer the perspective of practical implementations of SWs in information transmission and processing devices [47–54]. Due to particular properties of SW spectra, magnonic devices should offer new functionalities that are currently unavailable in, e.g., photonic and electronic devices. For example, magnonic devices are easily controlled by the applied magnetic field or electric current [49, 54, 55]. Moreover, magnetic nanostructures are non-volatile and their implementation will enable programmable devices with ultrafast re-programming at the sub-nanosecond time scale [56]. In magnetic data storage media magnetic nanostructures have already been combined with nanoelectronics (e.g. in read heads and magnetic random access memories) and optics (e.g. in magneto-optical disks). Hence, magnonic devices offer the integration with microwave electronics and photonic devices at the same time. Since the wavelength of SWs is several orders of magnitude shorter than that of electromagnetic waves of the same frequency, magnonic devices are better candidates for miniaturization at these frequencies.

A large attention in nanomaterial physics has been addressed recently to the theory of wave propagation in systems with discrete translational symmetry because of the possibility of tuning their band structure. The spatial periodicity determines the conservation of momentum of a material body in the free space and of the quasimomentum in crystals. Most of electronic, magnetic, and optical properties of solids are directly determined by their band structure, which directly results from the quasimomentum conservation. For example, the spectrum of electrons in solids splits into bands - energy regions in which electron propagation is allowed. There exist also "band gaps" - energy regions in which there are no available electronic states, and so the electron propagation is prohibited. Structures with artificial translational symmetry have been created to design objects with properties that otherwise do not exist in nature. In particular, artificial electromagnetic dielectric materials with periodicity of the refractive index comparable to the wavelength of light, known as photonic crystals, have already found practical applications in optoelectronics [57]. Semiconductor superlattices [58], plasmonic [59] and phononic [60, 61] crystals are other typical examples of exploitation of the spatial periodicity for controlling propagation and scattering of electrons, light and phonons in various devices.

By analogy to the previously mentioned band gap materials, periodic magnetic composite structures used as a medium for controlled propagation of magnons are called *magnonic crystals* (MCs). The spectrum of a MC, similarly to the one of any other structure with discrete translational symmetry, is strongly influenced by the presence of

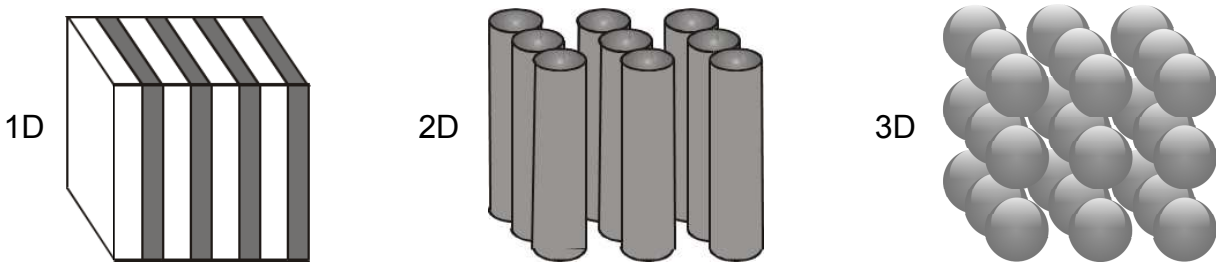

Figure 1. Schematics of the main types of MCs. 1D structure is represented by periodically repeated thin-film layers of two different types. 2D MC is shown for the case of a system of ferromagnetic cylindrical rods forming a 2D crystallographic lattice and embedded in a magnetic or nonmagnetic matrix. 3D magnonic structure is realized by arranging magnetic spheres in sites of a simple cubic lattice and immersing them into a matrix of different properties.

magnonic band gaps in which there are no allowed magnonic states. One of the first attempts to study the propagation of SWs in periodic magnetic structures was made by Elachi [62]. Nowadays, the number of studies on this topic has surged and continues to grow at a fast pace.

Depending on the dimensionality of the space in which the system is periodic, magnonic structures are one dimensional (1D), two dimensional (2D), or three dimensional (3D). Schematically these three cases are shown in Fig. 1. The simplest example of a 1D MC is a magnetic superlattice composed of alternating layers of different magnetic materials. This is probably the best studied system in which the spectrum of magnons has a band structure and contains band gaps [63–79]. One of the most popular methods of investigation of periodic 1D superlattices is the method known as "transfer-matrix". This method is based on the boundary conditions which connect the respective fields across the interface of two contacting layers. If the field is known at the one side of a layer, the field at the other side can be derived from a simple matrix operation. A stack of layers can then be represented as a system matrix, which is the product of the individual layer matrices. At the final step of the method the Bloch theorem is applied to the transfer matrix of an elementary cell of the periodic structure in order to obtain the dispersion relation of the studied system. This method has been successfully applied for ideal MCs [67, 68, 76, 80] as well as for ones with translational symmetry broken by a defect layer [81–83].

1D comb-like structures represented by a ferromagnetic wire with periodically situated dangling branches were studied in [84, 85]. The stop bands originate from the periodicity of the system determined by the distance between two neighbouring sites and from the eigenmodes of the dangling side branches. A theoretical investigation of the magnonic band structure of a 1D serial loop structure with dangling resonators using a Green's

function method is presented in [86]. It was shown that such structures exhibit very large magnonic stop bands. A more detailed study of the considered above mono-mode circuits can be found in a review published in [87]. Interesting spectra can be observed also in quasi-periodic and fractal magnetic structures [88, 89]. The mentioned above periodic and quasi-periodic systems have complicated geometry and therefore it can be a problem to calculate analytically their magnonic spectrum. Hence, numerical methods have to be used instead. So, MCs formed by periodically varying the width of a magnetic stripe were proposed and numerically studied in [52, 53].

A 2D MC represented by a system of ferromagnetic cylindrical rods embedded in a magnetic or nonmagnetic matrix is shown in Fig. 1. A concept of a MC together with the basic theory of 2D periodic magnetic structures were introduced in the pioneer work of Vasseur *et al.* in 1996 [90]. Since that time the theory of such systems has been developed in, e.g., Refs. [91, 92]. The position and width of band gaps in the SW spectrum were investigated in these articles as a function of the period of the structure and the depth of modulation ("contrast") of the magnetic parameters. It was found that the depth of modulation of the exchange constant has a drastic effect upon the position and width of the band gaps.

MCs with material parameters periodic in all three directions are the most challenging for fabrication and experimental investigation in nanoscale. A schematic of a 3D MC comprised of magnetic spheres arranged in sites of a simple cubic lattice and immersed into a matrix of different properties is shown in the right panel of Fig. 1. One of the promising techniques for fabrication of 3D periodic magnetic structures is one based on protein crystallization [93, 94]. Using this technique it is possible to grow ordered 3D arrays of magnetic nanoparticles of sufficient quality and precision within a short period of time (hours to days). Size of each nanoparticle can be as small as 8-12 nm while the whole structure is on the meso-scale, with sizes of the order of tens, up to a few hundred micrometres. Despite all the achievements of the protein crystallization technique, replacing protein nonmagnetic shells by magnetic ones is still a challenge. The theoretical treatment of such magnetic systems is more developed than their fabrication and experimental investigation. The dispersion of SW modes in ordered superlattices of nanospheres were studied in [95, 96]. Magnonic band structure of 3D periodic all-ferromagnetic composites was calculated by M. Krawczyk and H. Puszkarski in [97, 98].

The excitation and detection of SWs is the major technological challenge for the realization of magnonic devices. The cavity based FMR was historically the first experimental technique used to detect precession of magnetization [6] by measuring spectra of the absorption of microwaves in a cavity containing a magnetic sample. The spectra are determined by the density of states of SWs that can resonantly couple to the

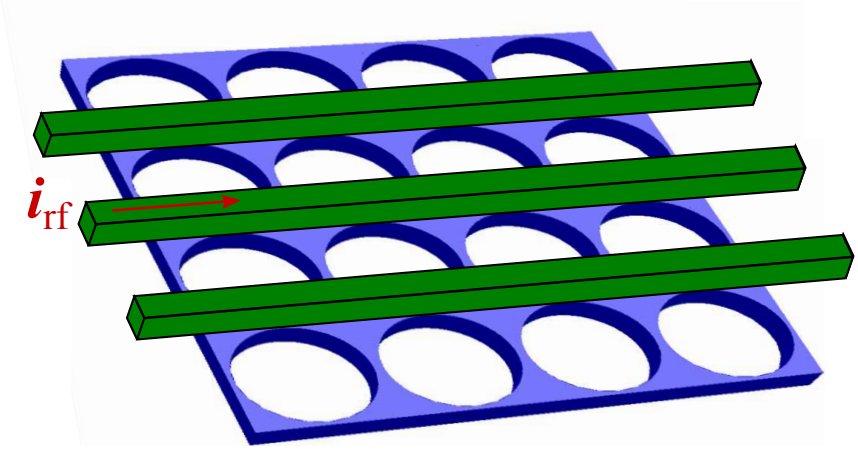

Figure 2. Sketch of a coplanar waveguide (CPW) integrated to an antidot lattice (ADL) prepared from a thin ferromagnetic film. The CPW consists of three metallic leads (ground-signal-ground leads). Adjusting the dimensions of the CPW allows one to vary the profile of the magnetic field generated by microwave current i_{rf} supplied by the VNA. This defines the wave vector transferred to the sample. The same CPW picks up the voltage induced by precessing spins.

microwave field. This technique is conventionally used to study magnetization dynamics at frequencies up to about 100 GHz. At higher frequencies, the mismatch between the linear momentum of a free space electromagnetic radiation (photon) and that of a magnon increasingly prohibits an efficient coupling. Therefore, higher frequencies require the use of different experimental and technical concepts to excite and measure, e.g., THz magnons.

The vector network analyser ferromagnetic resonance (VNA-FMR) technique with a broadband vector network analyser (VNA) operated in the GHz frequency regime represents a relatively new twist in the FMR spectroscopy. Microwaves applied to a waveguide locally excite SWs that in turn induce a high-frequency voltage due to precessing magnetization (see Fig. 2). The VNA-FMR technique measures spectra of both the amplitude and phase change of microwaves passing through a magnetic sample integrated with the waveguide [99–101]. The geometrical parameters of the waveguide determine the spatial distribution of the rf magnetic field and therefore the wavelength spectrum addressed by the microwave field. Hence, the VNA-FMR can be also referred to as a "near field" FMR. Due to the large penetration depth of microwaves, both thin film and bulk samples can be successfully investigated using this technique.

The recent advances in the studies of MCs are associated with advances in the Brillouin light scattering (BLS) technique, which has proved to be a very powerful tool for the investigation of magnetization dynamics in magnonic structures [102]. This technique is based on the phenomenon of Brillouin–Mandelstam inelastic scattering of photons from

either thermal, or externally pumped magnons [103]. The frequency and the wave vector of the scattered photons are shifted by amounts equal to the frequency and the wave vector of the scattering magnons, respectively. This facilitates the possibility of a direct mapping of the magnonic dispersion in the reciprocal space [42, 104]. In particular, the BLS technique is suitable for measuring the magnonic band structure, provided that the periodicity of the magnonic crystal is such that the Brillouin zone (BZ) boundary lies in the accessible wave vector range (up to $2.2 \cdot 10^5$ rad/cm). The spin wave dispersion can be measured in different scattering geometries that differ by the relative orientation of the magnon wave vector and direction of the applied magnetic field. Using this technique planar 1D MCs formed by arrays of closely spaced Permalloy stripes of identical [104] or alternating width [105] were studied, showing the existence of tuneable band gaps. Furthermore, alternating stripes of two different magnetic materials were studied in [42]. BLS measurements are quite demanding on the surface quality of the studied samples. The sensitivity of this technique is limited to the surface region thinner than the optical skin depth and requires a high surface quality of the studied samples. Nonetheless, BLS measurements have been performed on such "rough" samples as granular [106] and rod [107] nanocomposites. Cochran pointed out that only "acoustic" SW modes of a superlattice, in which magnetic moments of different layers precess in phase and which corresponds to the first band of the spectrum, can be observed in a BLS experiment [108]. The higher frequency modes have an "optical" character with magnetic moments precessing out of phase, which reduces the BLS signal from such modes dramatically.

Another way of probing magnetization in nanostructured magnonic materials is offered by measuring a change in polarization of light reflected from a magnetic sample, due to the magneto-optical Kerr effect [109]. In a time-resolved scanning Kerr microscopy (TRSKM) experiment, the sample is pumped by a repetitive and coherent pulse, i.e. it has a well-defined phase with respect to the probe beam. To probe, one uses ultrashort optical pulses and controls their arrival time relative to the pump. By changing the optical path of the probe beam one can trace the time evolution of the excited dynamics. The TRSKM provides images of dynamic magnetization with a spatial resolution of down to 250 nm in real space [110–113], and is suitable for studying both continuous and nanostructured samples. The minimal temporal resolution of the TRSKM is on the subpicosecond time scale, therefore offering the detection of SWs in the THz frequency regime. The TRSKM performs a 3D vectorial analysis of the time dependent magnetization [114] and is therefore phase sensitive. Alternatively, one can combine the magneto-optical detection with a VNA-FMR setup to image SW modes in the frequency rather than time domain [115].

From the point of view of fabrication and practical applications, magnonic devices with a planar geometry and, ideally, fabricated from a single magnetic material are easier

to realize. MCs fabricated by periodic corrugation of yttrium iron garnet (YIG) and ferromagnetic metallic films were studied in [116, 117], respectively. A 1D system formed by alternating stripes of two different magnetic materials was investigated in [42, 118], although magnonic band gaps were observed only in the latter work. In [119] it was shown that a ferrite film with periodically etched holes can serve as a filter for MSSWs propagating in the film plane.

A popular analytical method for investigation the band structure of 2D and 3D periodic systems is the plane wave method (PWM). This method has been successfully developed and applied for electronic [120, 121], photonic [57], phononic [61, 122, 123] as well as magnonic crystals [90, 97, 98, 124]. Following the main idea of the PWM, the equation of motion for a periodic structure is transformed into the reciprocal space with the use of the Fourier transform and the Bloch theorem. The obtained eigenvalue problem is solved then by standard numerical routines. Its solution yields eigenfrequencies that form the band structure of the considered crystal.

The PWM has proved to be a flexible tool for SW spectrum calculations in MCs, relatively fast, giving an opportunity for modeling new properties and providing the insight in new physics of SWs in periodic magnetic structures. But so far the PWM were used for systems unsuitable for comparison with experimental measurements and to calculate SW spectra in elements of realistic devices. The main drawback of this method was the assumption of the infinite thickness of MCs. In magnonics, as opposed to photonics, this is a strong assumption that changes drastically the SW spectra making impossible to use the PWM for interpretation of the measurements. The main goal of the research providing to this thesis is to overcome this limitation. This will be done in the following steps, which combine development of the theoretical model, its verification with experimental data and providing their interpretation. The attempt for development of a practical application of MCs will also done.

One of the challenges in the SW spectrum calculations is to consider the magnetostatic field. So far, only its dynamic component was taken into account in the PWM (see, e.g., [92, 98, 124]). One of the main objectives of this thesis is **to extend the PWM to the calculation of the magnonic band structure in thin MCs, by taking into account the nonuniformity of the total magnetostatic field in the system**.

The improved method is tested in numerous examples of 1D and 2D planar periodic structures and compared with various experimental data. In order **to calculate the SW spectrum of MCs with nonmagnetic inclusions a simple technique is applied to the PWM and justified in this work**. All major assumptions related to the magnetostatic field and used in the calculations are analyzed and discussed in detail in this thesis.

As it was mentioned above the origin of magnetic ordering is the exchange energy. The derivation of the exchange field in a uniform ferromagnetic material from microscopic models can be found in different textbooks, e.g., [2, 3, 125, 126]. Following the ideas presented in these books **the exchange field to be derived in the linear approximation for the case of composite materials, the structure of which includes two or more ferromagnetic constituent materials in direct contact**.

Boundary conditions play an important role in the formation of the band structure of MCs. One of the possibilities for manipulating them is to use different types of substrates or overlayers, e.g., metallic, dielectric etc. So, another objective of this thesis is **to develop the PWM for the calculation of the SW spectrum of thin MCs with a metallic screen on top of them**.

The continuing search for new logic paradigms alternative to those based upon semiconductors has led to suggestions that propagating SWs could create basis for such logic devices. The Mach-Zehnder interferometer has been used as the basic element of logic gates in optics. **A simple example of this interferometer employing a local nonuniformity of the effective magnetic field is proposed and studied** in this work.

This thesis is organized as follows. Different forms of the exchange field in an inhomogeneous ferromagnetic material are derived from the Heisenberg Hamiltonian in the linear approximation in section 1. The results of this section were accepted for publication in Advances in Condensed Matter Physics. Section 2 presents the general theory of SW propagation in MCs with planar geometry composed of two different materials. In subsection 2.1 the magnetostatic field is calculated for the case of thin periodic magnetic structures. The ideas and results of this subsection were used in [45, 127, 128]. Propagation of SWs in planar MCs is studied in section 3. Influence of different forms of the exchange field on the band structure of MCs is shown in subsection 3.1. The results of this subsection were accepted for publication in Advances in Condensed Matter Physics [129]. Subsection 3.2 is devoted to a comprehensive study of magnetostatic SWs in planar 1D MCs. The results of this subsection were published in [127]. The SW spectrum of a 1D MC comprised of a periodic array of two ferromagnetic thin slabs separated by a nonmagnetic dielectric material is calculated and analyzed in subsection 3.3. The results of this subsection were presented in an oral session of the Progress In Electromagnetics Research Symposium, that was held on March 20-23, 2011 in Marrakesh, Morocco. Influence of metallic overlayers on the band structure of planar MCs is studied in subsection 3.4. The main results of this subsection were published in [130]. Propagation of SWs in a 2D ADL structure is investigated in details in subsection 3.5. The results of the research in this subsection were published in [45]. Tunnelling of SWs in a rhombic

ADL in deep-submicron channels between the holes is demonstrated in subsection 3.6. The results of this subsection have been submitted for publication to Physical Review B [46]. Limitations of the developed PWM are discussed in subsection 3.7. A possible realization of the Mach-Zehnder interferometer employing a local nonuniformity of the effective magnetic field and with SWs acting as information carriers is proposed and studied in section 4. The results of this research were published in [55].

1. Forms of the exchange field in inhomogeneous media

The expression for the exchange field in inhomogeneous magnetic materials will be derived in two steps. First, the formula for the exchange energy density is obtained from the microscopic Heisenberg Hamiltonian in subsection 1.1. Crucial in this procedure is a transition from the discrete model to a continuous one. In the second step, the formula for the exchange field is derived from the exchange energy density in subsection 1.2. The linear approximation is used in this step, and a space dependence of magnetic material parameters is allowed for.

1.1. Exchange energy functional

As mentioned above, the exchange interactions play a fundamental role in magnetic materials. Thus, they are a crucial factor to be taken into account in the calculation of the spin dynamics. Many textbooks, e.g., Refs. [2, 3, 125, 126], present the derivation of the formula for the exchange field in a uniform ferromagnetic material in microscopic models. The ideas presented in these books will be followed here in the consideration of composite materials, the structure of which includes two or more ferromagnetic constituent materials in direct contact. The exchange effects were discovered independently by W. Heisenberg and P. A. M. Dirac in 1926. Both proposed the following form of the energy operator (Hamiltonian) for the exchange interaction between two particles with spins $\mathbf{S}_1$ and $\mathbf{S}_2$:

$$\mathcal{H}_{\text{ex}} = -2J_{12}\mathbf{S}_1 \cdot \mathbf{S}_2, \tag{1}$$

where J_{12} is the exchange integral. In the case of a discrete lattice of spins the Heisenberg Hamiltonian $\mathcal{H}_l$ that defines the exchange energy of spin $\mathbf{S}_l$ at lattice site l can be written:

$$\mathcal{H}_l = -2 \sum_{m \in \text{n.n.}} J_{lm}\mathbf{S}_l \cdot \mathbf{S}_m, \tag{2}$$

where $\mathbf{S}_m$ is the total spin vector at lattice site m, and the summation is performed over all the nearest neighbors (n.n.) of the l-th spin; J_{lm} is the exchange integral between the spins at lattice sites l and m. The Hamiltonian in (2) describes the isotropic Heisenberg

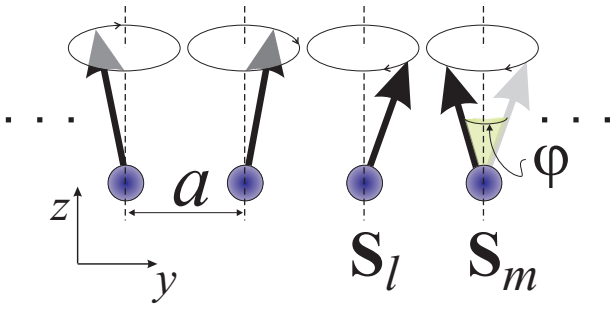

Figure 3. A discrete lattice of spins. The angle between nearest-neighbor spins $\mathbf{S}_l$ and $\mathbf{S}_m$ is φ, and the distance between them is a.

model of the considered structure. Systems with anisotropic Heisenberg interactions were studied, e.g., in [131, 132].

Let us introduce a normalized unit vector for spin $\mathbf{S}_l$:

$$\boldsymbol{\alpha}_l = \frac{\mathbf{S}_l}{|S_l|}. \tag{3}$$

The equation (2) becomes:

$$\mathcal{H}_l = -2|S_l| \sum_{m \in \text{n.n.}} J_{lm}|S_m|\boldsymbol{\alpha}_l \cdot \boldsymbol{\alpha}_m. \tag{4}$$

By the definition (3), $\boldsymbol{\alpha}_l \cdot \boldsymbol{\alpha}_m = \cos\varphi$, where φ is the angle between nearest-neighbor spin vectors at lattice sites l and m (see Fig. 3).

Let us assume that the angle φ is small and the spin vectors are continuous and smooth functions of the position vector $\mathbf{r}$, i.e. $\boldsymbol{\alpha} = \boldsymbol{\alpha}(\mathbf{r})$ [126]. This can be realized formally by averaging $\mathbf{S}$ over the unit cell, i.e. by the introduction of the magnetization vector $\mathbf{M}(\mathbf{r})$: $\mathbf{M}(\mathbf{r}_l) = \bar{N}\mu_B g\mathbf{S}_l$, where $\bar{N} = N/V$ is the number of spins (N) per unit cell volume (V); μ_B is the Bohr magneton and g is the g-factor (for free electrons $g \approx 2$). By these definitions:

$$\boldsymbol{\alpha}_l = \frac{\mathbf{S}_l}{|S_l|} \equiv \frac{\mathbf{M}(\mathbf{r}_l)}{M(\mathbf{r}_l)}$$

and $\boldsymbol{\alpha}(\mathbf{r})$ can be written as a continuous function of the position vector:

$$\boldsymbol{\alpha}(\mathbf{r}) = \frac{\mathbf{M}(\mathbf{r})}{M(\mathbf{r})}. \tag{5}$$

As a continuous function of the position vector the unit vector $\boldsymbol{\alpha}$ at lattice site m ($\boldsymbol{\alpha}(\mathbf{r}_m) \equiv \boldsymbol{\alpha}_m \equiv \boldsymbol{\alpha}'$) can be represented as a Taylor series:

$$\boldsymbol{\alpha}' = \boldsymbol{\alpha}_l + \sum_i (\partial_{x_i}\boldsymbol{\alpha}_l)dx_i + \frac{1}{2}\sum_{i,j}(\partial_{x_i}\partial_{x_j}\boldsymbol{\alpha}_l)dx_i dx_j + ..., \tag{6}$$

where $i = x, y$ or z; dx_i is the distance between adjacent spins along the i axis; ∂_{x_i} denotes the partial derivative with respect to the Cartesian component x_i. The limitation of the expansion to the linear and quadratic terms only (which is equivalent to assuming small variations of $\boldsymbol{\alpha}(\mathbf{r})$) and the substitution of (6) into (4) leads to:

$$\mathcal{H}_l = -2|S_l| \sum_{m\in(\text{n.n.})} J_{lm}|S_m| - 2|S_l| \sum_{m\in(\text{n.n.})} J_{lm}|S_m| \sum_i \boldsymbol{\alpha}_l \cdot (\partial_{x_i}\boldsymbol{\alpha}_l) dx_i \\ -|S_l| \sum_{m\in(\text{n.n.})} J_{lm}|S_m| \sum_{i,j} \boldsymbol{\alpha}_l \cdot (\partial_{x_i}\partial_{x_j}\boldsymbol{\alpha}_l) dx_i dx_j. \tag{7}$$

The unit vectors $\boldsymbol{\alpha}_l$ fulfill the obvious relation: $\boldsymbol{\alpha}_l \cdot \boldsymbol{\alpha}_l = 1$. Differentiated with respect to x_i, this equation reads:

$$(\partial_{x_i}\boldsymbol{\alpha}_l) \cdot \boldsymbol{\alpha}_l = 0. \tag{8}$$

Hence, the second term on the right side of (7) is equal to zero. The Hamiltonian becomes:

$$\mathcal{H}_l = -2|S_l| \sum_{m\in(\text{n.n.})} J_{lm}|S_m| - |S_l| \sum_{m\in(\text{n.n.})} J_{lm}|S_m| \sum_{i,j} \boldsymbol{\alpha}_l \cdot (\partial_{x_i}\partial_{x_j}\boldsymbol{\alpha}_l) dx_i dx_j. \tag{9}$$

In a homogeneous material the spin magnitude is equal at each lattice site, $|S_l| = |S_m|$, and the exchange integral is constant, i.e. $J_{lm} = J$ for each n.n. l and m ($l \neq m$). [1] With this homogenization (9) becomes:

$$\mathcal{H}_l = -2Z|S|^2 J - |S|^2 J \sum_{m\in\text{n.n.}} \sum_{i,j} \boldsymbol{\alpha}_l \cdot (\partial_{x_i}\partial_{x_j}\boldsymbol{\alpha}_l) dx_i dx_j, \tag{10}$$

where Z is the number of nearest neighbors. In cubic crystal structures (simple cubic (sc), body centered cubic (bcc) and face centered cubic (fcc) lattice types) the distance between neighboring atoms is equal along each axis: $|dx_i| = a$. Thus, the sum over nearest neighbors $\sum_{m\in\text{n.n.}}(\cdots)dx_i dx_j$ for $i \neq j$ is 0 for each lattice type. Thus, the Hamiltonian (10) can be written as:

$$\mathcal{H}_l = -2Z|S|^2 J - 2|S|^2 J a^2 \sum_i (\partial_{x_i}\partial_{x_i}\boldsymbol{\alpha}_l). \tag{11}$$

[1] This assumption applies to inhomogeneous materials when two atomic planes (for n.n. exchange interactions) at the interfaces are excluded from consideration.

Equation (8) can be again differentiated with respect to x_j, to yield:

$$\boldsymbol{\alpha}_l \cdot (\partial_{x_i}\partial_{x_j}\boldsymbol{\alpha}_l) = -(\partial_{x_i}\boldsymbol{\alpha}_l)\cdot(\partial_{x_j}\boldsymbol{\alpha}_l). \tag{12}$$

This equality allows to rewrite the equation (11) for the exchange energy in the form:

$$\mathcal{H}_l = -2Z|S|^2J + 2|S|^2Ja^2\sum_i(\partial_{x_i}\boldsymbol{\alpha}_l)^2. \tag{13}$$

To express the energy density $\mathcal{E}_{\text{ex}}$ as a continuous function of the position vector the summation must be performed over all the spins in the unit cell and the result divided by the unit cell volume. The energy density obtained in this way is:

$$\mathcal{E}_{\text{ex}} = \lambda M^2 + A\sum_i(\partial_{x_i}\boldsymbol{\alpha}(\mathbf{r}))^2, \tag{14}$$

where $A = 2nJS^2/a$, and $n = 1, 2$ or 4 for sc, bcc and fcc lattices, respectively [126]; $\boldsymbol{\alpha}(\mathbf{r})$ is as defined in (5), and

$$\lambda = -\frac{2ZJ}{\bar{N}\mu_B^2 g^2}.$$

To calculate the total exchange energy E_{ex} in a magnetic material the energy density (14) must be integrated over the volume of the material:

$$\begin{aligned} E_{\text{ex}} &= \int_V \mathcal{E}_{\text{ex}}d^3r = \int_V \lambda M^2 d^3r + \int_V A\sum_i(\partial_{x_i}\boldsymbol{\alpha}(\mathbf{r}))^2 d^3r \\ &= \int_V \lambda M^2 d^3r + \int_V A\left[\left(\partial_x\frac{\mathbf{M}}{M}\right)^2 + \left(\partial_y\frac{\mathbf{M}}{M}\right)^2 + \left(\partial_z\frac{\mathbf{M}}{M}\right)^2\right]d^3r. \end{aligned} \tag{15}$$

A spin wave can be regarded as a coherent precession of the magnetization vector around its equilibrium direction. Based on this observation most SW calculations are performed in the linear approximation, which we have already used in equation (7). Let us use it again to simplify the expression (15) for the total exchange energy.

1) Exchange energy : Form I

In the linear approximation the magnetization vector:

$$\mathbf{M}(\mathbf{r}) = M_x(\mathbf{r})\hat{x} + M_y(\mathbf{r})\hat{y} + M_z(\mathbf{r})\hat{z}$$

can be split into the static and dynamic components. Here the magnetization component along the $\hat{z}$-axis, the direction of the applied magnetic field (see Fig. 3), is assumed to be constant in time, and its magnitude is close to that of the total magnetization vector:

$$M_z \approx |\mathbf{M}| \equiv M_{\mathrm{S}}. \tag{16}$$

Let m_x and m_y denote the time-dependent components M_x and M_y, respectively, of the magnetization vector. The dynamic magnetization vector, defined as $\mathbf{m} = (m_x, m_y)$, is a two-dimensional vector in the plane perpendicular to the direction of the saturation magnetization.

In the approximation (16) the exchange energy (15) becomes:

$$E_{\mathrm{ex}} = \int_V \lambda M_{\mathrm{S}}^2 d^3r + \int_V A \left(\nabla \frac{\mathbf{m}}{M_{\mathrm{S}}} \right)^2 d^3r. \tag{17}$$

This is the final formula for the exchange energy, which we shall refer to as **Form I**.

2) Exchange energy: Form II

Let us continue simplifying expression (17) of the first form of the exchange energy. Using basic rules of differentiation one can rewrite the integrand of the second integral in (17) as follows:

$$\left(\partial_x \frac{\mathbf{m}}{M_{\mathrm{S}}} \right)^2 = \left(\frac{(\partial_x \mathbf{m}) M_{\mathrm{S}} - (\partial_x M_{\mathrm{S}}) \mathbf{m}}{M_{\mathrm{S}}^2} \right)^2 = \frac{(\partial_x \mathbf{m})^2 M_{\mathrm{S}}^2 + (\partial_x M_{\mathrm{S}})^2 \mathbf{m}^2 - 2 M_{\mathrm{S}} (\partial_x M_{\mathrm{S}}) (\partial_x \mathbf{m}) \cdot \mathbf{m}}{M_{\mathrm{S}}^4}, \tag{18}$$

where an obvious relation has been used in the last component of the numerator:

$$2\mathbf{m} \cdot \partial_x \mathbf{m} = \partial \left(\mathbf{m}^2 \right).$$

The same calculations can be applied to other components of the nabla operator in the exchange energy functional (17). The following expression for the exchange energy can be obtained:

$$E_{\text{ex}} = \int_V \lambda M_{\text{S}}^2 d^3r + \int_V \frac{A}{M_{\text{S}}^2} \left(\nabla \mathbf{m}\right)^2 d^3r + \int_V \frac{A}{M_{\text{S}}^4} \left(\nabla M_{\text{S}}\right)^2 \mathbf{m}^2 d^3r - \int_V \frac{A}{M_{\text{S}}^3} \left(\nabla M_{\text{S}}\right) \cdot \left(\nabla \mathbf{m}^2\right) d^3r. \tag{19}$$

In a MC the saturation magnetization is a function of the position vector with a step increase at interfaces. For a bi-component MC (i.e., consisting of two ferromagnetic materials, A and B) $M_{\text{S}}(\mathbf{r})$ can be defined with the help of the characteristic function $S(\mathbf{r})$:

$$M_{\text{S}}(\mathbf{r}) = \left(M_{\text{S,A}} - M_{\text{S,B}}\right) S(\mathbf{r}) + M_{\text{S,B}}, \tag{20}$$

where

$$S(\mathbf{r}) = \begin{cases} 1, & \text{for } \mathbf{r} \text{ pointing at material A} \\ 0, & \text{for } \mathbf{r} \text{ pointing at material B} \end{cases}$$

and $M_{\text{S,A}}$, $M_{\text{S,B}}$ are the saturation magnetizations in materials A and B, respectively. As one can see in the last two terms in (19) there are derivatives of $M_{\text{S}}(\mathbf{r})$ with respect to the position. According to (20) these derivatives are the ones from the step function, i.e., $\nabla M_{\text{S}}(\mathbf{r}) = \left(M_{\text{S,A}} - M_{\text{S,B}}\right) \delta(\mathbf{r} - \mathbf{r}_{\text{interface}})$, where δ is the Dirac delta function and $\mathbf{r}_{\text{interface}}$ is a position vector which defines the interface. It means that these two terms are connected with the exchange energy localized exactly at the interfaces and which are related to the jump of the saturation magnetization value (the values of saturation magnetization of the constituent materials are assumed to be parallel in whole MC). It can be shown that they introduce singularities in the equation of motion and, therefore, these terms will be neglected[2].

Thus, two different formulas for the exchange energy of nonuniform materials have been obtained in the linear approximation:

$$\begin{aligned} &\textbf{Form I:} \qquad E_{\text{ex}} = \int_V \lambda M_{\text{S}}^2 d^3r + \int_V A \left(\nabla \frac{\mathbf{m}}{M_{\text{S}}}\right)^2 d^3r, \\ &\textbf{Form II:} \qquad E_{\text{ex}} = \int_V \lambda M_{\text{S}}^2 d^3r + \int_V \frac{A}{M_{\text{S}}^2} (\nabla \mathbf{m})^2 d^3r. \end{aligned} \tag{21}$$

In the case of a uniform ferromagnetic body these two forms are equivalent.

[2] In fact these terms introduce non-Hermitian elements into the equation of motion and its physical interpretation is questionable.

1.2. Exchange field

The exchange field can be derived from the exchange energy functionals (21) as the first variational derivative with respect to the magnetization vector [3, 133]:

$$\mathbf{H}_{\mathrm{ex}}(\mathbf{r}) = -\frac{1}{\mu_0}\frac{\delta E_{\mathrm{ex}}}{\delta \mathbf{M}} = -\frac{1}{\mu_0}\left[\frac{\delta E_{\mathrm{ex}}}{\delta m_x}, \frac{\delta E_{\mathrm{ex}}}{\delta m_y}, \frac{\delta E_{\mathrm{ex}}}{\delta M_{\mathrm{S}}}\right]. \tag{22}$$

This equation is written in SI units. The variational derivatives can be calculated using Euler's formula [3]:

$$\frac{\delta E_{\mathrm{ex}}}{\delta m_x} = \frac{\partial \eta}{\partial m_x} - \nabla\left(\frac{\partial \eta}{\partial(\nabla m_x)}\right) = \frac{\partial \eta}{\partial m_x} - \sum_i \frac{\partial}{\partial x_i}\left(\frac{\partial \eta}{\partial(\partial_{x_i} m_x)}\right), \tag{23}$$

where $E_{\mathrm{ex}} = \int_V \eta d^3r$, and

$$\eta^{(\mathrm{I})} = \lambda M_{\mathrm{S}}^2 + A\left(\nabla \frac{\mathbf{m}}{M_{\mathrm{S}}}\right)^2, \tag{24a}$$

$$\eta^{(\mathrm{II})} = \lambda M_{\mathrm{S}}^2 + \frac{A}{M_{\mathrm{S}}^2}(\nabla \mathbf{m})^2 \tag{24b}$$

for the **Form I** and **Form II** of the exchange energy, respectively (see the equation (21)). These calculations can be performed independently for each form of the exchange energy defined in (21). We shall henceforth take into account the inhomogeneity of the material by assuming space-dependent exchange constant $A(\mathbf{r})$ and saturation magnetization $M_{\mathrm{S}}(\mathbf{r})$.

1) Exchange field: Form I

For the **Form I** of the exchange energy functional (24a) the functional derivative can be calculated directly from (23). Since

$$\frac{\partial \eta^{(\mathrm{I})}}{\partial m_x} = \frac{\partial \eta^{(\mathrm{I})}}{\partial m_y} = 0$$

and the first term in $\eta^{(\mathrm{I})}$ is independent of $\partial_{x_i} m_x$, (22) can be rewritten as:

$$\mu_0 \mathbf{H}_{\rm ex}(\mathbf{r}) = \nabla \frac{\partial \eta}{\partial \nabla \mathbf{m}} = \nabla \frac{\partial A \left(\nabla \dfrac{\mathbf{m}}{M_{\rm S}} \right)^2}{\partial \nabla \mathbf{m}}$$
$$= \nabla \left[2A \left(\nabla \frac{\mathbf{m}}{M_{\rm S}} \right) \cdot \left(\frac{\partial \nabla \dfrac{\mathbf{m}}{M_{\rm S}}}{\partial \nabla \mathbf{m}} \right) \right] = \nabla \cdot \left[\frac{2A(\mathbf{r})}{M_{\rm S}(\mathbf{r})} \right] \nabla \frac{\mathbf{m}(\mathbf{r})}{M_{\rm S}(\mathbf{r})}. \tag{25}$$

2) Exchange field: Form II

As in the previous case, $\partial \eta^{(\rm II)} / \partial m_x = 0$ and the first term in (24b) is independent of $\partial_{x_i} m_x$. Thus, the functional derivative of $E_{\rm ex}$ with respect to m_x can be written as:

$$\frac{\delta E_{\rm ex}}{\delta m_x} = -\sum_i \frac{\partial}{\partial x_i} \left(\frac{\partial \dfrac{A}{M_{\rm S}^2} (\nabla \mathbf{m})^2}{\partial (\partial_{x_i} m_x)} \right)$$
$$= -\sum_i \frac{\partial}{\partial x_i} \left[\frac{A}{M_{\rm S}^2} \frac{\partial \left[(\partial_x m_x)^2 + (\partial_x m_y)^2 + (\partial_y m_x)^2 + (\partial_y m_y)^2 + (\partial_z m_x)^2 + (\partial_z m_y)^2 \right]}{\partial (\partial_{x_i} m_x)} \right]$$
$$= -\frac{\partial}{\partial x} \left[\frac{2A}{M_{\rm S}^2} (\partial_x m_x) \right] - \frac{\partial}{\partial y} \left[\frac{2A}{M_{\rm S}^2} (\partial_y m_x) \right] - \frac{\partial}{\partial z} \left[\frac{2A}{M_{\rm S}^2} (\partial_z m_x) \right]. \tag{26}$$

The y component of the magnetization has the same form. Thus, the total exchange field can be written in this compact form:

$$\mu_0 \mathbf{H}_{\rm ex}(\mathbf{r}) = \nabla \cdot \left[\frac{2A(\mathbf{r})}{M_{\rm S}^2(\mathbf{r})} \right] \nabla \mathbf{m}(\mathbf{r}).$$

3) Summary of the exchange field forms

In summary, two different forms of the exchange field in inhomogeneous ferromagnetic materials have been obtained from the Heisenberg Hamiltonian in the linear approximation:

$$\begin{aligned}
&\textbf{Form I:} \quad \mathbf{H}^{\mathrm{I}}_{\mathrm{ex}}(\mathbf{r}) = \nabla \cdot l^2_{\mathrm{ex,I}}(\mathbf{r}) \nabla \frac{\mathbf{m}(\mathbf{r})}{M_{\mathrm{S}}(\mathbf{r})}, \quad \text{where} \quad l^2_{\mathrm{ex,I}}(\mathbf{r}) = \frac{2A(\mathbf{r})}{\mu_0 M_{\mathrm{S}}(\mathbf{r})}; \\
&\textbf{Form II:} \quad \mathbf{H}^{\mathrm{II}}_{\mathrm{ex}}(\mathbf{r}) = \nabla \cdot l^2_{\mathrm{ex,II}}(\mathbf{r}) \nabla \mathbf{m}(\mathbf{r}), \quad \text{where} \quad l^2_{\mathrm{ex,II}}(\mathbf{r}) = \frac{2A(\mathbf{r})}{\mu_0 M^2_{\mathrm{S}}(\mathbf{r})}.
\end{aligned} \tag{27}$$

The exchange field can be written also in **Form III**, derived directly from the exchange energy functional (21) (independent of the form used) under the assumption of homogeneity of the material, i.e. for space-independent A and M_{S} assumed in the calculation of the functional derivative (23):

$$\textbf{Form III:} \quad \mathbf{H}^{\mathrm{III}}_{\mathrm{ex}}(\mathbf{r}) = \frac{l^2_{\mathrm{ex,I}}(\mathbf{r})}{M_{\mathrm{S}}(\mathbf{r})} \nabla^2 \mathbf{m}(\mathbf{r}). \tag{28}$$

Of the parameters $l^2_{\mathrm{ex,I}}(\mathbf{r})$ and $l^2_{\mathrm{ex,II}}(\mathbf{r})$ introduced above only the latter (related to **Form II**) has an additional physical meaning: its square root defines the exchange length [125]. In **Form III** the coefficient in the exchange field formula is the same as in **Form II**, but M_{S} is reduced in the calculation of the latter.

At this very point it is worthy of notice that the differential operators of the exchange field in (27) and (28) act on the dynamic component $\mathbf{m}(\mathbf{r})$ of the magnetization vector in **Forms II** and **III**, and on its normalized function $\mathbf{m}(\mathbf{r})/M_{\mathrm{S}}(\mathbf{r})$ in **Form I**. This should be kept in mind in the interpretation of the calculated SW spectra.

2. The plane wave method

The band structure of excitations in periodically modulated materials, including electronic, photonic, phononic and magnonic crystals, can be calculated by similar methods. The conceptual simplicity of the plane wave method (PWM) and its applicability to any type of lattice and any shape of scattering centers have made this technique one of the most popular tools commonly used for studying structures of these types [57, 90, 98, 122, 134, 135]. The method is being constantly improved, with its field of application extending to new problems. Recently the PWM has been employed for the calculation of the band structure of a variety of materials, including photonic and magnonic crystals composed of materials with energy dissipation or with frequency-dependent properties [136, 137], 1D and 2D MCs of finite thickness [127, 128], 2D antidot lattices (ADLs) based on a square lattice [45, 138], and 2D MCs with a point defect [139].

The main improvement of the PWM made in this thesis is adaptation of the method to *planar magnetic structures*, i.e. magnetic structures of finite thickness. Similarly to 1D and 2D crystals (see Fig. 1), planar magnetic structures are infinite in one plane, in which the magnetic parameters have a periodic distribution (Fig. 4). As mentioned in the Introduction, currently available fabrication techniques allow the realization of patterned magnetic films with a thickness less than 30 nm, a minimal modulation size below a hundred of nanometers in the film plane, and a total width attaining the micrometer range. Thus, the planar model is suitable for structures of this kind.

Let us consider an infinite planar MC consisting of a ferromagnetic thin film with magnetic parameters periodic in the film plane, or ferromagnetic rods arranged periodically in the air (or a nonmagnetic dielectric) with the rod axis oriented along the film thickness, as shown in Fig. 4. The rods are assumed to be homogeneous. An external magnetic field is applied in the plane of the studied structure along the $\hat{z}$-axis.

In the classical approach the dynamics of the magnetization vector $\mathbf{M}(\mathbf{r},t)$ with negligible damping is described by the Landau-Lifshitz (LL) equation:

$$\frac{\partial \mathbf{M}(\mathbf{r},t)}{\partial t} = \gamma\mu_0 \mathbf{M}(\mathbf{r},t) \times \mathbf{H}_{\text{eff}}(\mathbf{r},t), \tag{29}$$

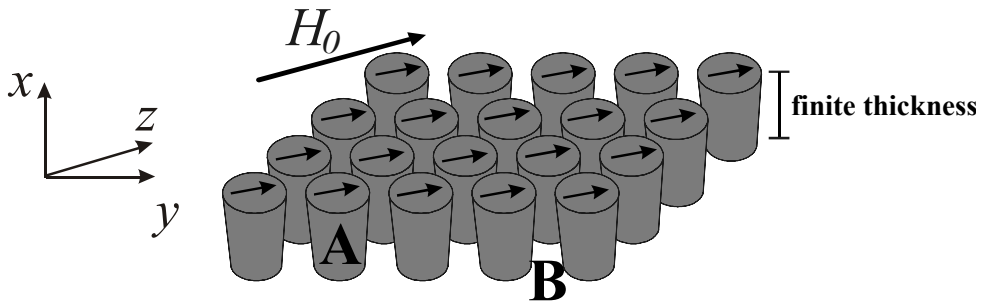

Figure 4. Schematic of a planar MC. The external magnetic field H_0 is applied along the $\hat{z}$ axis and assumed to be strong enough to induce the parallel alignment of all the magnetic moments.

where γ is the gyromagnetic ratio ($\gamma > 0$), μ_0 is the permeability of vacuum, and $\mathbf{H}_{\text{eff}}$ denotes the effective magnetic field acting on the magnetic moments. As in the case of free electrons, we shall assume $\gamma\mu_0 = 2.21 \times 10^5 (\text{ A/m})^{-1}\text{s}^{-1}$, unless otherwise stated.

The effective magnetic field $\mathbf{H}_{\text{eff}}$ is in general the sum of several components. On the assumption that the magnetocrystalline anisotropy is negligible within the studied structure, this field can be written as:

$$\mathbf{H}_{\text{eff}}(\mathbf{r},t) = \mathbf{H}_0(\mathbf{r},t) + \mathbf{H}_{\text{ex}}^{\Lambda}(\mathbf{r},t) + \mathbf{H}_{\text{ms}}(\mathbf{r},t). \tag{30}$$

The first term in (30) is the applied magnetic field $\mathbf{H}_0$. It is assumed to be homogeneous in space and strong enough to enforce the parallel alignment of all the magnetic moments. This allows to use the linear approximation, which implies small deviations $\mathbf{m}(\mathbf{r},t)$ of the magnetization from its ground state; thus, the magnetization vector can be written in the same form as in subsection 1.1: $\mathbf{M}(\mathbf{r},t) = M_z(\mathbf{r})\hat{z} + \mathbf{m}(\mathbf{r},t)$. Since $|\mathbf{m}(\mathbf{r},t)| \ll M_z(\mathbf{r})$, we can assume $M_z \approx M_{\text{S}}$, where M_{S} is the saturation magnetization. Since only monochromatic SWs are considered in this dissertation, the dynamic component of $\mathbf{M}(\mathbf{r},t)$ can be written as: $\mathbf{m}(\mathbf{r},t) = \mathbf{m}(\mathbf{r}) \cdot \exp(i\omega t)$, where ω is the SW angular frequency.

The second component of the effective field is the exchange field $\mathbf{H}_{\text{ex}}^{\Lambda}$. It can be defined in various forms, as already shown in subsection 1.1. Henceforth the symbol $\mathbf{H}_{\text{ex}}$ without any superscript will denote the exchange field calculated by **Form II** (27).

The last component of the effective field is the magnetostatic field. In the linear approximation it can be decomposed into the static and dynamic components, $\mathbf{H}(\mathbf{r})$ and $\mathbf{h}(\mathbf{r},t)$, respectively: $\mathbf{H}_{\text{ms}}(\mathbf{r},t) = \mathbf{H}(\mathbf{r}) + \mathbf{h}(\mathbf{r},t)$, where $|\mathbf{h}(\mathbf{r},t)| \ll \mathbf{H}(\mathbf{r},t)$. The time dependence of the dynamic component of the magnetostatic field has the same form as that of the dynamic component of the magnetization vector: $\mathbf{h}(\mathbf{r},t) = \mathbf{h}(\mathbf{r}) \cdot \exp(i\omega t)$. So far, only the dynamic magnetostatic field has been taken into account in the calculations of the SW spectra of 2D and 3D MCs (see, e.g., Refs. [92, 98, 124]). The main objective of this thesis is to extend the PWM in order to calculate the SW spectrum of thin

planar MCs. This can be achieved by taking into account the nonuniformity of the total magnetostatic field in the system.

In the linear approximation the following system of equations can be obtained from (29):

$$i\frac{\omega}{\gamma\mu_0}\xi_\Lambda(\mathbf{r})m_x(\mathbf{r}) + \hat{H}^\Lambda_{\text{ex}}\left[\xi_\Lambda(\mathbf{r})m_y(\mathbf{r})\right] - \xi_\Lambda(\mathbf{r})m_y(\mathbf{r})(H_0 + H_z(\mathbf{r})) + M_{\text{S}}(\mathbf{r})\cdot\left[\xi_\Lambda(\mathbf{r})h_y(\mathbf{r})\right] = 0, \tag{31a}$$

$$i\frac{\omega}{\gamma\mu_0}\xi_\Lambda(\mathbf{r})m_y(\mathbf{r}) - \hat{H}^\Lambda_{\text{ex}}\left[\xi_\Lambda(\mathbf{r})m_x(\mathbf{r})\right] + \xi_\Lambda(\mathbf{r})m_x(\mathbf{r})(H_0 + H_z(\mathbf{r})) - M_{\text{S}}(\mathbf{r})\cdot\left[\xi_\Lambda(\mathbf{r})h_x(\mathbf{r})\right] = 0, \tag{31b}$$

where the operator $\hat{H}^\Lambda_{\text{ex}}$ and coefficient $\xi_\Lambda(\mathbf{r})$ are defined by the form $\Lambda = \text{I, II or III}$ of the exchange field in (27) and (28):

$$\begin{aligned}
&\hat{H}^{\text{I}}_{\text{ex}} = \nabla\cdot l^2_{\text{ex,I}}(\mathbf{r})\nabla, && \xi_{\text{I}}(\mathbf{r}) = \frac{1}{M_{\text{S}}(\mathbf{r})};\\
&\hat{H}^{\text{II}}_{\text{ex}} = M_{\text{S}}(\mathbf{r})\nabla\cdot l^2_{\text{ex,II}}(\mathbf{r})\nabla, && \xi_{\text{II}}(\mathbf{r}) = 1;\\
&\hat{H}^{\text{III}}_{\text{ex}} = l^2_{\text{ex,I}}\nabla^2, && \xi_{\text{III}}(\mathbf{r}) = 1.
\end{aligned} \tag{32}$$

The static demagnetizing field in equations (31) is assumed to have only one nonzero component, H_z, along the direction of the external field. The other two components, H_x and H_y, must be neglected for the equations to be consistent under the approximations used. The material parameters A and M_{S}, and consequently $l^2_{\text{ex},\Lambda}$, in the system of equations (31) are periodic functions of the position vector $\mathbf{r}_{||} = (y, z)$, with a period equal to the lattice vector $\mathbf{a}_\parallel$. Thus, we can perform the Fourier transformation to map these periodic functions to the reciprocal space:

$$M_{\text{S}}(\mathbf{r}_\parallel) = \sum_{\mathbf{G}_\parallel} M_{\text{S}}(\mathbf{G}_\parallel)e^{i\mathbf{G}_\parallel\cdot\mathbf{r}_\parallel}, \tag{33a}$$

$$l^2_{\text{ex},\Lambda}(\mathbf{r}_\parallel) = \sum_{\mathbf{G}_\parallel} l^2_{\text{ex},\Lambda}(\mathbf{G}_\parallel)e^{i\mathbf{G}_\parallel\cdot\mathbf{r}_\parallel}, \tag{33b}$$

where $\mathbf{G}_\parallel = (G_y, G_z)$ denotes a reciprocal lattice vector of the considered structure. The Fourier coefficients $M_\mathrm{S}(\mathbf{G}_\parallel)$ and $l^2_{\mathrm{ex},\Lambda}(\mathbf{G}_\parallel)$ of the respective material parameters can be found from the inverse transformation:

$$M_\mathrm{S}(\mathbf{G}_\parallel) = \frac{1}{V_c}\int\limits_{V_c} M_\mathrm{S}(\mathbf{r}_\parallel) e^{-i\mathbf{G}_\parallel\cdot\mathbf{r}_\parallel} d^3 r_\parallel, \tag{34a}$$

$$l^2_{\mathrm{ex},\Lambda}(\mathbf{G}_\parallel) = \frac{1}{V_c}\int\limits_{V_c} l^2_{\mathrm{ex},\Lambda}(\mathbf{r}_\parallel) e^{-i\mathbf{G}_\parallel\cdot\mathbf{r}_\parallel} d^3 r_\parallel. \tag{34b}$$

The coefficients can be either calculated by integration over the unit cell volume V_c or determined numerically by means of the fast Fourier transform in a procedure similar to that used for the determination of photonic band structures [57].

The Bloch's theorem is used in the solution of the system of equations (31). This theorem asserts that a solution of a differential equation with periodic coefficients can be represented as the product of a plane wave envelope function and a periodic function $\mathbf{m}_{\mathbf{k}_\parallel}(\mathbf{G}_\parallel)$:

$$\mathbf{m}(\mathbf{r}_\parallel) = \sum_{\mathbf{G}_\parallel} \mathbf{m}_{\mathbf{k}_\parallel}(\mathbf{G}_\parallel) e^{i(\mathbf{k}_\parallel+\mathbf{G}_\parallel)\cdot\mathbf{r}_\parallel}, \tag{35}$$

where $\mathbf{k}_\parallel = (k_y, k_z)$ is the Bloch wave vector of the SW. In the case when the first form of the exchange energy is used, i.e. $\Lambda = \mathrm{I}$, formula (35) will read:

$$\xi_\mathrm{I}(\mathbf{r}_\parallel)\mathbf{m}(\mathbf{r}_\parallel) \equiv \frac{\mathbf{m}(\mathbf{r}_\parallel)}{M_\mathrm{S}(\mathbf{r}_\parallel)} \equiv \tilde{\mathbf{m}}(\mathbf{r}_\parallel) = \sum_{\mathbf{G}_\parallel} \tilde{\mathbf{m}}_{\mathbf{k}_\parallel}(\mathbf{G}_\parallel) e^{i(\mathbf{k}_\parallel+\mathbf{G}_\parallel)\cdot\mathbf{r}_\parallel}. \tag{36}$$

To finalize the formalism in which an eigenvalue problem in the reciprocal space is derived from the system of equations (31) one needs to calculate the magnetostatic field $\mathbf{H}_\mathrm{ms}(\mathbf{r}_\parallel, t)$.

2.1. Calculation of the magnetostatic field

As it was mentioned in Introduction the strong and short range exchange interaction is responsible for the magnetic ordering. However there is another type of relatively weak but important magnetic interaction that should be considered as well. It is based on the interactions between magnetic moments of the atoms within a magnetic sample and is known as magnetostatic interaction.

The magnetostatic self-energy called also demagnetizing energy of a body of volume V and magnetization $\mathbf{M}(\mathbf{r})$ can be written

$$E = -\frac{1}{2}\int_V \mathbf{M}(\mathbf{r}) \cdot \mathbf{H}_{\rm ms}(\mathbf{r}) d^3 r, \tag{37}$$

where $\mathbf{H}_{\rm ms}(\mathbf{r})$ is the internal magnetic field due to magnetization itself. This field can be obtained by solving the magnetostatic Maxwell equations with appropriate boundary conditions, as given by:

$$\begin{aligned} \nabla \times \mathbf{H}_{\rm ms}(\mathbf{r}) = 0, \\ \nabla \cdot (\mathbf{H}_{\rm ms}(\mathbf{r}) + \mathbf{M}(\mathbf{r})) = 0. \end{aligned} \tag{38}$$

One can solve this system of equations introducing the magnetostatic potential:

$$\mathbf{H}_{\rm ms}(\mathbf{r}) = -\nabla U(\mathbf{r}), \tag{39}$$

where this potential is given by (see, e.g. [2])

$$U(\mathbf{r}) = -\int_V \mathbf{M}(\mathbf{r}') \cdot \nabla \frac{1}{|\mathbf{r} - \mathbf{r}'|} d^3 r' \tag{40}$$

and the gradient is taken with respect to the point $\mathbf{r}$.

If the sample is uniformly magnetized, i.e., $\mathbf{M}(\mathbf{r}) = \text{const}$ then the magnetostatic field in (39) can be written as follows

$$\mathbf{H}_{\rm ms}(\mathbf{r}) = \nabla \cdot (\mathbf{M}\nabla) \int_V \frac{d^3 r'}{|\mathbf{r} - \mathbf{r}'|} = -\hat{N}(\mathbf{r})\mathbf{M}, \tag{41}$$

where $\hat{N}(\mathbf{r})$ is known as the demagnetizing tensor. Its components can be evaluated using

$$\hat{N}_{ij}(\mathbf{r}) = -\frac{\partial^2}{\partial x_i \partial x_j} \int_V \frac{d^3 r'}{|\mathbf{r} - \mathbf{r}'|}, \tag{42}$$

so that the demagnetizing factors of a ferromagnetic sample depend only on its shape.

For a ferromagnetic body with a spatial distribution of magnetization, the problem of finding the magnetostatic field is a far more complicated task. It has been solved analytically, e.g., for a periodic lattice of infinitely long magnetic needles of rectangular cross section [140, 141], for some particular cases of heterogeneous films with columnar structure [142, 143] and planar assemblies of ferromagnetic nanoparticles embedded in a nonmagnetic matrix [144], and for multilayers [145]. The magnetostatic energy and shape anisotropy for an ellipsoidal matrix containing magnetic particles regularly spaced forming a 3D array were considered by Dubowik in [146]. Using the mean-field approach

he obtained approximate expressions containing both macroscopic and microscopic demagnetizing tensors and considered particular cases of these expressions for magnetic multilayers, granular films, etc.

A derivation of the exact solution of the magnetostatic field in the general case of a planar 2D MC of a finite thickness was performed in [142] using the Poisson method. Its main idea is based on the similarity of the magnetostatic and electrostatic equations that lead to the simple relation between the respective potentials and the boundary conditions applied to them. This method gives the rigorous solution of the problem when the MC is surrounded by dielectric. In the case of a metallic coating the boundary conditions for the static and dynamic components of the demagnetizing field become different and asymmetric (if metal covers only one side of the structure), and therefore this technique can not be applied to the both of them simultaneously.

Here, a method that allows to derive analytically both components of the magnetostatic field in the case of a 2D MC with planar geometry is presented. The proposed method can be applied also for the planar structures covered by different types of overlayers what will be shown in subsection 3.4.

In the magnetostatic approximation both the dynamic and static components of the demagnetizing field $\mathbf{H}_{\mathrm{ms}}(\mathbf{r},t) = \mathbf{H}(\mathbf{r}) + \mathbf{h}(\mathbf{r}) \cdot \exp(i\omega t)$ in the considered MC must fulfill Maxwell's equations (38):

$$\begin{array}{cc} \nabla \times \mathbf{H}(\mathbf{r}) = 0 & \nabla \times \mathbf{h}(\mathbf{r}) = 0 \\ \text{and} & \\ \nabla \cdot (\mathbf{H}(\mathbf{r}) + M_{\mathrm{S}}(\mathbf{r}_{\parallel}) \cdot \hat{z}) = 0 & \nabla \cdot (\mathbf{h}(\mathbf{r}) + \mathbf{m}(\mathbf{r}_{\parallel})) = 0. \end{array} \tag{43}$$

The solution of this system of equations requires the determination of the boundary conditions on the surfaces of the slab. Applicable in this case, the standard electromagnetic boundary conditions assert the continuity of the tangential component of the magnetic field and the normal component of the magnetic induction at the interfaces.

According to (43), magnetostatic potentials can be introduced for both components of the magnetic field:

$$\mathbf{H}(\mathbf{r}) = -\nabla\varphi(\mathbf{r}) \quad \text{and} \quad \mathbf{h}(\mathbf{r}) = -\nabla\psi(\mathbf{r}). \tag{44}$$

By using these expressions the boundary conditions can be written as:

$$\begin{aligned} \chi_i(\mathbf{r})\Big|_{x=\pm\frac{d}{2}} &= \chi_e(\mathbf{r})\Big|_{x=\pm\frac{d}{2}}, \\ \frac{\partial\chi_i(\mathbf{r})}{\partial x}\Big|_{x=\pm\frac{d}{2}} &= \frac{\partial\chi_e(\mathbf{r})}{\partial x}\Big|_{x=\pm\frac{d}{2}}, \end{aligned} \tag{45}$$

where d is the thickness of the considered MC, χ denotes any of the magnetostatic potentials φ or ψ, and the indices i and e refer to the interior and exterior of the studied structure, respectively. Since both the equations and the boundary conditions for the static and dynamic components of the magnetostatic field are similar, below we shall only present the derivation of the static component of $\mathbf{H}_{\text{ms}}(\mathbf{r},t)$.

The substitution of (44) into (43) leads to the following system of equations for the magnetostatic potential $\varphi(\mathbf{r}_\parallel)$:

$$\begin{aligned} &\Delta\varphi_i(\mathbf{r}) = \frac{\partial M_{\text{S}}(\mathbf{r}_\parallel)}{\partial z} && \text{in the MC;} \\ &\Delta\varphi_e(\mathbf{r}) = 0 && \text{beyond the MC.} \end{aligned} \tag{46}$$

Because of the periodic distribution of the static magnetization $M_{\text{S}}(\mathbf{r}_\parallel)$ (see the equation (33a)) within the considered MC the sought solutions of this system of equations have the form:

$$\varphi_{i,e}(\mathbf{r}) = \sum_{\mathbf{G}_\parallel} \varphi_{i,e}(x,\mathbf{G}_\parallel) e^{i\mathbf{G}_\parallel\cdot\mathbf{r}_\parallel}. \tag{47}$$

The substitution of (33a) and (47) into (46) leads to the system of differential equations:

$$\frac{\partial^2\varphi_i(x,\mathbf{G}_\parallel)}{\partial x^2} - \mathbf{G}^2\varphi_i(x,\mathbf{G}_\parallel) - iG_z M_{\text{S}}(\mathbf{G}) = 0, \tag{48a}$$

$$\frac{\partial^2\varphi_e(x,\mathbf{G}_\parallel)}{\partial x^2} - \mathbf{G}^2\varphi_e(x,\mathbf{G}_\parallel) = 0. \tag{48b}$$

Note that we only seek solutions of (46) valid for arbitrary coordinate $\mathbf{r}_\parallel$ in the plane of the studied MC.

As implied by the theory of differential equations, the general solution of (48a) can be constructed from the fundamental system of the corresponding homogeneous equation and one particular solution of the inhomogeneous equation. For the equations (48) it reads:

$$\varphi_i(x,\mathbf{G}_\parallel) = A_1 \mathrm{e}^{|\mathbf{G}_\parallel|x} + A_2 \mathrm{e}^{-|\mathbf{G}_\parallel|x} - \frac{iG_z}{\mathbf{G}_\parallel^2} M_\mathrm{S}(\mathbf{G}_\parallel), \tag{49a}$$

$$\varphi_e(x,\mathbf{G}_\parallel) = B_1 \mathrm{e}^{|\mathbf{G}_\parallel|x} + B_2 \mathrm{e}^{-|\mathbf{G}_\parallel|x}, \tag{49b}$$

where A_1, A_2 and B_1, B_2 are undefined constants of integration. The magnetostatic potential φ_e beyond the considered structure should be finite when $x \to \pm\infty$. This imposes restrictions on the constants B_1 and B_2. Thus, φ_e in (49b) for two semispaces, $x > 0$ and $x < 0$, can be written as:

$$\begin{aligned} \varphi_e^{(x>0)}(x,\mathbf{G}_\parallel) &= B_2 \mathrm{e}^{-|\mathbf{G}_\parallel|x}, \\ \varphi_e^{(x<0)}(x,\mathbf{G}_\parallel) &= B_1 \mathrm{e}^{|\mathbf{G}_\parallel|x}. \end{aligned} \tag{50}$$

By substituting the solutions (49) and (50) into the boundary conditions (45) we obtain the following system of algebraic equations for the integration constants:

$$\begin{cases} A_1 \mathrm{e}^{|\mathbf{G}_\parallel|d/2} + A_2 \mathrm{e}^{-|\mathbf{G}_\parallel|d/2} - \dfrac{iG_z}{\mathbf{G}_\parallel^2} M_\mathrm{S}(\mathbf{G}_\parallel) = B_2 \mathrm{e}^{-|\mathbf{G}_\parallel|d/2}, \\ A_1 \mathrm{e}^{|\mathbf{G}_\parallel|d/2} - A_2 \mathrm{e}^{-|\mathbf{G}_\parallel|d/2} = -B_2 \mathrm{e}^{-|\mathbf{G}_\parallel|d/2}, \end{cases} \tag{51}$$

at $x = d/2$, and

$$\begin{cases} A_1 \mathrm{e}^{-|\mathbf{G}_\parallel|d/2} + A_2 \mathrm{e}^{|\mathbf{G}_\parallel|d/2} - \dfrac{iG_z}{\mathbf{G}_\parallel^2} M_\mathrm{S}(\mathbf{G}_\parallel) = B_1 \mathrm{e}^{-|\mathbf{G}_\parallel|d/2}, \\ A_1 \mathrm{e}^{-|\mathbf{G}_\parallel|d/2} - A_2 \mathrm{e}^{|\mathbf{G}_\parallel|d/2} = B_1 \mathrm{e}^{-|\mathbf{G}_\parallel|d/2}, \end{cases} \tag{52}$$

at $x = -d/2$. The simultaneous solution of these two systems of equations yields the coefficients A_1, A_2, B_1 and B_2. Using (49a) the magnetostatic potential within the studied MC can be written as follows:

$$\varphi_i(\mathbf{r}) = \sum_{\mathbf{G}_\parallel} \frac{iG_z}{\mathbf{G}_\parallel^2} M_\mathrm{S}(\mathbf{G}_\parallel) \left(1 - \mathrm{e}^{-|\mathbf{G}_\parallel|d/2} \cosh\left(|\mathbf{G}_\parallel|x\right)\right) \mathrm{e}^{i\mathbf{G}_\parallel \cdot \mathbf{r}_\parallel}. \tag{53}$$

The scalar magnetic potential $\psi(\mathbf{r})$ of the dynamic component of the demagnetizing field $\mathbf{h}(\mathbf{r})$ can be derived in a similar way, and reads:

$$\psi_i(\mathbf{r}) = \sum_{\mathbf{G}_\parallel} \left[\frac{m_{x,\mathbf{k}_\parallel}(\mathbf{G}_\parallel)}{|\mathbf{k}_\parallel + \mathbf{G}_\parallel|} \mathrm{e}^{-|\mathbf{k}_\parallel+\mathbf{G}_\parallel|d/2} \sinh\left(|\mathbf{k}_\parallel + \mathbf{G}_\parallel|x\right) \right.$$
$$\left. - \frac{i(k_y + G_y)}{|\mathbf{k}_\parallel + \mathbf{G}_\parallel|^2} m_{y,\mathbf{k}_\parallel}(\mathbf{G}_\parallel) \left[1 - \mathrm{e}^{-|\mathbf{k}_\parallel+\mathbf{G}_\parallel|d/2} \cosh\left(|\mathbf{k}_\parallel + \mathbf{G}_\parallel|x\right)\right] \right] \mathrm{e}^{i(\mathbf{k}_\parallel+\mathbf{G}_\parallel)\cdot\mathbf{r}_\parallel}. \quad (54)$$

By using (44) the magnetic field in the considered MC can be obtained from (53) and (54) as a function of the magnetization vector[3]:

$$H_z(\mathbf{r}_\parallel, x) = -\sum_{\mathbf{G}_\parallel} \frac{G_z^2}{\mathbf{G}_\parallel^2} M_\mathrm{S}(\mathbf{G}_\parallel) \left(1 - \cosh\left(|\mathbf{G}_\parallel|x|\right)\mathrm{e}^{-|\mathbf{G}_\parallel|d/2}\right) \mathrm{e}^{i\mathbf{G}_\parallel\cdot\mathbf{r}_\parallel}, \quad (55a)$$

$$h_x(\mathbf{r}_\parallel, x) = -\sum_{\mathbf{G}_\parallel} m_{x,\mathbf{k}_\parallel}(\mathbf{G}_\parallel) \cosh\left(|\mathbf{k}_\parallel + \mathbf{G}_\parallel|x\right)\mathrm{e}^{-|\mathbf{k}_\parallel+\mathbf{G}_\parallel|d/2} \mathrm{e}^{i(\mathbf{k}_\parallel+\mathbf{G}_\parallel)\cdot\mathbf{r}_\parallel}, \quad (55b)$$

$$h_y(\mathbf{r}_\parallel, x) = -\sum_{\mathbf{G}_\parallel} \frac{(k_y + G_y)^2}{|\mathbf{k}_\parallel + \mathbf{G}_\parallel|^2} m_{y,\mathbf{k}_\parallel}(\mathbf{G}_\parallel) \left(1 - \cosh\left(|\mathbf{k}_\parallel + \mathbf{G}_\parallel|x\right)\mathrm{e}^{-|\mathbf{k}_\parallel+\mathbf{G}_\parallel|d/2}\right) \mathrm{e}^{i(\mathbf{k}_\parallel+\mathbf{G}_\parallel)\cdot\mathbf{r}_\parallel}. \quad (55c)$$

Both the dynamic and static components of the magnetostatic field are assumed to depend only on the same component of the magnetization vector. This result coincides with the one obtained in [142] under the considered assumption.

In the above formulas the magnetostatic field depends on the position along the $\hat{x}$-axis and fulfills standard electromagnetic boundary conditions on the slab surfaces. When the slab is thin enough the nonuniformity of the magnetostatic field across its thickness can be assumed to have a minor effect on the low-frequency SWs (more detailed analysis of the considered assumption is given in section 3.7). Thus, the magnetostatic field in the LL equation (31) can be assumed to have a constant value equal to its actual value in the middle of the slab, i.e. for $x = 0$. However, this assumption is restricted by the condition that the wavelength of the SW should be much greater than the thickness of the slab. The parts of the dispersion corresponding to large wave vectors are folded to the first Brillouin zone and form bands of higher frequency. Thus, our approximation assuming a uniform dynamic magnetization along the $\hat{x}$-axis only applies to the first few low-frequency bands of sufficiently thin planar MCs.

[3] Formulas for a normalized value $\tilde{\mathbf{h}}(\mathbf{r}) \equiv \mathbf{h}(\mathbf{r})/M_\mathrm{S}(\mathbf{r}_\parallel)$ of the dynamic component of the demagnetizing field will have the same form. It can be shown in the following way: $0 = \nabla \cdot \left[M_\mathrm{S}(\mathbf{r}_\parallel)\left(\tilde{\mathbf{h}}(\mathbf{r}) + \tilde{\mathbf{m}}(\mathbf{r}_\parallel)\right)\right] = \left(\nabla M_\mathrm{S}(\mathbf{r}_\parallel)\right) \cdot \left(\tilde{\mathbf{h}}(\mathbf{r}) + \tilde{\mathbf{m}}(\mathbf{r}_\parallel)\right) + M_\mathrm{S}(\mathbf{r}_\parallel)\nabla \cdot \left(\tilde{\mathbf{h}}(\mathbf{r}) + \tilde{\mathbf{m}}(\mathbf{r}_\parallel)\right) \approx M_\mathrm{S}(\mathbf{r}_\parallel)\left(\tilde{\mathbf{h}}(\mathbf{r}) + \tilde{\mathbf{m}}(\mathbf{r}_\parallel)\right)$, where similarly to (19) the component with $\nabla M_\mathrm{S}(\mathbf{r}_\parallel)$ is neglected.

2.2. Final algebraic eigenvalue problem

Because of its Fourier form the solution (55) can be used directly in the PWM. The substitution of equations (33), (35) and (55) into (31) leads to the eigenvalue problem with eigenvalues $i\omega/\gamma\mu_0 H_0$:

$$\hat{M}_\Lambda \mathbf{m}_{\mathbf{k}_\parallel,\Lambda} = i\frac{\omega}{\gamma\mu_0 H_0}\mathbf{m}_{\mathbf{k}_\parallel,\Lambda}, \tag{56}$$

where the eigenvector depends on the form of the exchange field: $\mathbf{m}^{\mathrm{T}}_{\mathbf{k}_\parallel,\Lambda} = \left[m_{x,\mathbf{k}_\parallel}(\mathbf{G}_{\parallel,1}),\cdots,m_{x,\mathbf{k}_\parallel}(\mathbf{G}_{\parallel,N}),m_{y,\mathbf{k}_\parallel}(\mathbf{G}_{\parallel,1}),\cdots,m_{y,\mathbf{k}_\parallel}(\mathbf{G}_{\parallel,N})\right]$ for $\Lambda = \mathrm{II}, \mathrm{III}$; and $\mathbf{m}^{\mathrm{T}}_{\mathbf{k}_\parallel,\mathrm{I}} = \left[\tilde{m}_{x,\mathbf{k}_\parallel}(\mathbf{G}_{\parallel,1}),\cdots,\tilde{m}_{x,\mathbf{k}_\parallel}(\mathbf{G}_{\parallel,N}),\tilde{m}_{y,\mathbf{k}_\parallel}(\mathbf{G}_{\parallel,1}),\cdots,\tilde{m}_{y,\mathbf{k}_\parallel}(\mathbf{G}_{\parallel,N})\right]$ for $\Lambda = \mathrm{I}$. A finite number N of reciprocal lattice vectors is used here and in (33)-(35). The matrix of this eigenvalue problem has the form of a block matrix:

$$\hat{M}_\Lambda = \begin{pmatrix} \hat{M}_\Lambda{}^{xx} & \hat{M}_\Lambda{}^{xy} \\ \hat{M}_\Lambda{}^{yx} & \hat{M}_\Lambda{}^{yy} \end{pmatrix}. \tag{57}$$

The submatrices in (57) are:

$$\hat{M}^{xx}_{ij} = \hat{M}^{yy}_{ij} = 0, \tag{58a}$$

$$\hat{M}^{xy}_{ij} = \delta_{ij} + M^{\mathrm{ex},\Lambda}_{i,j} - \frac{(G_{z,i}-G_{z,j})^2}{H_0|\mathbf{G}_{\parallel,i}-\mathbf{G}_{\parallel,j}|^2}M_{\mathrm{S}}(\mathbf{G}_{\parallel,i}-\mathbf{G}_{\parallel,j})(1-C(\mathbf{G}_{\parallel,i}-\mathbf{G}_{\parallel,j},x)) + \frac{(k_y+G_{y,j})^2}{H_0|\mathbf{k}_\parallel+\mathbf{G}_{\parallel,j}|^2}M_{\mathrm{S}}(\mathbf{G}_{\parallel,i}-\mathbf{G}_{\parallel,j})(1-C(\mathbf{k}_\parallel+\mathbf{G}_{\parallel,j},x)), \tag{58b}$$

$$\hat{M}^{yx}_{ij} = -\delta_{ij} - M^{\mathrm{ex},\Lambda}_{i,j} + \frac{(G_{z,i}-G_{z,j})^2}{H_0|\mathbf{G}_{\parallel,i}-\mathbf{G}_{\parallel,j}|^2}M_{\mathrm{S}}(\mathbf{G}_{\parallel,i}-\mathbf{G}_{\parallel,j})(1-C(\mathbf{G}_{\parallel,i}-\mathbf{G}_{\parallel,j},x)) - \frac{1}{H_0}M_{\mathrm{S}}(\mathbf{G}_{\parallel,i}-\mathbf{G}_{\parallel,j})C(\mathbf{k}_\parallel+\mathbf{G}_{\parallel,j},x), \tag{58c}$$

where the reciprocal lattice vector indices i,j,l are integers in the range $\langle 1,N\rangle$. The function $C(\mathbf{k}_\parallel,x)$ in the above equations is defined as:

$$C(\mathbf{k}_\parallel,x) = \cosh\left(|\mathbf{k}_\parallel|x\right)\mathrm{e}^{-|\mathbf{k}_\parallel|d/2}. \tag{59}$$

The matrix elements $M_{i,j}^{\mathrm{ex},\Lambda}$ related to the exchange field depend on its form, and read:

$$M_{i,j}^{\mathrm{ex,I}} = \frac{(\mathbf{k}_\parallel + \mathbf{G}_{\parallel,i}) \cdot (\mathbf{k}_\parallel + \mathbf{G}_{\parallel,j})}{H_0} l_{\mathrm{ex,I}}^2 (\mathbf{G}_{\parallel,i} - \mathbf{G}_{\parallel,j}), \tag{60a}$$

$$M_{i,j}^{\mathrm{ex,II}} = \sum_l \frac{(\mathbf{k}_\parallel + \mathbf{G}_{\parallel,j}) \cdot (\mathbf{k}_\parallel + \mathbf{G}_{\parallel,l})}{H_0} l_{\mathrm{ex,II}}^2 (\mathbf{G}_{\parallel,l} - \mathbf{G}_j) M_{\mathrm{S}} (\mathbf{G}_{\parallel,i} - \mathbf{G}_{\parallel,l}) \tag{60b}$$

$$M_{i,j}^{\mathrm{ex,III}} = \frac{(\mathbf{k}_\parallel + \mathbf{G}_{\parallel,j})^2}{H_0} l_{\mathrm{ex,I}}^2 (\mathbf{G}_{\parallel,i} - \mathbf{G}_{\parallel,j}). \tag{60c}$$

We shall solve the eigenvalue problem (56) by standard numerical routines designed for solving complex eigenvalue problems. All the eigenvalues found by these procedures must be tested for convergence.

In summary, the magnetostatic field has been analytically calculated in the form of Fourier series as a function of the magnetization vector for the general case of a planar 2D MC. Using several approximations the obtained result has been successfully implemented to the PWM calculations of the SW spectrum of the considered MC.

3. Propagation of SWs in planar MCs

3.1. Influence of different forms of the exchange field on the band structure of MCs

Let us consider a 1D MC consisting of cobalt (Co) and permalloy (Py) nanostripes of equal width $s = 250$ nm and thickness $d = 30$ nm (see Fig. 5). The length of the stripes is assumed to be infinite. This choice is motivated by recently published papers presenting experimental and theoretical results for similar structures [42, 43, 127, 147, 148]. The dispersion relation of SWs in such kind of crystals was measured by Brillouin Light Scattering spectroscopy and was calculated from the LL equation using the finite element method and the PWM. Very weak magnetic field, $\mu H_0 = 0.001$ T is applied along the stripes.

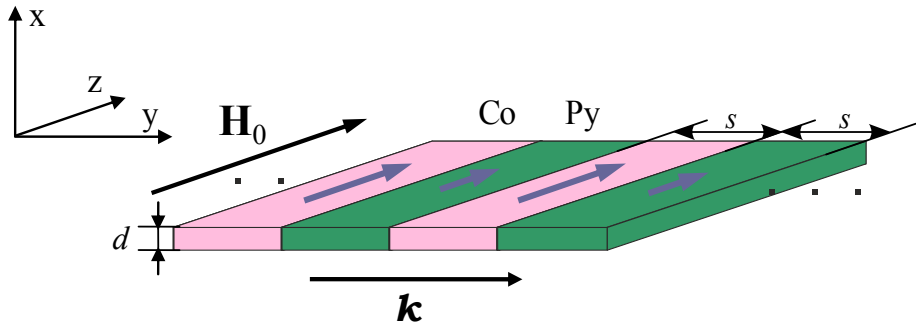

Figure 5. Geometry of the studied MC. Thickness of the Py and Co nanostripes is $d = 30$ nm, while its width is $s = 250$ nm. A magnetic field $\mathbf{H}_0$ is applied along the stripes length, $\mathbf{k}$ is the wave vector of the spin waves.

For the structure shown in Fig. 5 the demagnetizing field (55) will read:

$$\begin{aligned} H_z(x,y) &= 0, \\ h_x(x,y) &= -\sum_{G_y} m_{x,k_y}(G_y)\cosh\left((k_y+G_y)x\right)\mathrm{e}^{-(k_y+G_y)d/2}\mathrm{e}^{i(k_y+G_y)y}, \\ h_y(x,y) &= -\sum_{G_y} m_{y,k_y}(G_y)\left(1-\mathrm{e}^{-(k_y+G_y)d/2}\cosh\left((k_y+G_y)x\right)\right)\mathrm{e}^{i(k_y+G_y)y}, \end{aligned} \tag{61}$$

where a reciprocal lattice vector of the considered structure is $\mathbf{G}_{\parallel} = (G_y, G_z) = (\pi n_y/s, 0)$ (n_y is an integer), k_y is a Bloch wave vector of SWs propagating along the $\hat{y}$-axis. Then the submatrices in (58) of the eigenvalue problem (56) can be simplified as follows:

$$\begin{aligned} \hat{M}_{ij}^{xx} &= \hat{M}_{ij}^{yy} = 0, \\ \hat{M}_{ij}^{xy} &= \delta_{ij} + M_{i,j}^{\mathrm{ex},\Lambda} + \frac{1}{H_0}\left(1 - \mathrm{e}^{-(k_y+G_{y,j})d/2}\right) M_{\mathrm{S}}(G_{y,i} - G_{y,j}), \\ \hat{M}_{ij}^{yx} &= -\delta_{ij} - M_{i,j}^{\mathrm{ex},\Lambda} - \frac{1}{H_0}\mathrm{e}^{-(k_y+G_{y,j})d/2} M_{\mathrm{S}}(G_{y,i} - G_{y,j}), \end{aligned} \tag{62}$$

where the element connected with the exchange field, $M_{i,j}^{\mathrm{ex},\Lambda}$ for the considered MC can be written in the following form:

$$\begin{aligned} M_{i,j}^{\mathrm{ex,I}} &= \frac{(k_y + G_{y,j}) \cdot (k_y + G_{y,i})}{H_0} l_{\mathrm{ex,I}}^2 (G_{y,i} - G_{y,j}), \\ M_{i,j}^{\mathrm{ex,II}} &= \sum_l \frac{(k_y + G_{y,j}) \cdot (k_y + G_{y,l})}{H_0} l_{\mathrm{ex,II}}^2 (G_{y,l} - G_{y,j}) M_{\mathrm{S}}(G_{y,i} - G_{y,l}), \\ M_{i,j}^{\mathrm{ex,III}} &= \frac{(k_y + G_{y,j})^2}{H_0} l_{\mathrm{ex,I}}^2 (G_{y,i} - G_{y,j}). \end{aligned} \tag{63}$$

As before a finite number N of the reciprocal lattice vectors is used here and, hence $i, j, l = \langle 1, N \rangle$. In order to solve the obtained eigenproblem numerically, we have to calculate the Fourier coefficients of the material parameters (34): the static magnetization and the exchange length squared. In the case of the studied 1D MC (see Fig. 5) it is possible to perform this integration analytically and obtain the following common formula:

$$X(G_y) = \begin{cases} \frac{1}{2}(X_{\mathrm{A}} - X_{\mathrm{B}}) + X_{\mathrm{B}}, & \text{for } G_y = 0 \\ \frac{1}{G_y s}(X_{\mathrm{A}} - X_{\mathrm{B}}) \sin G_y \frac{s}{2}, & \text{for } G_y \neq 0 \end{cases} \tag{64}$$

where X_{A} and X_{B} are the material parameters, i.e, M_{S} or $l_{\mathrm{ex},\Lambda}^2$ in the stripes A and B, respectively. Values of spontaneous magnetization and exchange constants of Co and Py are assumed to be equal to those presented in the experimental paper [42]. It is for Co: $M_{\mathrm{S,Co}} = 1.15 \cdot 10^6$ A/m, $A_{\mathrm{Co}} = 2.88 \cdot 10^{-11}$ J/m and for Py: $M_{\mathrm{S,Py}} = 0.658 \cdot 10^6$ A/m, $A_{\mathrm{Py}} = 1.1 \cdot 10^{-11}$ J/m. Average value for the gyromagnetic ratio (calculated from the values assumed in [42]) is considered, i.e., the same for Co and Py, $\gamma = 194.6$ GHz/T. Three types of lines in Fig. 6 represent the results of the calculations performed using the PWM for three different formulations of the exchange field taken from equations (27)-(28).

Additionally a convergence test to check the obtained results is performed (see Fig. 7. All eigenfrequencies are calculated for the wave vector $k = \pi/4s$. Second form of the

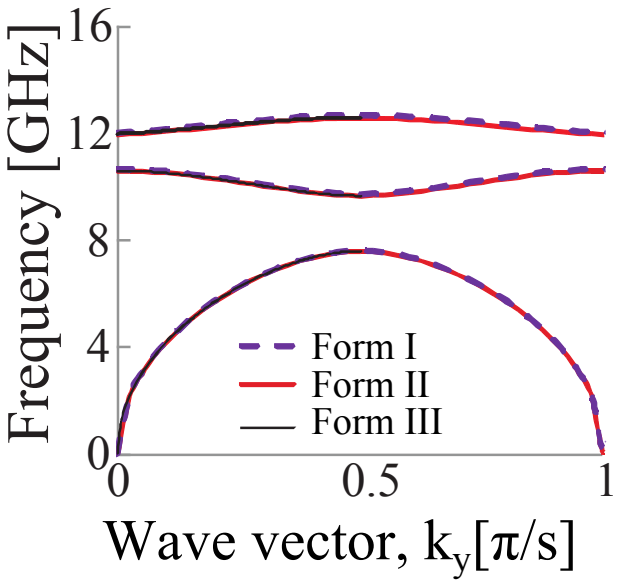

Figure 6. Magnonic band structures calculated for three different definitions of the exchange field (as defined in equations (27)-(28)) for a thin slab of the considered 1D MC. Very weak external magnetic field, $\mu_0 H_0 = 0.001$ T is directed along the stripes. The magnetostatic interaction determine the magnonic band structure — the definition of the H_{ex} is unimportant.

exchange field (27), i.e., $\Lambda = \text{II}$ is used in these calculations. As one can see a satisfactory convergence of the numerical solution of (56) for the considered MC is found when $N = 43$ reciprocal lattice vectors are used.

The dispersion relations calculated with the three different forms of the exchange field are overlapping almost perfectly (see Fig. 6). It means that the effect of exchange interactions between Co and Py is minor or even negligible for this structure. In the next subsection of this thesis more detailed investigation of nature of SWs in such MC will be done.

In order to observe effects connected with various definitions of the exchange field in nonuniform materials one needs to decrease the value of the magnetostatic interaction with respect to the exchange one. This can be done by decreasing a lattice constant. In Fig. 8 the magnonic band structure for the 1D MC with $s = 15$ nm width of Co and Py stripes is shown. Film thickness is changed to $d = 4$ nm. The rest of parameters are the same as in the previous calculation.

The differences connected with various definition of the exchange field start to be visible already near the Brillouin zone (BZ) border and for higher modes also at the center of the BZ. The most essential difference can be observed between SW dispersions calculated according to the **Form I** and **Forms II, III**. For the **Form I** (dashed line) the magnonic gap is absent between 1$^{\text{st}}$ and 2$^{\text{nd}}$ band, while for the other two formulations of H_{ex} the gap exists.

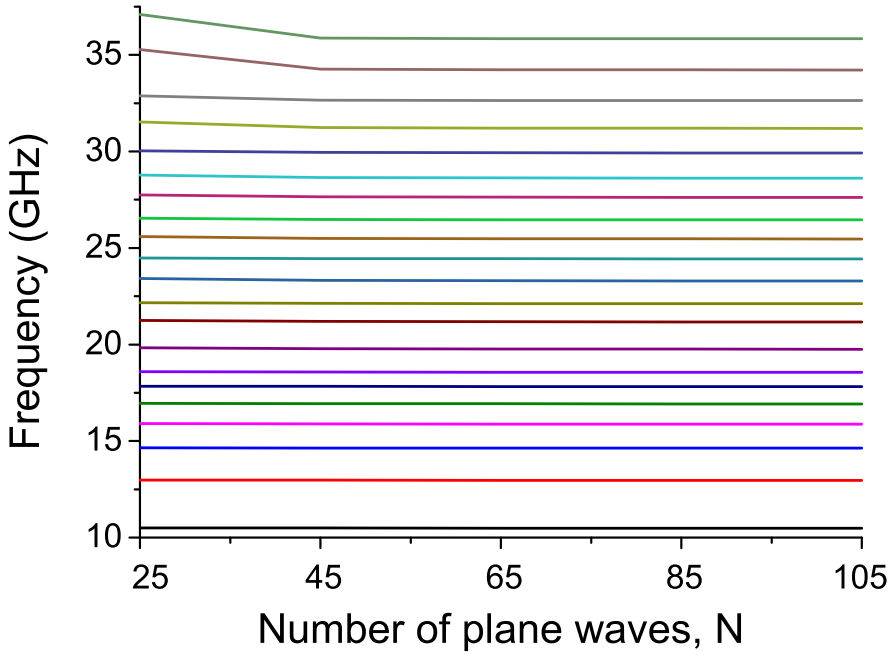

Figure 7. Convergence test of the eigenfrequencies of the considered MC given by (56). The frequencies of all the bands are calculated for the wave vector $k = \pi/4s$ and second form of the exchange field (27), i.e., $\Lambda = \mathrm{II}$. Sufficient convergence is observed for $N > 40$.

In Fig. 8(b) and (c) the profiles of dynamical magnetization and its first derivatives with respect to y are shown for three lowest modes. The profiles are very similar for all three forms of the exchange field. The shift of the 3$^{\mathrm{rd}}$ mode along $\hat{y}$-axis for **Form I** of the exchange field with respect to other two can be observed. In the inset of Fig. 8(c) one can see also a discontinuity of the $\partial\mathbf{m}/\partial y$. The biggest one is observed for SWs calculated with **Form I** of the exchange field.

A thin film of a 2D MC composed of ferromagnetic circular dots in the square lattice and immersed in other ferromagnetic material is considered for the case of a 2D planar structure (see Fig. 9). The eigenvalue problem for such system is obtained in subsection 2.2 (see equation (56)) with the matrix $\hat{M}_\Lambda$ and its elements defined in (57)-(60). In the case of the studied MC the integration in (34) can be performed analytically and will lead to the following common formula:

$$X(\mathbf{G}_\parallel) = \begin{cases} \dfrac{\pi R^2}{a^2}(X_\mathrm{A} - X_\mathrm{B}) + X_\mathrm{B}, & \text{for } \mathbf{G}_\parallel = 0 \\ 2\dfrac{\pi R}{|\mathbf{G}_\parallel| a^2} J_1(|\mathbf{G}_\parallel| R)(X_\mathrm{A} - X_\mathrm{B}), & \text{for } \mathbf{G}_\parallel \neq 0 \end{cases} \tag{65}$$

where $\mathbf{G}_\parallel = (2\pi n_y/a,\ 2\pi n_z/a)$ (n_y and n_z are integers), X_A and X_B are the material parameters, i.e, M_S or $l^2_{\mathrm{ex},\Lambda}$ of the dots and matrix, respectively.

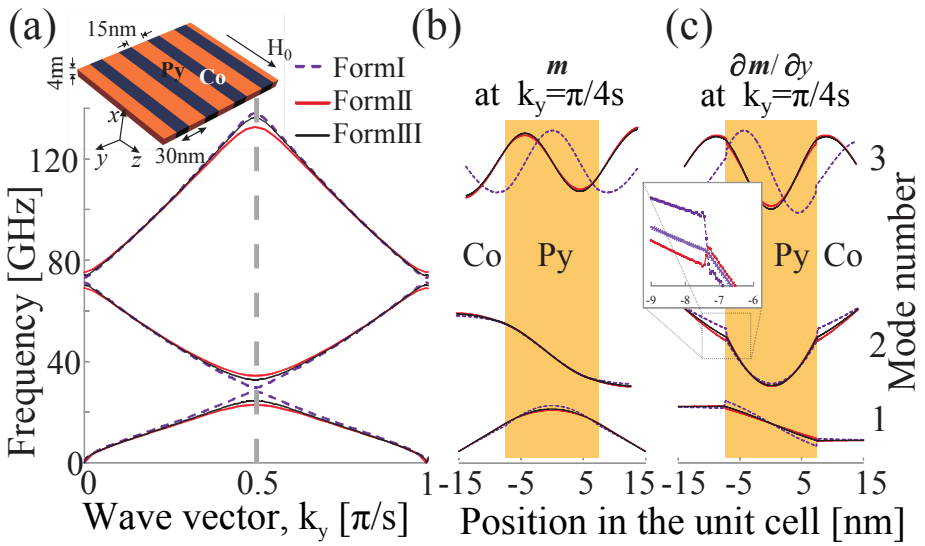

Figure 8. Magnonic band structure and profiles of SWs calculated for three different definitions of the exchange field for the considered 1D MC with the lattice constant of 30 nm and thickness 4 nm (schematically shown in the inset) for the case of dominating exchange interaction. (a) Magnonic band structure with the BZ border marked by dashed gray line. In (b) the amplitude of the dynamical component of the magnetization vector, m_x at the border of the 1st BZ is shown. Its first derivative with respect to the y is shown in (c).

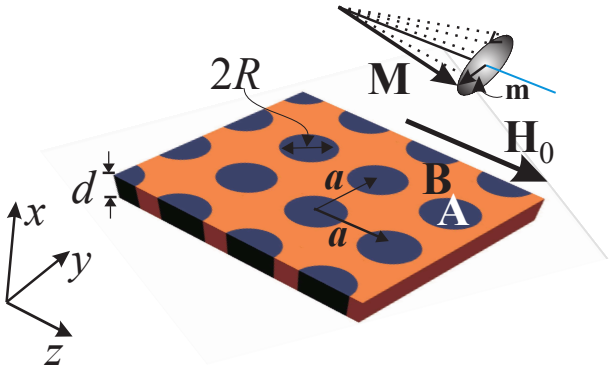

Figure 9. Schematics of the studied 2D MC. The structure is formed by cylindrical dots A arranged in a square lattice immersed into a ferromagnetic matrix B. The external magnetic field $\mathbf{H}_0$ is applied in the direction of the $\hat{z}$-axis. Spin-waves are assumed to form standing waves in the infinite (y, z) plane. The thickness of MC, d, is much smaller than the lattice constant a and the diameter of dots, $2R$.

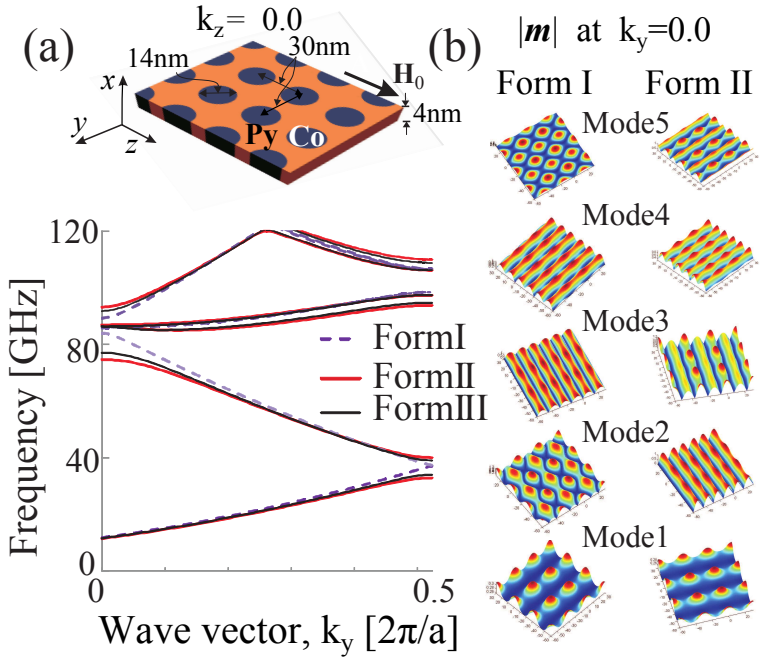

Figure 10. (a) Magnonic band structure calculated for three different definitions of the exchange field. The MC is composed of Co dots in square lattice and immersed in a Py matrix. The film has thickness of $d = 4$ nm, the lattice constant is $a = 30$ nm and diameter of dots is $2R = 14$ nm. (b) Modulus of the dynamical component of the magnetization vector calculated for the wave vector from the center of the BZ. The profiles shown are calculated for **Form II** and **Form I** of the exchange field.

First, the SW spectrum for Co dots in Py matrix in the exchange interaction dominating regime is calculated. This is obtained by assuming small lattice constant $a = 30$ nm and thickness $d = 4$ nm. The dot diameter of 14 nm is chosen. The magnonic band structure along $\hat{y}$-axis (i.e., perpendicular to the direction of the bias magnetic field) and profiles of SWs are shown in Fig. 10(a) and (b), respectively. The bias magnetic field is directed along the $\hat{z}$-axis and it is strong enough to saturate the sample, $\mu_0 H_0 = 0.2$ T. Satisfactory convergence of numerical solutions of (56) for all considered here 2D MCs proves to be assured by the use of $N = 625$ reciprocal lattice vectors.

Similar dependences as for the case of 1D MC in Fig. 8 are observed. For the **Forms II** and **III** of the exchange field magnonic gaps (at least partial) exist, while for the **Form I** the bands overlap. Differences in the SW profiles, especially for modes with higher frequencies are also found.

So far the PWM calculations have been performed for various definitions of the exchange field for MCs consisting of only Co and Py. In Fig. 11(a) and (b) the magnonic band structures of a 1D and 2D MCs, respectively, formed by Fe and YIG are shown. Fe and YIG are chosen because those materials have substantially different magnetization and exchange constants, which are: $M_{\mathrm{S,Fe}} = 1.752 \cdot 10^6$ A/m, $A_{\mathrm{Fe}} = 2.1 \cdot 10^{-11}$ J/m, $M_{\mathrm{S,YIG}} = 0.194 \cdot 10^6$ A/m, $A_{\mathrm{YIG}} = 0.4 \cdot 10^{-11}$ J/m. The geometrical parameters of the

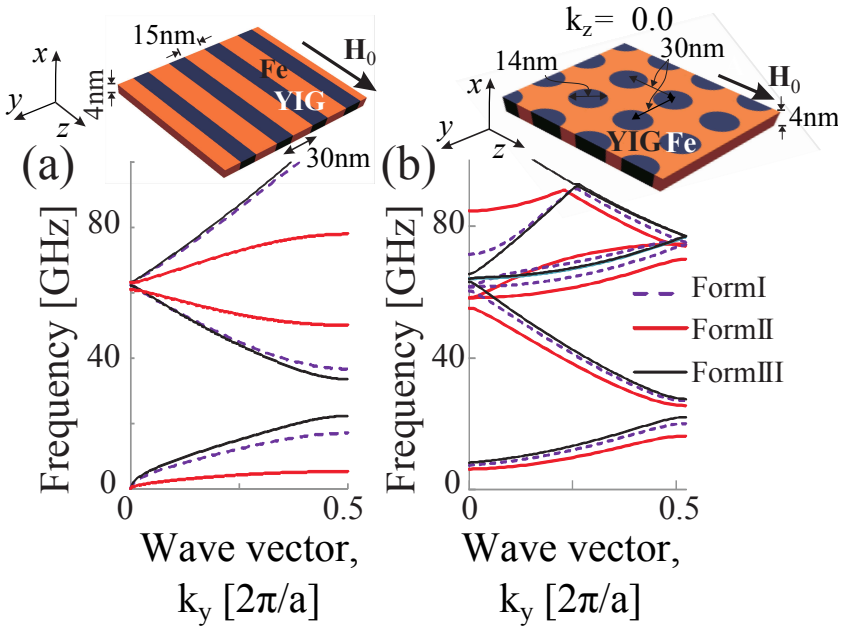

Figure 11. Magnonic band structure calculated for different forms of the exchange field. MCs composed of Fe and YIG are studied for the cases of (a) 1D and (b) 2D structures. The lattice constant is $a = 30$ nm and the film thickness is $d = 4$ nm for both cases. The external magnetic field is applied along $\hat{z}$-axis and has the value $\mu_0 H_0 = 0.001$ T for the case of the 1D MC and 0.1 T for the 2D MC.

MCs are the same as in previous figures: lattice constant is $a = 30$ nm and the film thickness is $d = 4$ nm for the 1D MC; $a = 30$ nm, $R = 7$ nm, and $d = 4$ nm for the 2D MC.

It is found that the magnonic gap (between 1st and 2nd band) exists in both MCs and for any form of the exchange energy. For the case of the 1D MC there is a significant difference between the magnonic bands and the gap width calculated using the **Form II** and other two forms. It is interesting to note that at Γ point there is a good agreement between various formulations of H_{ex}. In the 2D MC the magnonic band structure is more complicated, gaps are smaller than for 1D structure but present for all formulations of the exchange field.

Now let us try to answer the question for the physical reasons of different solutions found with **From I, II** and **III** of the exchange field. Significantly different results obtained from the **Form II** and **Form I** for Co/Py MC have been observed, while the solutions obtained from **Forms II** and **III** are close to each other. It is different to Fe/YIG MC where the solution for **Form III** is much closer to the solution of the **Form I**. Those effects shall be related to boundary conditions for dynamic components of the magnetization vector implemented in various formulations. The boundary conditions implemented in the differential equation, in our case LL equation, shall be obtained by integrating them over the interface [149]. Because the main interest here is the exchange boundary conditions it is enough for the purpose of this study to take into account only

terms connected with the exchange field in (31). By performing those integrations and taking a limit of zero thickness one can obtain the boundary conditions at the interface between two different materials. One of them implies the continuity of **m** for the **Forms II** and **III**, and continuity of the $\tilde{\mathbf{m}}$ for the **Form I**. Another one requires the continuity of $(A/M_0)\partial_n\tilde{\mathbf{m}}$, $(A/M_0^2)\partial_n\mathbf{m}$ and $\partial_n\mathbf{m}$ for the exchange field in the **Forms I**, **II** and **III** respectively. ∂_n means the derivative along the direction normal to the interface. Those boundary conditions agree with the profiles and its first derivatives found for the 1D MC and shown in Fig. 8(b) and (c), respectively (see also the inset in Fig. 8(c) for the 2$^{\text{nd}}$ mode). The continuity of the first derivative at the interface is observed only for the **Form III**, as expected. However, to validate which form of the exchange field is proper to describe properly the physical systems is out of scope of this work [78, 79, 149–155] Further investigation of the boundary conditions at the interface between two ferromagnetic materials and a definition of the $\mathbf{H}_{\text{ex}}$ is required.

At this very point it is worthy of notice that historically, the presented in this thesis derivation and a comprehensive study of the exchange component of the effective field $\mathbf{H}_{\text{eff}}(\mathbf{r}, t)$ in the LL equation (29) were performed after the results of the following subsections based on the second form of the exchange field had been obtained. The main purpose of such research was to obtain the exchange field from micromagnetic models and find its relation with the boundary conditions and influence on the magnonic band structure. It is shown that in the regime where the magnetostatic interaction predominates, i.e., for large lattice constants, the SW spectrum of planar MCs is independent on the used formulation of the exchange field. Basically, all the structures considered below, especially ones that have been also studied experimentally meet this requirement. Therefore, the results of the following subsections are valid and should not be revised.

In summary, two forms of the exchange field in a nonuniform magnetic material have been used in the numerical calculations based on the PWM for studying the influence of these different formulations on the magnonic band structure of 1D and 2D planar MCs. It is found that for large lattice constants (roughly speaking, larger than 150 nm) the SW spectrum is independent on the formulation used. It is because the magnetostatic interaction dominates over the exchange one. The situation changes for small lattice constants where in dependence on the form of the exchange field the magnonic gap can be present or absent in magnonic band structure. By numerical calculations it has been shown that various formulations of the exchange field have strong relation to the boundary conditions at the interfaces between two ferromagnetic materials. Further investigation is necessary to elucidate the proper form of the exchange field which fulfill the physical

boundary conditions imposed on dynamic components of the magnetization vector in MCs.

3.2. Magnetostatic SWs in planar 1D MCs

Let us continue studying the 1D MC shown in Fig. 5. Similar structure was fabricated and investigated by Z. K. Wang et al. [42, 43]. The comparison of the results obtained from the PWM calculations and experimental data taken from [42] is shown in Fig. 12. Second form of the exchange field (27), i.e., $\Lambda = \mathrm{II}$, is used in the calculations. Satisfactory convergence of the numerical solution of (56) for the considered MC has been already found for $N = 43$ reciprocal lattice vectors (see Fig. 7).

The evident feature of the spectrum is the presence of the two energy band gaps. It is found that applying an external magnetic field the frequencies of the entire band structure shift up and both band gaps become narrower. As one can see, a good agreement is achieved for all frequencies except the highest ones and those that are close to the center of the BZ. The discrepancy for the third band increases when a nonzero external magnetic field is applied (Fig. 12(a)). An explanation could be the fact that the gyromagnetic ratio is assumed to be uniform in the PWM calculations and moreover the magnetostatic field is taken in the middle of the plane of the MC (in $x = 0$). Including into the calculations inhomogeneity of the gyromagnetic ratio allows the authors of [42] to obtain a better agreement for all energy bands of the studied structure (Fig. 3 in [42]).

Higher frequencies of the first mode observed in the experiment as compared to those obtained from the PWM calculations can have two sources: it can be connected with limitations of the experimental setup or/and with real structure of the MC different from that used in the calculations. In the Brillouin light scattering (BLS) spectroscopy light is collected under limited range of angles, i.e., the signal is coming to Fabry-Perot interferometer from some range of the transversal components of the light's wave vectors. Assuming that the experimental setup has the resolution taken from [156]: $\Delta k = 0.45{\cdot}10^{-3}$ nm^{-1}, from the PWM calculations one can obtain frequency around 2 GHz for $k = 0$ and $H_0 = 0$. In the case of the uniform thin film very small magnetic field will shift up frequency of the Damon-Eshbach mode to a higher frequency, e.g., putting $\mu_0 H_0 = 0.005$ T shifts up the frequency to 2.0 GHz for $k = 0$. This is very small value and it is reasonable, that there could be comparable anisotropy field in real Co/Py stripes, at least in Co ones. The role of the interfaces was skipped in [42]. This issue is studied in details in the next subsection 3.3. It is found that 4 nm thick air spaces result in 3 GHz frequency of the first mode in the center of the BZ with $H_0 = 0$. By increasing the empty spaces increase of the frequencies of the modes is observed.

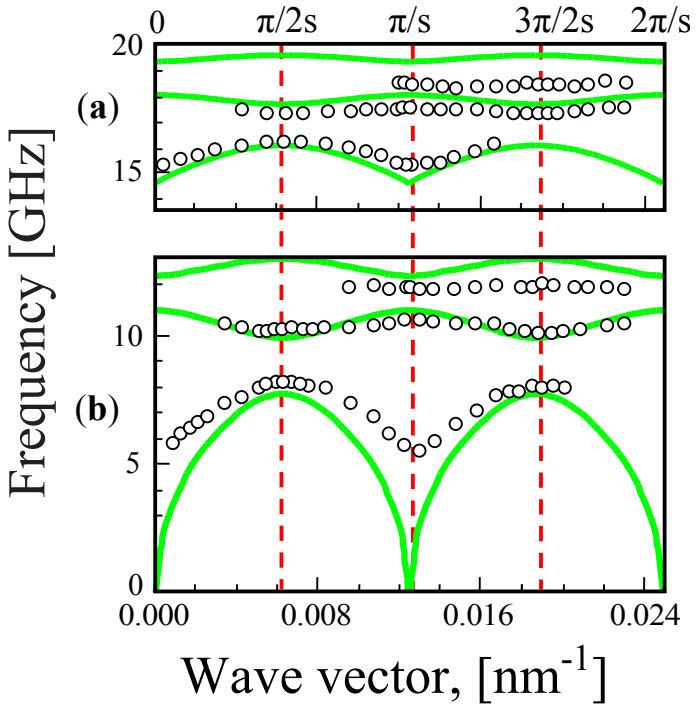

Figure 12. Spin wave spectra of the studied MC. (a) The SW frequency in dependence on the wave vector of the considered structure for $\mu_0 H_0 = 0.2$ T. The green lines represent results of the PWM calculations, whilst the open circles are the experimental data taken from [42]. (b) Magnonic band structure of the studied system in the same configuration as in (a) but for $\mu_0 H_0 = 0$ T. Experimental points are taken also from [42].

In order to understand the nature of the observed SW spectra the dependences of the SW frequency on the static magnetizations and the exchange constants in the nanostripes are calculated. The results are presented in Fig. 13. As one can see there is almost no effect of the exchange constant of Py for the first three bands with lower frequency and there is minor effect of the static magnetization of Co on the magnonic band structure of the studied MC. (The dependence of the spectrum on the exchange constant in Co is found to be the same as that for Py). At the same time, the spectrum of our system is sensitive to the magnitude of the static magnetization of Py. The independence of the magnonic band structure on the exchange constants points out that the first three bands observed in the experiment have magnetostatic nature while in the bands with higher frequency exchange interaction starts to play important role.

In order to have a deeper insight into the behaviour of the SWs in the considered MC the amplitude profiles of the waves with arbitrary chosen frequencies from the 1st, 2nd, and 3rd bands are calculated and shon in Fig. 14. According to these profiles the amplitude of the SWs from all three bands are concentrated in the Py nanostripes. This result explains insensitivity of the studied material with respect to the static magnetization of the Co nanostripes.

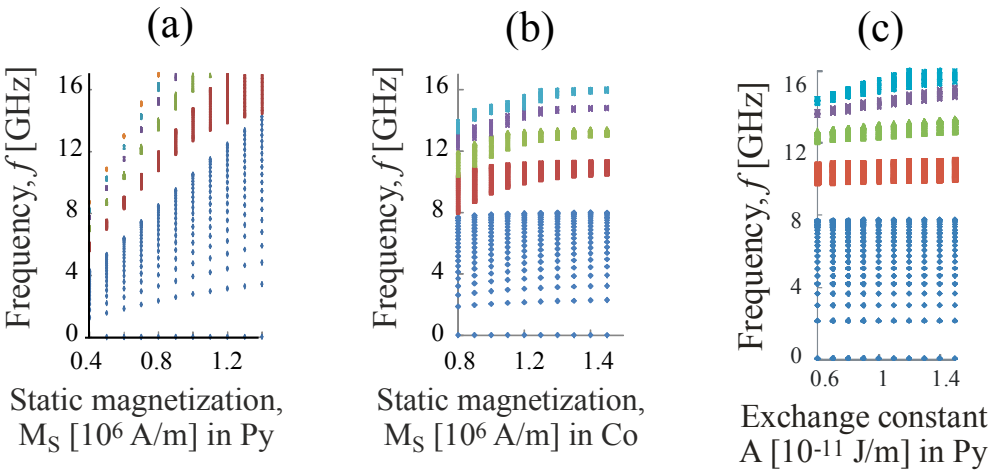

Figure 13. Confirmation of magnetostatic nature of the observed SWs. In this figure, the SW frequencies versus static magnetization (a and b) and exchange constant (c) of the Py and Co nanostripes of the studied MC are shown. As one can see, the low frequency spectrum of the considered structure almost doesn't depend on the exchange constant in Py and has a week influence from the static magnetization of Co.

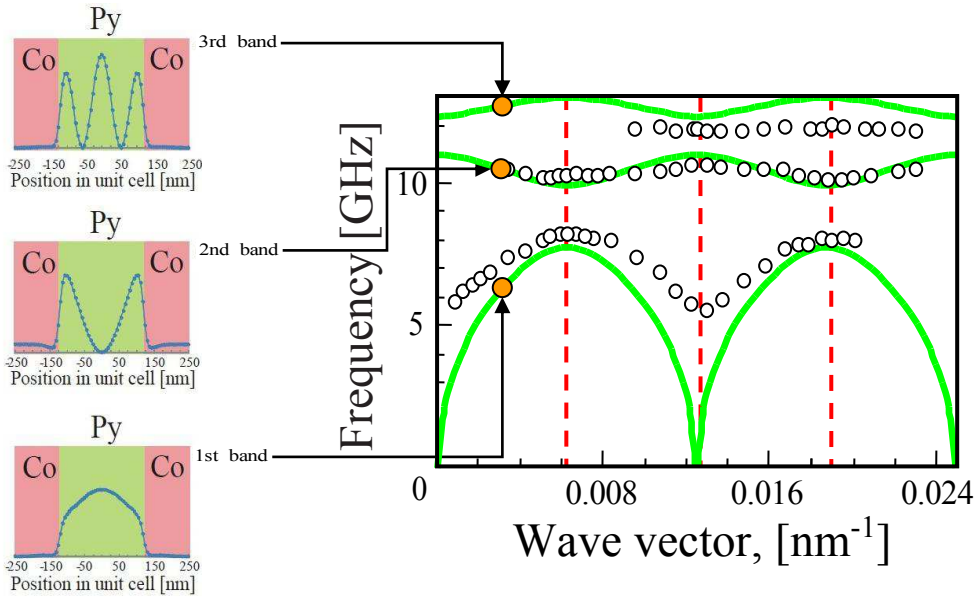

Figure 14. Profiles of the SWs with frequencies taken from the 1st, 2nd, and 3rd bands of the magnonic band structure are shown. As one can see, the SWs are localized in the Py nanostripes.

In summary, the SW spectrum of a nanoscale periodic magnetic structure with a finite thickness is calculated. The PWM is employed for this purpose. The dynamic demagnetizing field is obtained in the form suitable for the PWM. A good agreement with the published BLS measurements is obtained. Localization of the SWs in the Py nanostripes is shown and the magnetostatic nature of the observed spin waves is justified.

3.3. Introduction of a nonmagnetic dielectric spacer

The fabrication process of artificial periodic structures with characteristic dimensions in nanoscale is very hard to control. Especially it concerns the quality of the interfaces between adjacent layers which make up a MC. Diffusion normally occurs between homogeneous materials and therefore it can create a "transition" layer with properties different from the original constituents. It is well known that the speed of diffusion is proportional to the concentration gradient at the interface and hence is fastest in structures prepared with sharp interfaces. Most of the theoretical papers devoted to investigation of the SW dynamics in MCs consider structures with infinitely thin interfaces [79, 90, 92, 98]. However, in some cases, this assumption is a severe idealization and another model should be used instead. For example, in Ref. [75] the coordinate dependence of magnetic parameters of a "transition" layer was approximated by the Jacobian elliptic sine function. A strong dependence of the magnonic spectrum and coefficients of reflection and transmission of SWs upon the thickness of interfaces was demonstrated. The spectrum of exchange SWs in a MC with diffuse interfaces was derived for a model with a cosine-like [157] and linear [158] profiles of the uniaxial anisotropy value at the interfaces. Degradation of the performance of magnonic devices employing MCs as a filtering element with the increase of the thickness of interfaces, e.g. due to the process of diffusion between constituent layers of MCs, was demonstrated.

In the case of the structure considered in the previous subsection the disagreement between numerical results of the PWM and the experimental data taken from [42], among others, could be induced by the imperfections of the interfaces between the nanostripes. The white vertical "stripes" in the scanning electron microscope image of the MC (see Fig. 1(a) in Ref. [42]) may indicate the presence of another material or air between the Co and Py slabs. To model such situation a MC represented by a 1D periodic array of Py and Co nanostripes of equal width that are separated by the air or any other nonmagnetic dielectric (NM) material is considered (see Fig. 15).

In the SW spectra calculations second form (27) of the exchange field is used, i.e., $\Lambda = \mathrm{II}$. Material parameters of Co and Py are assumed to be equal to those in subsection 3.1. External magnetic field $\mathbf{H}_0$ is applied along the stripes and equal to $\mu_0 H_0 = 0.1$ T.

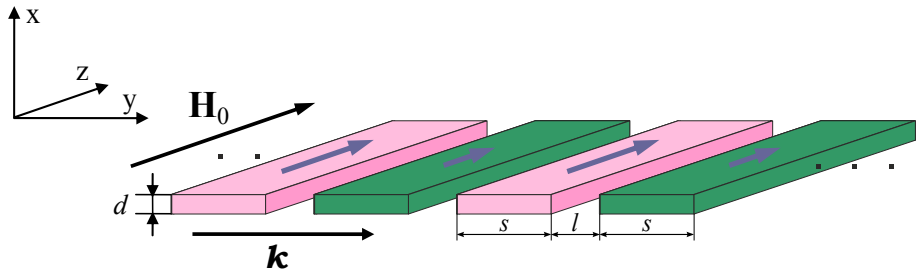

Figure 15. Geometry of a MC in the form of a 1D periodic array of two ferromagnetic nanostripes of thickness d and width s that are separated by a nonmagnetic layer of width l. A magnetic field $\mathbf{H}_0$ is applied along the stripes length, $\mathbf{k}$ is the wave vector of the SWs.

A remark must be made on the application of the PWM to the calculations of the magnonic band structure of MCs with nonmagnetic inclusions. These inclusions cause the divergence of the solution of the eigenvalue problem (56). In order to overcome this problem values of the "static magnetization" and "exchange constant" of air are chosen ten times lower than the ones of Py, i.e., $M_{\mathrm{S,air}} = 0.0658 \cdot 10^6$ A/m and $A_{\mathrm{air}} = 0.11 \cdot 10^{-11}$ J/m, respectively. (A detailed study and discussion of the considered assumption will be given in subsection 3.7).

The band structure of the MC depicted in Fig. 15 is calculated by solving numerically the eigenvalue problem (56) with the Fourier coefficients of the material parameters calculated according to the following formula:

$$X(G_y) = \begin{cases} \dfrac{s}{a}(X_{\mathrm{A}} - X_{\mathrm{B}}) + \dfrac{2l}{a}(X_{\mathrm{NM}} - X_{\mathrm{B}}) + X_{\mathrm{B}}, & \text{for } G_y = 0 \\ \dfrac{2}{G_y a}\left[(X_{\mathrm{A}} - X_{\mathrm{B}}) \sin\left(\dfrac{G_y s}{2}\right)\right. & \\ \left. +2\,(X_{\mathrm{NM}} - X_{\mathrm{B}}) \sin(G_y l) \cos(G_y(s+l))\right], & \text{for } G_y \neq 0 \end{cases} \tag{66}$$

where $a = 2(s + l)$ is the period of the lattice, X_{A}, X_{B}, and X_{NM} are the material parameters, i.e, M_{S} or $l^2_{\mathrm{ex},\Lambda}$ in the stripes A, B or in the NM spacer, respectively.

The dependence of the SW spectrum of the considered structure on the width of the NM gap is shown in Fig. 16(a) for the case of the $s = 250$ nm width of the nanostripes. As one can see there is an evident and significant shift of the lowest band to higher frequencies. A NM spacer of 2 nm width results in about 4 GHz frequency of the first mode in the centre of the BZ. Such minute separation (more than 100 times smaller than the width of the stripes) may occur in the sample during its fabrication. Hence this shift in frequency may explain the disagreement between the results of PWM calculations (see Fig. 12) and the experimental data taken from [42]. Actually, a 1-nm-wide gap was introduced by the group of Adeyeye in the micromagnetic simulations in their recent paper [159]. Hence,

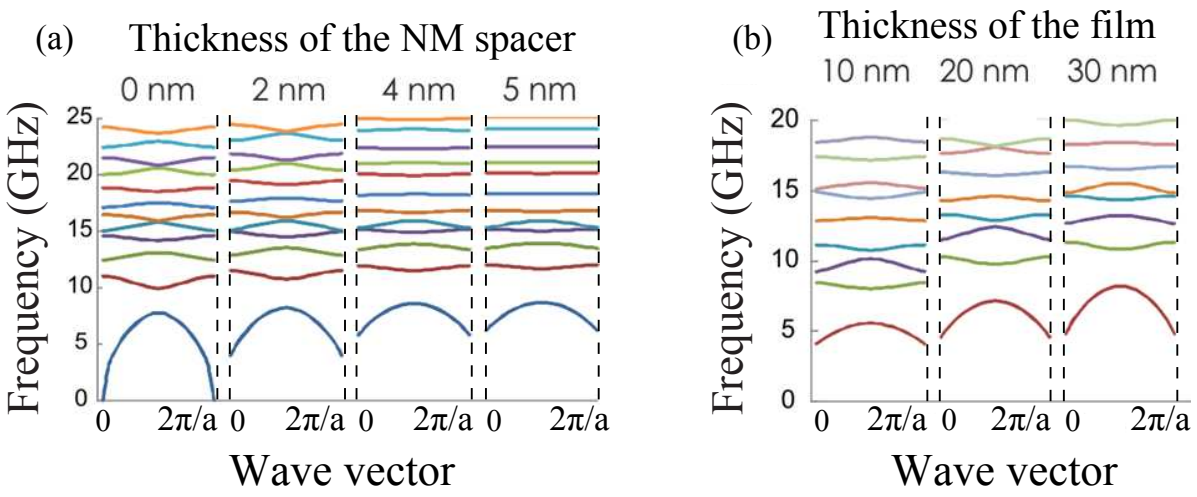

Figure 16. SW spectrum of a MC in the form of a 1D periodic array of Py and Co nanostripes of width $s = 250$ nm that are separated by a NM layer in dependence of (a) its width l and (b) thickness of the film d. The value of separation in the latter case is $l = 3$ nm. External magnetic field is $\mu_0 H_0 = 0.1$ T. The wave vector changes in the range from 0 to $2\pi/a$. A significant shift of the lowest band to higher frequencies is observed in graph (a). At the same time the higher bands of the SW spectrum become flatter for larger values of the width of the NM spacer. Increase of the thickness of the studied MC results in strong bending of the first mode of the magnonic spectrum while the higher modes are mainly shifted up in frequency without changing their curvature (see graph (b)).

they admit that misalignment during the two-step lithographic process may result in such a gap at the interface of two alternate magnetic media.

Increase of the frequencies of the modes is observed in Fig. 16(a) with further increase of the width of the NM gap. At the same time the higher bands of the magnonic spectrum become flatter for larger values of the distance between the nanostripes. The SW spectrum of the considered MC versus thickness of the film is shown in Fig. 16(b). The value of the width of the NM layer is $l = 3$ nm. Increase of the film thickness results in strong bending of the first mode of the band structure while the higher modes are mainly shifted up in frequency without changing their curvature.

These results presented in Fig. 16 can be explained in terms of the strength of interaction between the nanostripes. It is well known that the exchange interaction is present only in magnetic media. Therefore the only interaction that creates the SW spectrum in the considered case of the array of nanostripes separated by a NM material is the magnetostatic one. Increase of the value of separation of the magnetic slabs as well as decrease of the thickness of the film will decrease the magnetostatic interaction between the nanostripes. Hence the modes become less dispersive and flatter.

The results of the PWM calculations for the studied MC in the exchange dominating regime is represented in Fig. 17. As opposed to the previous configuration of the MC

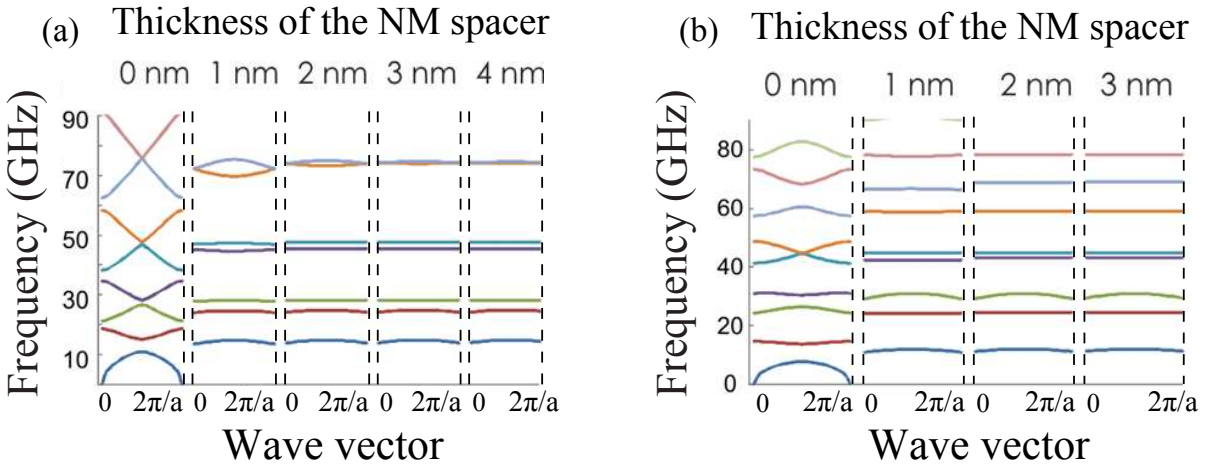

Figure 17. SW spectrum of the considered MC consisted of (a) Co/Py and (b) Fe/Py slabs in the exchange dominating regime versus width of the NM spacer. Thickness of the film is $d = 10$ nm while the width of the nanostripes is $s = 51$ nm. External magnetic field is $\mu_0 H_0 = 0.1$ T. The wave vector changes in the range from 0 to $2\pi/a$. An evident feature of the both graphs is almost flat magnonic bands when the width of the NM spacer differs from 0. The transition happens when the space filled by a NM material between the magnetic nanostripes appears, then the SW spectrum remains almost unaffected. Shift of the modes to higher frequencies with increase of the width of the NM layer is not observed.

the width of the magnetic nanostripes has been reduced to $s = 51$ nm. Film thickness of $d = 10$ nm is kept the same in both configurations. SW spectrum of the considered MC consisted of Co and Py slabs in dependence on the width of the NM gap is shown in Fig. 17(a). Similar results but for the case when Co stripes are replaced by the ones made of Fe are depicted in Fig. 17(b). An evident feature of the both figures is almost flat bands when the width of the gap between the magnetic slabs differs from 0. The transition happens when the space filled by a NM material between the magnetic nanostripes appears, then the SW spectrum remains almost unaffected. Similar shift of the modes to higher frequencies with increase of the width of the NM spacer shown in Fig. 16 is not observed here.

In summary, the SW spectrum of the planar 1D MC comprised of a periodic array of two ferromagnetic thin slabs separated by a NM material has been calculated. Flattening the SW spectrum of the considered MC and shifting up the first band to higher frequencies with the increase of the size of a NM spacer have been demonstrated. An explanation of the disagreement between the results of the PWM calculations and the experimental data has been proposed.

3.4. Metallic overlayers - a promising tool for controlling the spectrum of magnetostatic SWs in planar MCs

Magnetostatic waves are known as "slow branches" (with small phase and group velocities) in the spectrum of electromagnetic waves in a ferromagnetic body. It is well known that metals play the role of screens for electromagnetic waves, i.e., the amplitude of the electromagnetic field decays exponentially over a very short distance defined by the skin depth. Therefore magnetostatic SWs should be sensitive to different types of substrates or overlayers, e.g., metallic, dielectric etc. that has been demonstrated in plenty of publications [3, 80, 160–164]. For example, magnetostatic surface waves propagating in a YIG film of finite dimensions with a metallic nonmagnetic screen placed at a distance from the surface of the film were studied in detail in [162]. The dependences of the dispersion relation and the bandwidth of surface waves on the propagation direction of the wave, thickness of the dielectric interlayer and width of the magnetic film were obtained. It was shown that for sufficiently high values of YIG-to-dielectric-thickness ratio the dispersion of SWs that propagate along the surface next to the conductor exhibits a region with zero group velocity. Propagation of SWs in a thin ferromagnetic film with a periodic array of metallic stripes on its surface was studied in [80, 164]. The dependence of the bandwidth of the SWs on filling fraction of the metallic grating was found in [80]. It was shown that the dispersion characteristics of planar periodic structures based on ferromagnetic films depend, not only on the geometry of the waveguiding system, but also on the surface anisotropy of the initial film.

A case when a tangentially magnetized uniform ferromagnetic film adjoins metal at one side and air at the other side was studied in [160]. It was shown that the presence of a conductor at one face of the film leads to the following "anisotropic" dispersion relation of the surface magnetostatic waves:

$$f = \frac{\gamma\mu_0 M_S}{2\pi}\left[\frac{\rho}{4}\left(1-e^{-2kd}\right)+\sqrt{\frac{1}{16}\left(1-e^{-2kd}\right)^2-0.5\left(1+\frac{H_0}{M_S}\right)\left[e^{-2kd}-1-2\frac{H_0}{M_S}\right]}\right],$$

where $\rho = \pm 1$ corresponds to the propagation in the positive/negative direction of the $\hat{y}$-axis, M_S is the saturation magnetization of the film, and H_0 is the applied external magnetic field. Comparison of the magnonic band structure of metallized and nonmetallized uniform films made of $d = 30$-nm-thick Py with $M_S = 0.8 \cdot 10^6$ A/m is

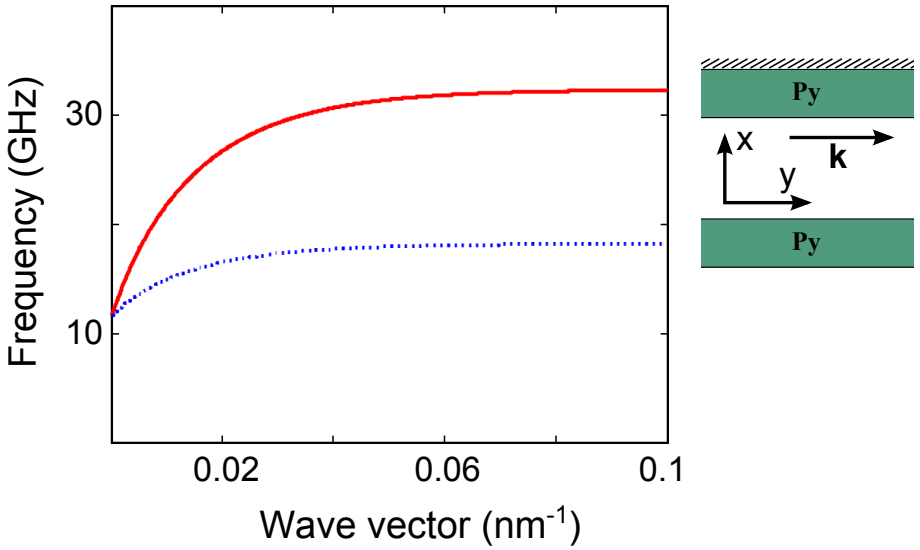

Figure 18. Dispersion relations of surface magnetostatic waves in a uniform Py film surrounded by dielectrics (blue dotted line) and covered by metal at one side (red solid line). Thickness of the film and the saturation magnetization are $d = 30$ nm and $M_S = 0.8 \cdot 10^6$ A/m, respectively. External magnetic field is $\mu_0 H_0 = 0.15$ T in both cases.

shown in Fig. 18. The bias magnetic field is $\mu_0 H_0 = 0.15$ T. The dispersion of SWs in the nonmetallized film is calculated according to the well-known Damon-Eshbach formula:

$$f = \frac{\gamma \mu_0 M_S}{2\pi} \sqrt{\left(\frac{1}{2} + \frac{H_0}{M_S}\right)^2 - \frac{1}{4} e^{-2kd}}.$$

As one can see a metal layer placed at one side of the magnetic film causes the significant increase of the group velocity of the magnetostatic SWs with small wave vectors (in the vicinity of $k = 0$). Therefore one can expect to observe similar effect when the uniform film is replaced by a MC. Below the PWM for calculations of the SW spectra in planar 1D and 2D MCs having various lattice constants and covered at one side by metallic screen is developed.

Let us cover a planar MC at one side by a perfect conductor (see Fig. 19). The structure consisted of alternating Co and Py nanostripes of equal width s and finite thickness d that has been investigated in details in the previous subsections is considered as the case of a 1D MC (see Fig. 19(a)). A 2D structure is studied on the example of a planar MC comprised of a periodic array of squared Co dots of width q arranged in the square lattice with period a and immersed in Py thin film of thickness d (see Fig. 19(b)). The origin of coordinates is placed in the center of the MC. External magnetic field is applied along the $\hat{z}$-axis and equal to $\mu_0 H_0 = 0.1$ T in both cases.

In the case of the ideal conductor with conductivity $\sigma \to \infty$ the skin depth vanishes $\delta \to 0$. It means that electromagnetic waves simply can not penetrate into the ideal

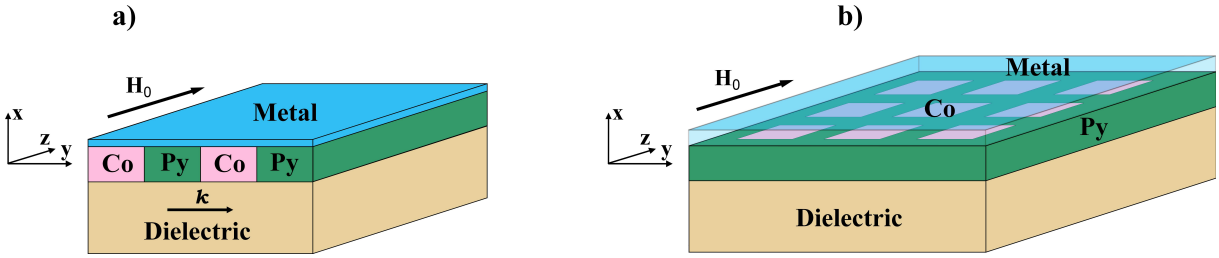

Figure 19. Schematics plots of the considered structures consisted of planar MCs covered by metal at one side and dielectric at another. a) 1D MC studied in details in subsection 3.2. b) 2D planar MC comprised of a periodic array of squared Co dots immersed in Py thin film. The external magnetic field is directed along the $\hat{z}$-axis.

conductor, i.e., $\mathbf{B} = 0$ everywhere inside of the latter including its surface. At the same time metallic material is transparent for a static magnetic field. Therefore replacing dielectric with metal the configuration of the dynamic magnetostatic field within the studied structure gets affected. Mathematically the influence of metallic screen on the internal magnetic field of the studied structures is expressed in the boundary conditions for the magnetostatic potential ψ as follows:

$$\left[-\frac{\partial\psi_i(\mathbf{r})}{\partial x} + m_x(\mathbf{r})\right]\Bigg|_{x=\frac{d}{2}} = 0, \tag{67}$$

where index i designates inner region of the considered MC. Conditions at the interface between the MC and dielectric substrate, i.e, at $x = -d/2$ have the same form as in (45).

Solving equations (43) and (44) together with the boundary conditions at the interfaces with dielectric (45) and metal (67), one can obtain the magnetic field inside the studied 2D MC in the form of a Fourier series as a function of the magnetization vector:

$$\begin{aligned}
H_z(\mathbf{r}_\parallel, x) &= -\sum_{\mathbf{G}_\parallel} \frac{G_z^2}{\mathbf{G}_\parallel^2} M_{\mathrm{S}}(\mathbf{G}_\parallel)\left(1 - \cosh\left(|\mathbf{G}_\parallel|x|\right)\mathrm{e}^{-|\mathbf{G}_\parallel|d/2}\right)\mathrm{e}^{i\mathbf{G}_\parallel\cdot\mathbf{r}_\parallel},\\
h_x(\mathbf{r}_\parallel, x) &= -\sum_{\mathbf{G}_\parallel} m_{x,\mathbf{k}_\parallel}(\mathbf{G}_\parallel)\mathrm{e}^{|\mathbf{k}_\parallel+\mathbf{G}_\parallel|(x-d/2)}\mathrm{e}^{i(\mathbf{k}_\parallel+\mathbf{G}_\parallel)\cdot\mathbf{r}_\parallel},\\
h_y(\mathbf{r}_\parallel, x) &= \sum_{\mathbf{G}_\parallel} \frac{(k_y+G_y)^2}{2|\mathbf{k}_\parallel+\mathbf{G}_\parallel|^2} m_{y,\mathbf{k}_\parallel}(\mathbf{G}_\parallel)\left(\mathrm{e}^{|\mathbf{k}_\parallel+\mathbf{G}_\parallel|(x-3d/2)} + \mathrm{e}^{-|\mathbf{k}_\parallel+\mathbf{G}_\parallel|(x+d/2)} - 2\right)\mathrm{e}^{i(\mathbf{k}_\parallel+\mathbf{G}_\parallel)\cdot\mathbf{r}_\parallel}.
\end{aligned} \tag{68}$$

Similar formulas for the considered 1D structure can be easily obtained from this more general case by taking $G_z = k_z = 0$.

As one can see that all components of the demagnetizing field are x-dependent, i.e., vary with position across the thickness of the MC. However, when the film is thin enough (that is the case of the studied MC) the nonuniformity of the demagnetizing field across its

thickness can be neglected. For the following calculations the value of the magnetostatic field taken at the border MC/metallic overlayer, i.e., at the point $x = d/2$, is used as the value across the thickness.

Substitution of (33), (35) and (68) into (31) leads to the eigenvalue problem (56) where elements of the matrix $\hat{M}$ are defined as follows:

$$\hat{M}_{ij}^{xx} = \hat{M}_{ij}^{yy} = 0, \tag{69a}$$

$$\hat{M}_{ij}^{xy} = \delta_{ij} + M_{i,j}^{\mathrm{ex},\Lambda} - \frac{(G_{z,i} - G_{z,j})^2}{H_0 |\mathbf{G}_{\parallel,i} - \mathbf{G}_{\parallel,j}|^2} M_{\mathrm{S}}(\mathbf{G}_{\parallel,i} - \mathbf{G}_{\parallel,j}) \left(1 - C(\mathbf{G}_{\parallel,i} - \mathbf{G}_{\parallel,j}, x)\right) \tag{69b}$$

$$- \frac{(k_y + G_{y,j})^2}{2H_0 |\mathbf{k}_\parallel + \mathbf{G}_{\parallel,j}|^2} M_{\mathrm{S}}(\mathbf{G}_{\parallel,i} - \mathbf{G}_{\parallel,j}) \left(\mathrm{e}^{|\mathbf{k}_\parallel + \mathbf{G}_{\parallel,j}|(x-3d/2)} + \mathrm{e}^{-|\mathbf{k}_\parallel + \mathbf{G}_{\parallel,j}|(x+d/2)} - 2\right),$$

$$\hat{M}_{ij}^{yx} = -\delta_{ij} - M_{i,j}^{\mathrm{ex},\Lambda} + \frac{(G_{z,i} - G_{z,j})^2}{H_0 |\mathbf{G}_{\parallel,i} - \mathbf{G}_{\parallel,j}|^2} M_{\mathrm{S}}(\mathbf{G}_{\parallel,i} - \mathbf{G}_{\parallel,j}) \left(1 - C(\mathbf{G}_{\parallel,i} - \mathbf{G}_{\parallel,j}, x)\right)$$

$$- \frac{1}{H_0} M_{\mathrm{S}}(\mathbf{G}_{\parallel,i} - \mathbf{G}_{\parallel,j}) \mathrm{e}^{|\mathbf{k}_\parallel + \mathbf{G}_{\parallel,j}|(x-d/2)}, \tag{69c}$$

where the function $C(\mathbf{k}_\parallel, x)$ and the matrix elements $M_{i,j}^{\mathrm{ex},\Lambda}$ in the above equations are defined in (59) and (60), respectively.

Fourier coefficients of the material parameters in (69) can be obtained in the following analytical form:

$$X(\mathbf{G}_\parallel) = \begin{cases} \dfrac{q^2}{a^2}(X_{\mathrm{A}} - X_{\mathrm{B}}) + X_{\mathrm{B}}, & \text{for } \mathbf{G}_\parallel = 0 \\ \dfrac{q^2}{a^2} \operatorname{sinc}(\dfrac{G_y q}{2}) \operatorname{sinc}(\dfrac{G_z q}{2})(X_{\mathrm{A}} - X_{\mathrm{B}}), & \text{for } \mathbf{G}_\parallel \neq 0 \end{cases} \tag{70}$$

where $\mathbf{G}_\parallel = (G_y, G_z) = (2\pi n_y/a,\ 2\pi n_z/a)$ (n_y and n_z are integers), X_{A} and X_{B} are the material parameters, i.e, M_{S} or $l_{\mathrm{ex},\Lambda}^2$ of the dots and matrix, respectively. Fourier coefficients of the material parameters for the studied 1D structure can be found in (64), where $s = a/2$.

In the following calculations the second form of the exchange field (27), i.e., $\Lambda = \mathrm{II}$ is used. Satisfactory convergence of the results of the obtained eigenproblems for the considered MCs proves to be attained with the use of $N = 121$ in the 2D case and $N = 43$ lattice vectors in the case of the 1D structure. Material parameters of Co and Py are assumed to have the following values: exchange constants $A_{\mathrm{Co}} = 2.8 \cdot 10^{-11}$ J/m, $A_{\mathrm{Py}} = 1.11 \cdot 10^{-11}$ J/m, and saturation magnetization $M_{\mathrm{S,Co}} = 1.39 \cdot 10^6$ A/m, $M_{\mathrm{S,Py}} = 0.8 \cdot 10^6$ A/m.

As it was mentioned above, the dynamic magnetization is assumed to be uniform across the thickness of the considered MC. It means that the frequency of the SW is limited by

the frequency of the first standing wave in the slab. To have a rough estimation of this value one can use the well-known Kittel formula for a uniform magnetic material:

$$f = \frac{1}{2\pi}\sqrt{\left(\gamma\mu_0 H_0 + \frac{2A\gamma}{M_\mathrm{S}}k^2\right)\left(\gamma\mu_0 H_0 + \gamma\mu_0 M_\mathrm{S} + \frac{2A\gamma}{M_\mathrm{S}}k^2\right)}, \tag{71}$$

where the wavevector k should be replaced with the one for the first standing wave, i.e., $k = \pi/d$. Using values of the material parameters defined above one can obtain two frequencies related to a thin film of Co or Py respectively: $\omega_{\mathrm{Co}} \approx 136$ GHz, $\omega_{\mathrm{Py}} \approx 92$ GHz. Taking the minimum value we can say that our approximation is justified for the frequencies of the spin waves smaller than 92 GHz.

Another consideration that has been made in the calculations concerns the conductivity of the metallic coat placed on top of the studied MC. As it was mentioned above a planar MC is considered to be covered on one side by a perfect conductor, i.e., the conductivity of the metal is infinite. Detailed analysis of the influence of the conductivity of a metallic overlayer on the spectrum of the magnetostatic waves in uniform ferromagnetic films was done, e.g., by R.E. De Wames and T. Wolfram in [161]. From the results of this paper one can estimate the effect of finite conductivity on the results of the PWM calculations of the SW spectrum of the considered MC.

It was shown in [161] that the mentioned approximation is valid for small values of $\delta \cdot k$ (δ is the skin depth of the metal, k is the magnitude of the wave vector) provided that $d > k \cdot \delta^2$. One can easily estimate this thickness. For example, for Copper at 10 GHz the skin depth is equal to $\delta = 0.65 \cdot 10^{-6}$ m and the wave vector has its maximum at the border of the Brillouin zone, so the thickness of the metal should be greater than $d > 0.265 \cdot 10^{-5}$ m. For large wave vectors and finite conductivity the dispersion curve should approach the Damon-Eshbach result of a ferromagnetic film surrounded by a dielectric when $k \to \infty$. This limit is not considered in this thesis.

The SW spectrum of the studied 1D MC is shown in Fig. 20 for the width of the nanostripes $s = 5$ nm, thickness of the slab $d = 0.5$ nm and the value of the external field $\mu_0 H_0 = 0.1$ T. The dashed lines represent the dispersion relation of the considered MC covered by a metallic overlayer, whilst the solid lines are the dispersion relation of the MC without metallic cover, calculated according to the equations obtained in subsection 3.1. For such very small lattice constants the more important role is played by the exchange interaction as compared to the magnetostatic one. As a consequence of it one can see almost no difference in the SW spectra of the considered MC with and without a metallic overlayer on top of it (see Fig. 20). Practically the same picture is observed in the case of the studied 2D structure (see Fig. 21). The dispersion curves of the metallized and

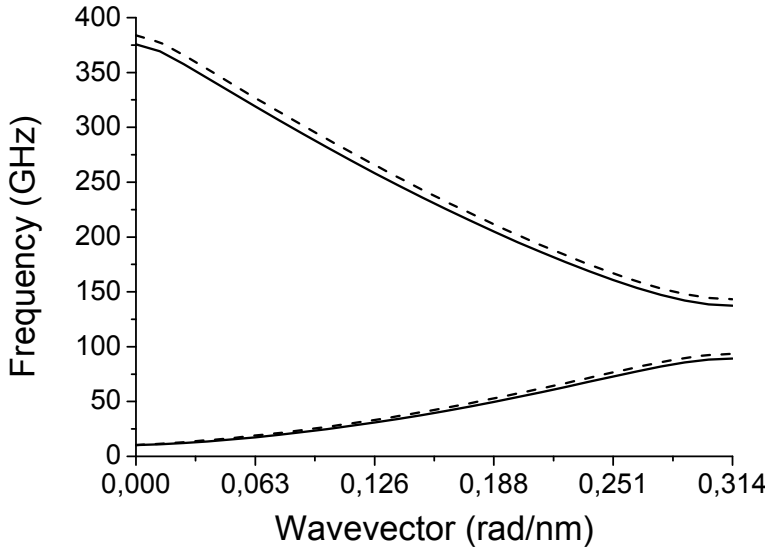

Figure 20. SW spectrum of the studied 1D MC is shown for the nanostripes of $s = 5$ nm width and of $d = 1$ nm thickness. The dashed lines represent the dispersion relation of the considered MC covered by a metallic overlayer, whilst the solid lines are the dispersion relation of the MC without metallic coating.

non-metallized 2D MC almost merged with each other. The magnonic band structure is plotted along the path in the first BZ shown in the inset in Fig. 21.

If the lattice constant of the MCs is enhanced to $a = 2s = 500$ nm magnetostatic field will become dominating for all wavevectors of the lowest bands (see Figs. 22 and 23). As one can see from Fig. 22 the behavior of the dispersion relation of the 1D system in the vicinity of $k = 0$ is linear, similar to the Damon-Eshbach one and thereby is defined by the magnetostatic interaction. By evaporating a film of metal on top of the considered 1D MC it is possible to increase significantly the slope (i.e., group velocity of the SW) of the first band and shift up the first band gap to higher frequencies. This result could be useful for applications as the increase of the group velocity can be used to shift the phase of the SWs propagating in logic devices based, e.g., on the Mach-Zehnder interferometer structure [50, 51, 55]. In the case of the 2D MC there are two regions in the band diagram (Fig. 23) with different types of propagating SWs. When the wave vector changes from Z to Γ it is the case of the backward volume wave configuration, when it changes from Γ to K it is the case of the surface Damon-Eshbach waves. The lowest bands of the former type of SWs are almost flat while the ones of the latter type are dispersive similarly to those obtained in the case of the 1D MC (Fig. 22). Recently such behaviour of the surface waves was observed experimentally in a bi-component 2D MC with magnetic inclusions having a circular shape [165]. It was shown that the low frequency mode resides along the etched regions in parallel stripes oriented perpendicular to the applied field whereas the high frequency mode exhibits the large spin precession amplitude between those parallel stripes.

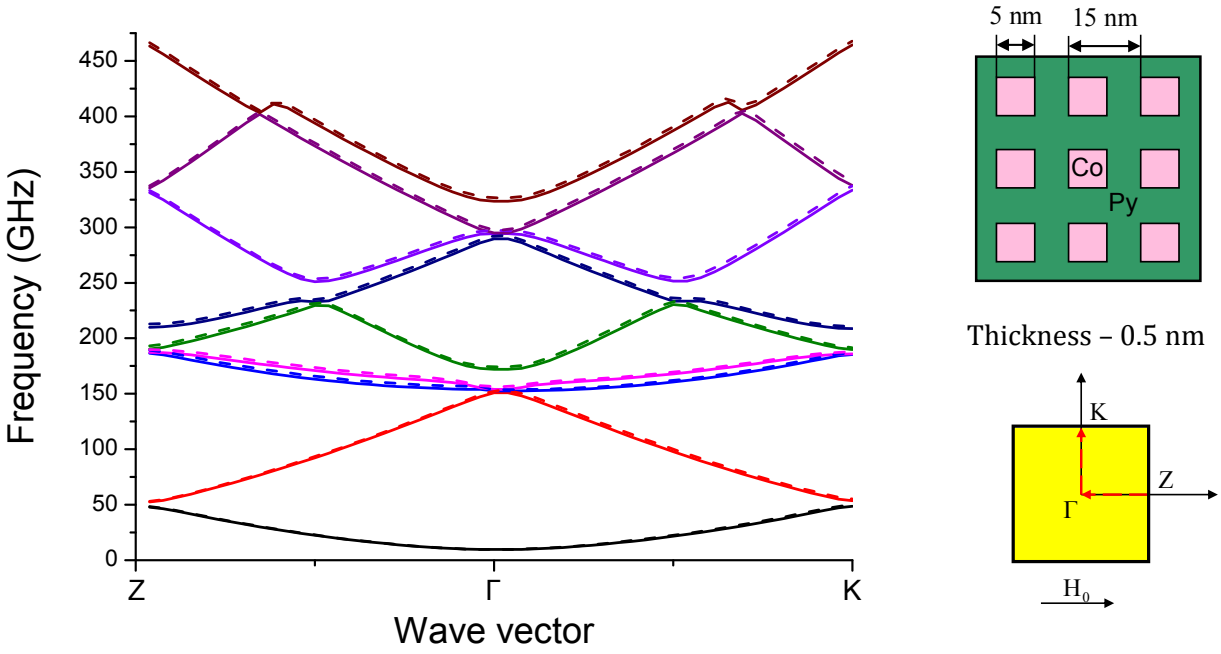

Figure 21. SW spectrum of the considered 2D MC with the dots of $q = 5$ nm width and of $d = 0.5$ nm thickness (schematically shown in the upper inset). Period of the structure is $a = 15$ nm. The dashed lines represent the dispersion relation of the studied MC covered by a metallic overlayer, whilst the solid lines are the dispersion relation of the MC without metallic coating. The 1st BZ of the considered structure is shown in the bottom inset.

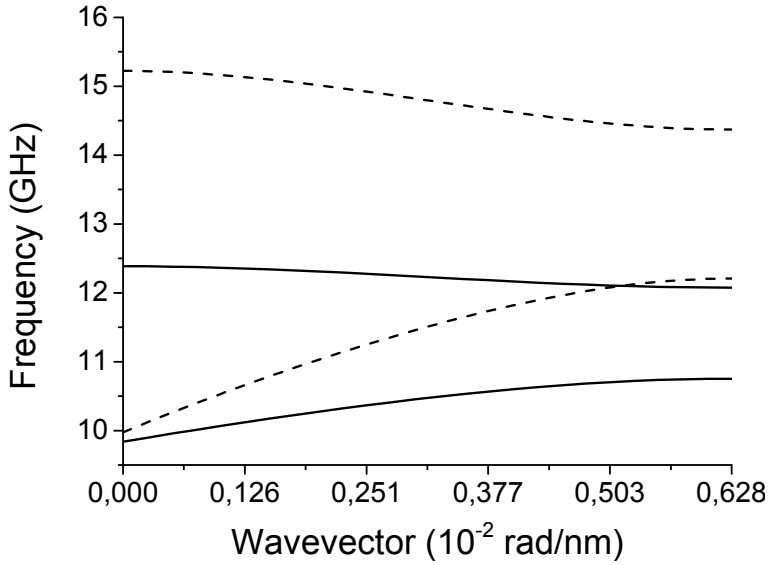

Figure 22. SW spectrum of the studied 1D MC is shown for the slab with the lattice constant $2s = 500$ nm and of $d = 10$ nm thickness. The legend is the same as in Fig. 20.

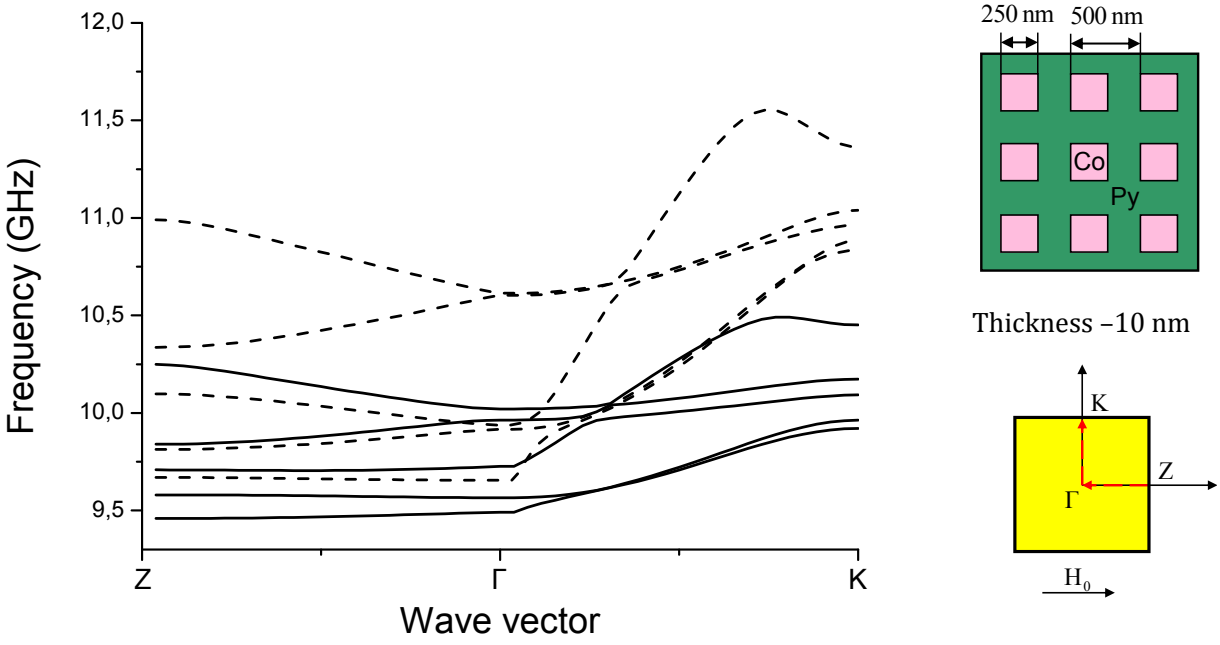

Figure 23. SW spectrum of the considered 2D MC with the Co dots of $q = 250$ nm width (schematically shown in the upper inset). Period of the structure is $a = 500$ nm and thickness of the film is $d = 10$ nm. The legend is the same as in Fig. 20. The 1st BZ of the studied MC is shown in the bottom inset.

η	Dielectric	Metal
$2s = 10$ nm, $d = 1$ nm	0.425	0.421
$2s = 75$ nm, $d = 5$ nm	0.184	0.194
$2s = 500$ nm, $d = 10$ nm	0.116	0.162

Table 1. The relative band gap width η in dependence on the geometry of the considered 1D MC and the type of overlayer.

In order to analyze the width of the first gap the relative band gap width is calculated for different sizes and types of overlayers of the considered 1D planar MC. The results are summarized in Table 1. The relative band gap width is defined as follows: $\eta = \Delta\omega/\omega_c$, where $\Delta\omega$ is the width of the band gap and ω_c is the frequency in the center of the gap. As one can see from Table 1 in the case of large lattice constants ($2s = 500$ nm) one can expect to have about 40% bigger value of the relative band gap width obtained just by adding a metallic coat on top of the structure.

In summary, the PWM has been developed in order to calculate the SW spectrum of planar MCs with a metallic screen on top of it. Significant increase of the group velocity of SWs and a shift of the first band gap up to higher frequencies have been observed in the studied structures. These features could be exploited in magnonic devices based on the phase shift of SWs, e.g., in Mach–Zehnder-interferometer-type ones.

3.5. Antidot lattices. Enhancement of the SW propagation velocity

As it was mentioned in Introduction magnonic devices are better candidates for miniaturization because the wavelength of SWs is several orders of magnitude shorter than that of electromagnetic waves of the same frequency. However, there is a severe obstacle that can hinder potential applications of MCs in microwave electronics. Since SW propagation velocities v_g in periodic systems are much smaller if compared with unstructured films it suggests slow signal processing in nanostructures [18, 104, 166]. For an individual magnetic element of lateral dimension l, the smallest excitable wave vector is on the order of π/l due to spin-wave quantization [167]. For 1 $\mu m > l >$ 10 nm, theory predicts that SWs reside in an intermediate regime between dipolar-dominated and exchange-dominated SW excitations [168]. For SWs in such nanostructures, group velocities are particularly small. To obtain large v_g, MC unit cells were of micrometer [169] and even millimeter dimensions [170], making miniaturization impossible. An important improvement has been achieved by using a MC that consists of a complex unit cell with two different ferromagnetic materials [43]. Here, group velocities are up to 4 km/s at $\mu_0 H = 0$ mT [extracted from Fig. 2(a) of Ref. [43] at $k \approx 1.2 \cdot 10^5$ rad/cm]. However, the device fabrication is challenging. Two exposure and material deposition steps are needed and they have to be aligned precisely on the nanoscale.

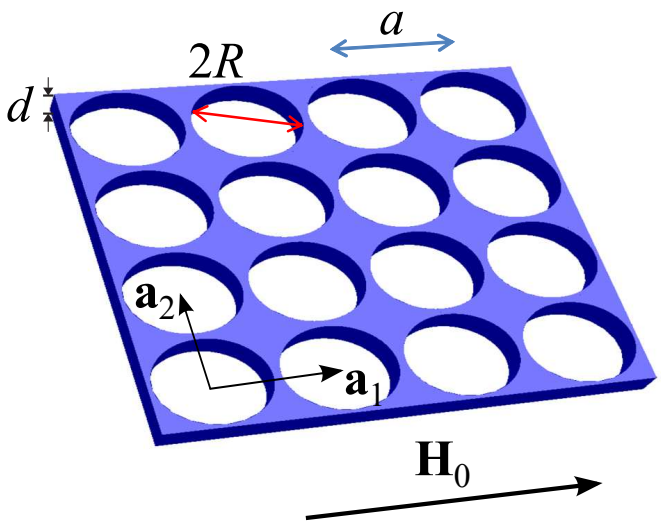

Figure 24. Geometry of the studied ADL structure.

An alternative way of increasing the SW propagation velocity was proposed by S. Neusser et al. in [45]. The authors fabricated and measured a series of 2D MCs consisted of a uniform Py thin film with periodically drilled nanoholes on the surface (see Fig. 24). The ADLs have been prepared by focused ion beam etching, which allowed to

create edge-to-edge separations down to 180 nm. Such configuration of planar MC allowed to generate SWs with strikingly large v_g.

To explain increased velocity of SWs in such systems the PWM is employed. In order to apply this method to ADL structures one needs to consider nonmagnetic media (i.e., the holes), to modify the magnetostatic field calculation method, and to conduct many numerical tests to verify the correctness of the method. Main ideas of how to extend the PWM for the SW spectrum calculations of magnetic structures with nonmagnetic inclusions are presented in subsection 3.3. Detailed analysis and discussion of the considered assumptions will be done in subsection 3.7.

Second form of the exchange field (27), i.e., $\Lambda = \text{II}$ is used in the SW spectrum calculations (56). The following material parameters for Py are chosen: $M_{\text{S,Py}} = 0.86 \cdot 10^6$ A/m and $A_{\text{Py}} = 1.3 \cdot 10^{-11}$ J/m. As it has been explained in subsection 3.3, in order to achieve convergence of the obtained solutions values of the "static magnetization" and "exchange constant" of air are chosen ten times lower than the ones of Py, i.e., $M_{\text{S,air}} = 0.086 \cdot 10^6$ A/m and $A_{\text{air}} = 0.13 \cdot 10^{-11}$ J/m, respectively. The Fourier coefficients of the material parameters can be found in (65). The assumed in calculations thickness of the fabricated films of Py is $d = 25$ nm which is in the range expected from the experimental measurements for these samples.

In Fig. 25(a) the gray-scale plot shows experimental spectra obtained on the ADL with the smallest periodicity $a = 0.3$ μm. The graph in Fig. 25(a) depicts the signal amplitude measured by VNA (data is taken from the paper [45]). Black color indicates a SW resonance. Here, both standing as well as propagating modes are resolved [171]. In Fig. 25(b) BLS data (open circles) taken at $k = 0$ are also depicted. The relevant modes with zero precession amplitude within the holes (i.e., physical solutions) are calculated using the PWM. As a result the dependence of the SW frequency on the external magnetic field is shown in Fig. 25(a) as solid lines. Note that only symmetric modes are plotted here in order to consider the excitation symmetry in the performed measurements. The PWM results and the experimental data are in good agreement.

The PWM is also used to study group velocities v_g for propagating modes in ADLs of different periodicity to explain the experimental data and understand the observed dependences. It has already been reported that ADLs with mesoscopic lattice constants support different SW modes [172–174]. The characteristic eigenfrequencies and spin-precession profiles depend on the lattice symmetry and orientation of the in-plane magnetic field with respect to high-symmetry directions [175]. In Fig. 25(b), v_g measured by AESWS on ADLs with different a are depicted as black circles (data taken from [45]). Micromagnetic simulations were also employed to model local SW excitations in the array of periodic holes in [45]. The results of the simulations are depicted by open squares in

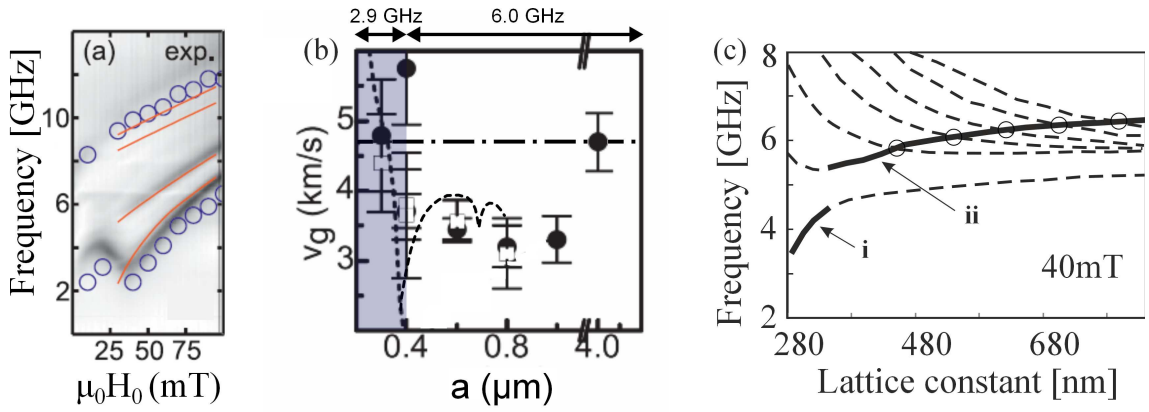

Figure 25. (Copyright © 2011 American Physical Society. This figure is taken from [45]) SW propagation in the ADL structures. (a) Frequency of the SW vs. applied magnetic field. Experimental data taken on an ADL with $a = 0.3$ μm. VNA data in reflection configuration (gray-scale plot, where dark color denotes an SW resonance) and BLS data at $k = 0$ (open circles). Thin solid lines are results of the PWM calculations. (b) Group velocities v_g at $k_{CPW} = 10^4$ rad/cm of propagating modes in ADLs with different a. The experimental values have been obtained by VNA measurements (black circles) and micromagnetic simulations (squares) at $\mu_0 H_0 = 40$ mT and. The horizontal dashed-dot line indicates the group velocity in Py. At $a = 0.4$ μm two modes of different eigenfrequencies which both propagate with a characteristic but different v_g are found. Triangles indicate v_g predicted by PWM. (c) Mode frequencies calculated by the PWM for different a. The thick solid lines mark regions where, for $a < 0.35$ μm the edge mode i and for $a > 0.35$ μm the extended mode ii is predicted to be the propagating mode. Circles mark predicted mode crossings (see text).

Fig. 25(b). For the ADL with $a = 0.4$ μm a transition is resolved. Such structure exhibits the same v_g as the plain film. The minimum $v_g = 3.2$ km/s at $a = 0.8$ μm is observed. It is now interesting that the eigenfrequencies of the prominent modes which propagate through the lattice depend also on a. It is important that the frequency f of the propagating mode at $a = 0.3$ μm with the largest v_g is $f = 2.9$ GHz. $f \approx 6$ GHz is found for the propagating mode when $a > 0.4$ μm. Result of the PWM calculations is depicted as the dashed line in Fig. 25(b) and is in good agreement with the simulation and the experimental data. PWM-calculated velocities are systematically larger than the experimental ones. This discrepancy can be attributed to the misalignment angle, which is assumed to be zero in the PWM calculations but ranges from 1° to 2°. in the experiments. Note the good agreement between the value $v_g = 5.8$ km/s calculated by the PWM at $a = 0.3$ μm and the maximum $v_g = 6$ km/s resolved by AESWS is obtained (see Fig. 25(b)).

The PWM allows us to elucidate the dependence of propagation characteristics on a. In Fig. 25(c), the frequency of the relevant modes is plotted as a function of ADL periodicity a. The thick lines mark the mode with largest v_g. For $a < 0.35$ μm, the edge mode (mode i) is found propagating by means of the PWM and micromagnetic

simulations (see, Ref. [45]). At $a = 0.35$ μm, the PWM predicts a transition to occur in that the mode ii (i.e., the extended mode) propagates for large a. The experimental data is consistent with this transition. In particular, two different propagating modes in one-and-the-same ADL with $a = 0.4$ μm are observed. In the PWM it is found that the extended modes hybridize with transversally quantized modes for certain a, which are highlighted by open circles in Fig. 25(c). The group velocity decreases significantly in the vicinity to hybridization points (see, Fig. 25(b)), so v_{g} is extracted only for specific values of a away from these points of hybridization; namely, for $a = 0.3$, $a = 0.6$, and $a = 0.8$ μm. The repulsion of the dispersion curves appears only when the crossing modes have the same symmetry. The mode with largest v_{g}, as excited in the experiment, is symmetric. It means that the crossing at a around 0.44, 0.62, and 0.78 μm will change neither the dispersion nor the group velocity. When repulsion between dispersion curves exists, the flattening of the dispersion results in a decrease of v_{g}.

To explain the high v_{g} of the propagating mode at $a = 0.3$ μm, microscopic details of the excitations were investigated using simulations and semianalytical approaches in [45]. It was shown that regions of large spin-precession amplitude at $f = 2.9$ GHz reside close to the edges of the holes where the demagnetizing field H_{ms} (in [45] this field is marked as H_{d}) forms potential wells with a strong peak-to-peak variation $\mu_0 \Delta H_{\mathrm{ms}} = 100$ mT[4] (see Fig. 4(d) in [45]). The amplitude of this variation is found to depend almost only on the hole shape and not on the ADL period a. Using theoretical SW dispersion relations from Ref. [168] and the values $H_{\mathrm{ms}}(\mathbf{r}_{\parallel})$ obtained by micromagnetic simulations, it was demonstrated that resonant spin precession at $f = 2.9$ GHz is substantiated to occur only in the minima of H_{ms}, very close to the edges of the holes. In the intermediate regions, the nonzero amplitudes reflect off-resonance excitation. It was also found that, at $a = 0.3$ μm, excited regions at neighboring holes overlap with nonzero amplitude in between the holes. This is in contrast to the ADL with $a = 0.8$ μm (see Fig.4(b) in [45]), where the edge excitations of the individual holes were found to be separated by regions of zero precession amplitude. In this scenario, propagation is suppressed for the edge mode. Instead, the higher-frequency mode (i.e., the extended mode at 5.6 GHz) propagates.

For an unpatterned plain Py film it is known [168] that, in the long-wavelength limit, the main contribution to the dynamic coupling comes from the dynamic magnetostatic one. For example, in the Damon-Eshbach configuration where $\mathbf{k} \perp \mathbf{M}_{\mathrm{S}}$ the dynamic magnetostatic coupling leads to a steep slope in the dispersion relation and thereby a large group velocity v_{g}. In the considered case the experimental finding of large v_{g} is believed to be attributed to the fact that SWs tunnel between the neighboring resonant

[4] Note that, despite the fact that $-H_{\mathrm{ms}} > H_0$, the spins are stabilized in their magnetization configuration due to an effective positive contribution of the exchange field.

oscillators localized at the holes' edges [20, 176]. The strength of such tunneling depends on the tunneling distance, the film thickness, and the susceptibility of the material through which the SW tunnels [20, 177, 178]. A large susceptibility χ of a material amplifies the magnetostatic stray field and thereby increases the magnetostatic coupling strength (i.e., tunneling probability) between both sides of the tunnel barrier.

In summary, artificial crystal behavior in a nanopatterned ADL has been reported. The PWM has been adapted to describe the devices and reproduce the experimental findings. The large SW velocities create interesting perspectives in the field of nanoscale magnonic devices.

3.6. Propagation of SWs in a rhombic ADL

Let us continue studying ADL structures started in the previous subsection. Here, rhombic ADLs will be of particular interest. Such systems have been less well investigated so far [179–181] as compare to squared ADLs. For such non-squared lattices experimental data have been presented for a wave vector $k = 0$ only [174]. Considering an antidot array as a mesh of interconnected wave guides it is interesting to study SW propagation and possible anisotropic behavior at $k \neq 0$. It is of particular interest whether the periodic arrangement of holes forms an artificial crystal for spin waves, i.e., a MC and gives rise to miniband formation as well as forbidden frequency gaps. In this subsection SW modes in an ADL where nanostructured holes are arranged on a rhombic lattice are investigated. The PWM is implemented to calculate the spectra of magnetostatic surface spin waves (MSSW) and magnetostatic backward volume waves (MSBVW) for wave vectors in different high symmetry directions. From the calculations it is found that many mode branches coexist at large frequencies. There allowed minibands and forbidden frequency gaps are not clearly formed. The findings are relevant for research on SW filters and wave guides based on periodically patterned nanomagnets as well as MCs [33, 43, 49, 52]. Results of the research presented here has been sent for publication to the Physical Review B [46].

The geometry of the structure under consideration is shown in Fig. 26(a). It is represented by a $d = 30$-nm-thick film of Py with an infinite array of holes arranged on a rhombic lattice. The lattice constant is taken to be $a = 400$ nm. To obtain agreement with experimental results, especially for edge modes, the radius of the holes is increased to the value of $R = 130$ nm that is 4% larger than the nominal one. Second form of the exchange field (27), i.e., $\Lambda = \mathrm{II}$, is used in the PWM calculations. The magnetization saturation of $M_\mathrm{S} = 0.8 \cdot 10^6$ A/m and the exchange constant of $A = 1.0 \cdot 10^{-11}$ J/m are chosen for Py for better fitting with the experimental data. As before values of the

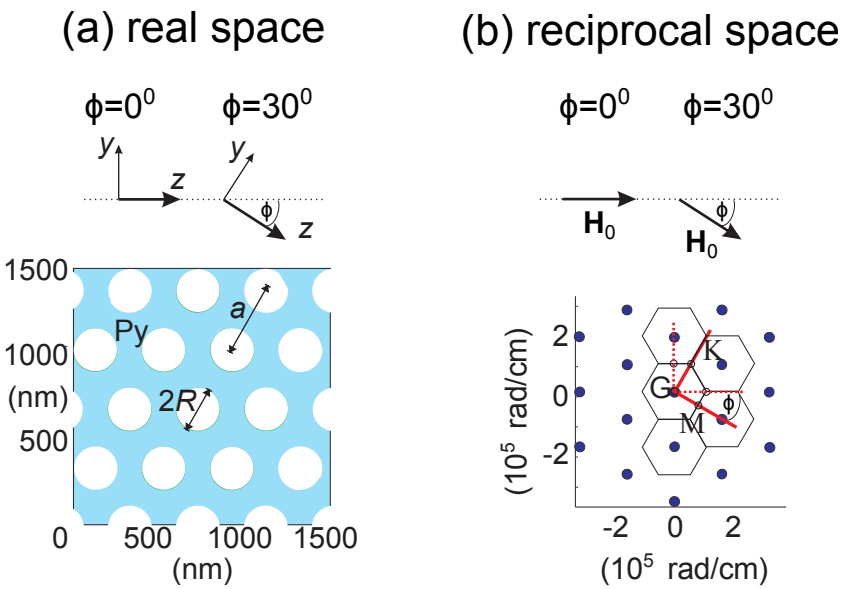

Figure 26. (a) Rhombic-lattice based ADL considered in this study. Antidots are represented by white holes with radius R; the magnetic field is always oriented along the $\hat{z}$-axis, i.e., in the $\phi = 0°$ geometry along the horizontal line, in the $\phi = 30°$ geometry along the line clockwise-rotated by 30°. (b) Reciprocal space for the structure shown in (a), with indicated high-symmetry points Γ, K and M in the center and at the border of the 1st BZ, respectively. Solid (dotted) lines represent the wave-vector range studied in BLS experiments, i.e., from 0 to 2.0 $\cdot 10^5$ rad/cm along $\mathbf{H}_0$ and perpendicular to $\mathbf{H}_0$ in $\phi = 30°$ ($\phi = 0°$) geometry. The $\hat{x}$-axis is out of the plane.

"magnetic parameters" of the holes are assumed to be ten times lower than the ones of Py. The bias field is applied along the $\hat{z}$-axis and equal to $\mu_0 H_0 = 0.09$ T. To address the two configurations studied in the experiments ($\phi = 0$ and 30°) the ADL is rotated while the bias field remained in the same direction (see, Fig. 26(a)).

The band structure of the considered MC is calculated by solving numerically the eigenvalue problem (56) with the Fourier coefficients of the material parameters calculated according to the following formula:

$$X(\mathbf{G}_\parallel) = \begin{cases} \dfrac{2\pi R^2}{\sqrt{3}a^2}(X_{\text{air}} - X_{\text{Py}}) - X_{\text{Py}}, & \text{for } \mathbf{G}_\parallel = 0 \\ \dfrac{4\pi R^2}{\sqrt{3}a^2}\dfrac{J_1(|\mathbf{G}_\parallel|R)}{|\mathbf{G}_\parallel|R}(X_{\text{air}} - X_{\text{Py}}), & \text{for } \mathbf{G}_\parallel \neq 0 \end{cases} \tag{72}$$

where X_{air} and X_{Py} are the material parameters, i.e, M_{S} or l_{ex}^2 of the holes and Py matrix, respectively; J_1 is a Bessel function of the first kind, R is the radius of a hole; $\mathbf{G}_\parallel = (G_y, G_z)$ denotes a reciprocal lattice vector of the studied structure that in the case when $\phi = 0$ can be written as $\mathbf{G}_\parallel = \frac{2\pi}{a}(\frac{2n_y - n_z}{\sqrt{3}}, -n_z)$, and when $\phi = 30°$ – $\mathbf{G} = \frac{2\pi}{a}(n_y, (2n_z - n_y)/\sqrt{3})$ (n_y, and n_z are integers). The reciprocal lattice of the rhombic structure is shown in Fig. 26(b). The solid (dotted) lines along two orthogonal directions represent the wave-vector range studied in BLS experiments for the $\phi = 30°$ ($\phi = 0$)

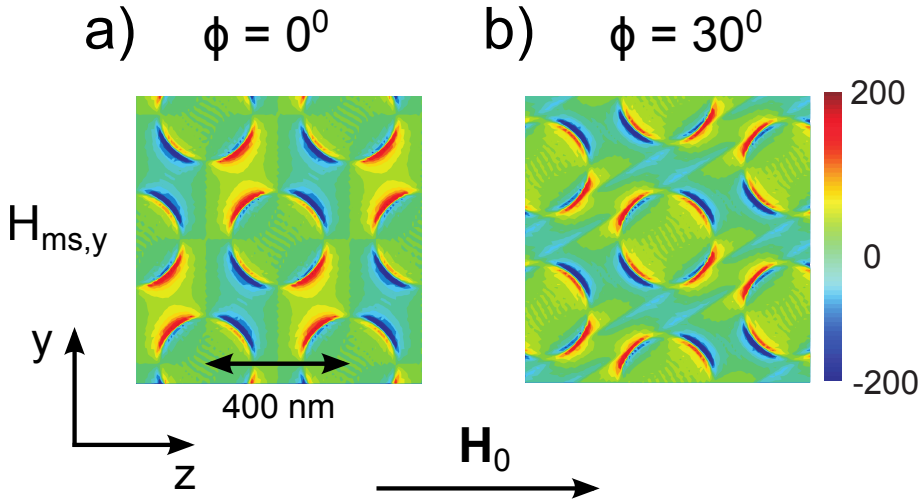

Figure 27. Component $H_y(\mathbf{r}_\parallel)$ of the static demagnetizing field calculated according to (44) and (53) in the ADL for the two different orientations of $\mathbf{H}_0$: (a) $\phi = 0$, (b) $\phi = 30°$. Note that the lattice is rotated by 30° between the left and right plots.

geometry. ϕ is the angle between bias magnetic field $\mathbf{H}_0$ and the dotted horizontal line in the structure presented in Fig. 26(a).

The non-zero magnetization is intentionally attributed to the holes. A non-zero value is needed for the convergence of the eigenvalue problem (56) (see, the discussion in subsections 3.3 and 3.7). Ten times lower value of the saturation magnetization of the holes than the one of Py is assumed in the calculations. Satisfactory convergence of the numerical solution of (56) for the considered MC is found for $N = 1681$ reciprocal lattice vectors.

The static component of the demagnetizing field $H_y(\mathbf{r}) = -\partial\varphi_i(\mathbf{r})/\partial y$ (perpendicular to $\mathbf{H}_0$) in the considered MC calculated from (53) is shown in Fig. 27(b) and (d). The regions of the ADL with maximum and minimum values of $H_y(\mathbf{r})$ point out the regions where the direction of the static magnetization can easily deviate from the saturated state assumed in the PWM formalism. Neglecting the nonuniform static magnetic field perpendicular to $\mathbf{H}_0$ is justified for strong external fields which saturate the ADL or for the SW modes which have large precession amplitude concentrated in the regions with negligible $H_y(\mathbf{r})$, e.g., for the edge modes. It means also that PWM results for the SWs which have precession amplitudes spread across the ADL can be used only for the qualitative interpretation of the experimental results.

When the eigenvectors in (56) are known the relative intensities of BLS spectra for different angles of the incident light can be calculated (see, e.g., [182]). For propagating SWs only the perpendicular-to-the-ADL-film component of the dynamical magnetization $m_x(\mathbf{r}_\parallel) \propto \mathrm{e}^{i(\mathbf{k}_\parallel \cdot \mathbf{r}_\parallel - \omega t)}$ will contribute to the inelastic light scattering process at the incident angle of the light which determines the wave vector $\mathbf{k}_\parallel$. If the investigated SW mode is

described by a mode profile $\mathbf{m}(\mathbf{r}_\parallel)$, the intensity is determined by the Fourier component $m_{x,\mathbf{k}_\parallel}(\mathbf{G}_\parallel = 0)$ of the mode:

$$I \propto |m_{x,\mathbf{k}_\parallel}(0)|^2. \tag{73}$$

It means that the square of the modulus of the fundamental harmonics $m_{x,\mathbf{k}_\parallel}(0)$ is proportional to the BLS response [174]. In this description $\mathbf{k}_\parallel$ does not need to be limited to the first BZ and can span over any point of the reciprocal space. The range of wave vectors investigated in this study are marked by solid and dashed lines in Fig. 26(b).

1. MSSW geometry for $\phi = 30°$ with $k_y \neq 0$

For the MSSW geometry with $\phi = 30°$ the magnonic band structure and relative BLS intensities calculated by the PWM are shown in Fig. 28(a) and (c), respectively. In Fig. 28(a) the PWM results (lines) are superimposed on the BLS data (circles) that is taken from the submitted article [46]. Magnonic bands with predicted large scattering cross sections are emphasized by bold lines. In agreement with BLS data the intensity of the low-frequency edge mode, i.e., mode E, disappears at the border of the 1$^{\text{st}}$ BZ (K point in Fig. 26(b)), while mode E_{AS} starts to be visible. From the calculated spin-precession amplitudes (Fig. 28(b)) one can see that two modes E and E_{AS} are edge modes with in-phase (symmetric) and π phase-shifted (antisymmetric) oscillations, respectively, in the unit cell. The E_{AS} mode is visible at large wave vectors when the mode wavelength matches the one probed by BLS. In agreement with the experimental results, the PWM calculations show that the mode E exhibits a significant dispersion in the 1$^{\text{st}}$ BZ. The group velocity of 2.6 km/s is obtained in the numerical calculations at $k_y = 0.05 \cdot 10^5$ rad/cm, being in a good quantitative agreement with the measured value. Such relatively large group velocity can be attributed to a strong interaction between the edge excitations of neighbouring holes which oscillate in phase. The strong coupling allows spin waves to propagate from hole to hole. The PWM thus substantiates deep-submicron SW channels between rows of holes (see mode E in Fig. 28(b)). For the mode E, the PWM calculations predict the formation of a miniband that has not been resolved experimentally due to the low cross-section of this mode for $k_y > 0.8 \cdot 10^5$ rad/cm. In contrast, the mode E_{AS} is almost independent on $\mathbf{k}_\parallel$ in the 1$^{\text{st}}$ BZ. The out-of-phase edge modes between neighboring holes are much less coupled and as a consequence SWs can not propagate.

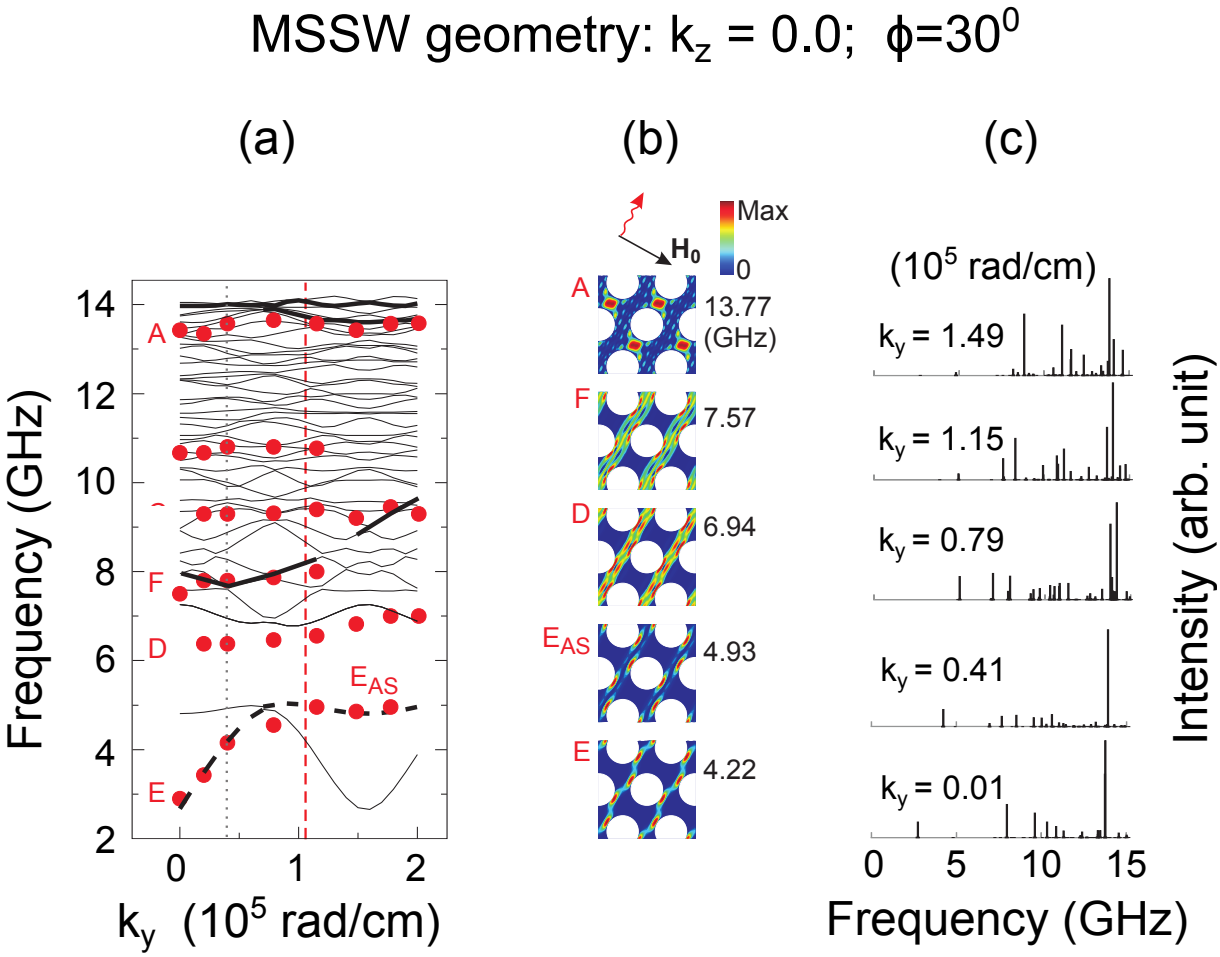

Figure 28. (a) Magnonic band structure in MSSW geometry for $\phi = 30°$ ($k_z = 0$). Circles represent peaks in BLS spectra. Thin lines are the results of the PWM calculations. Bold and dashed bold lines emphasize intense excitations as predicted by the PWM. The vertical dashed line marks the border of the 1st BZ (i.e. the K point) while the dotted line indicates the $\mathbf{k}_{\|}$-vector where modes profiles of panel b) is calculated. (b) Maps show spin-precession profiles, i.e., modulus of the amplitude of $m_x(\mathbf{r}_{\|})$, at $k_y = 0.41 \cdot 10^5$ rad/cm. The most intense modes E, E_{AS}, D, F and A are displayed. Modes E and E_{AS} are edge modes. (c) Relative values of BLS intensities calculated by the PWM for different values of k_y are given in 10^5 rad/cm. The intensities of E and E_{AS} modes interchange at $k_y = 0.79 \cdot 10^5$ rad/cm.

From Fig. 28 it is found that the rhombic lattice gives rise to numerous modes of different intensities at high frequencies. Many of them exhibit only a small or vanishing slope as a function of k_y.

2. MSBVW geometry for $\phi = 30°$ *with* $k_z \neq 0$

In Fig. 29(a) the experimental and calculated frequencies are depicted for the MSBVW geometry for $\phi = 30°$. In this geometry, nearly all the modes exhibit the independence on the wave vector of the SWs, i.e., they are quantized. In Fig. 29(b), the modulus of $m_x(\mathbf{r}_\parallel)$ is shown for the most intense modes at $k_z = 0.41 \cdot 10^5$ rad/cm. From Fig. 29(a) and (b) one can see that the edge excitations (mode E) do not couple significantly for $\mathbf{k}_\parallel$ being perpendicular to the SW nanochannels. Concentration of the amplitude of the A mode between holes along the direction perpendicular to $\mathbf{H}_0$ is observed in Fig. 29(b). This mode is most intense for small values of k_z (Fig. 29(c)) but starting at $k_z \approx 1.78 \cdot 10^5$ rad/cm the intensity of the mode C become comparable. Mode C is similar to the mode A, but with one nodal plane along $\mathbf{H}_0$. It means that this mode can be interpreted as a higher-order backward volume mode, thereby residing at a smaller frequency.

3. MSSW geometry for $\phi = 0°$ *with* $k_y \neq 0$

For the wave vectors perpendicular to $\mathbf{H}_0$ the dispersion relation exhibits mirror symmetry with respect to the border of the 1$^{\text{st}}$ BZ at $\phi = 0°$. The PWM results (lines) are superimposed on the measured BLS frequencies (circles) in Fig. 30(a). Magnonic bands with a large scattering cross section are emphasized by bold lines. In Fig. 30(c) relative intensities calculated by the PWM are presented.

The spin-precession profiles of modes with the most intense peaks at $k_y = 0.41 \cdot 10^5$ rad/cm are presented in Fig. 30(b). The edge excitations forming the low-frequency mode $\mathrm{E_{AS}}$ are found to precess out-of-phase. The scattering cross section is small and, consistently, the mode $\mathrm{E_{AS}}$ is not detected by BLS in the whole wave vector range. The higher mode E has a nonzero peak in the BLS spectra that is in a good agreement with a large intensity predicted by the PWM (bold line in Fig. 30(a)). The PWM predicts the mode E to form a narrow allowed miniband with the minimal frequency at $\mathbf{k}_\parallel = 0$ and

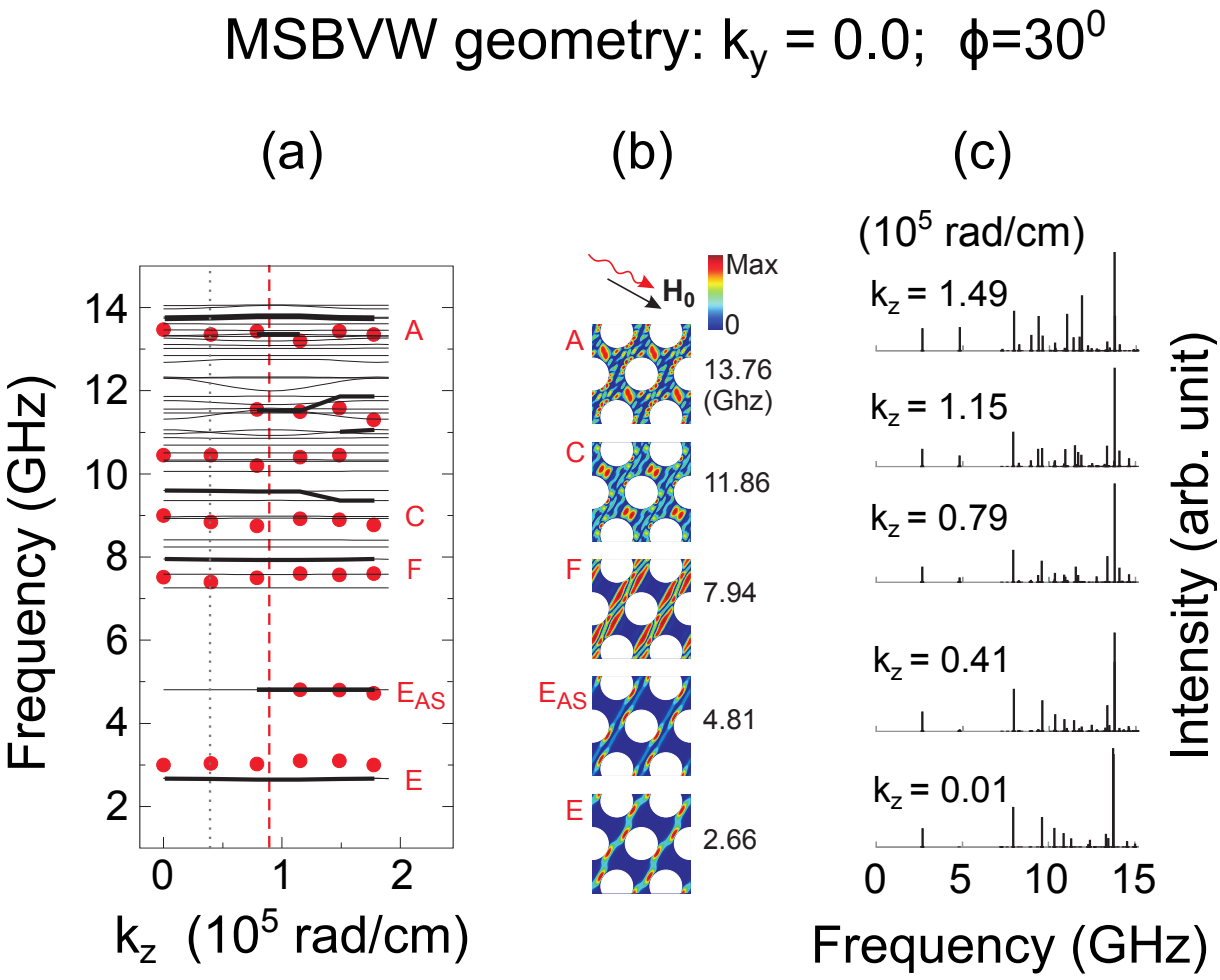

Figure 29. (a) Magnonic band structure in the MSBVW geometry for $\phi = 30°$ ($k_y = 0$). Circles represent peaks from BLS spectra. The thin lines are the results of the PWM calculations. Bold lines emphasize the modes with high intensities calculated by the PWM. The vertical dashed line marks the border of the 1st BZ (i.e. the M point) while the dotted line indicates the wave vector where mode profiles of panel b) are calculated. (b) Color maps show modulus of m_x of the modes E, E_{AS}, F, C and A at $k_z = 0.41 \cdot 10^5$ rad/cm. (c) Relative values of BLS intensities calculated by the PWM for different values of k_z (values are given in units of 10^5 rad/cm). The intensity of mode E_{AS} is close to zero near the center of the BZ and starts to appear at $k_z = 0.41 \cdot 10^5$ rad/cm. Then, its intensity increases with increasing k_z.

the maximal one at the border of the BZ. However in the BLS experiment this mode is practically flat. Numerous further modes of weak intensities are predicted by the PWM.

4. MSBVW geometry for $\phi = 0°$ with $k_z \neq 0$

Calculated magnonic band structure and BLS intensities are shown in Fig. 31(a) and (c), respectively, considering the MSBVW geometry at $\phi = 0°$. Interestingly, a low frequency mode appears in the BLS spectra for $k_z > 1.0 \cdot 10^5$ rad/cm and a frequency below 5 GHz. The observation of this low frequency mode is consistent with the result of the PWM calculations which predict an increasing intensity (see Fig. 31(c)) for this mode when k_z is larger that 10^5 rad/cm. Inspection of the spatial profile for this mode indicates that it is localized in the vicinity of the holes' edge and with an antisymmetric character. This explains why it is visible only for large wave vectors when the mode wavelength matches the one of the probing light.

The BLS data (Fig. 31(a)) shows that the mode A exhibits a negative slope with the increase of k_z. The PWM predicts a similar branch in the SW spectrum of the considered structure at a slightly higher frequency. A miniband behavior is not found. The mode crosses the edge of the BZ with a nearly constant slope. Spin-precession profiles of selected modes in the MSBVW geometry for the case of $\phi = 0°$ are presented in Fig. 31(b).

Aside from a good agreement between the results of the PWM calculations and BLS data for the low-frequency edge modes, there is a quantitative difference in BLS intensities for the modes with higher frequencies. The source of this discrepancy may lie in assumptions of the PWM. Here, a uniform magnetization and absence of components of the static demagnetizing field perpendicular to $\mathbf{H}_0$ are assumed. Both assumptions are connected with each other as the demagnetizing field provokes locally a rotation of magnetic moments away from the direction of the bias field.

In summary, it has been shown that rhombic ADLs open novel perspectives for SW guiding. SWs of both, positive and negative group velocities propagate through the lattice. These dynamic properties are relevant for the research field of magnonics where transmission and modification of SWs are considered for magnetic nanodevices operating in the GHz frequency regime. A good agreement between the results of the PWM calculations and the experimental data has been found. It validates the method developed in this thesis.

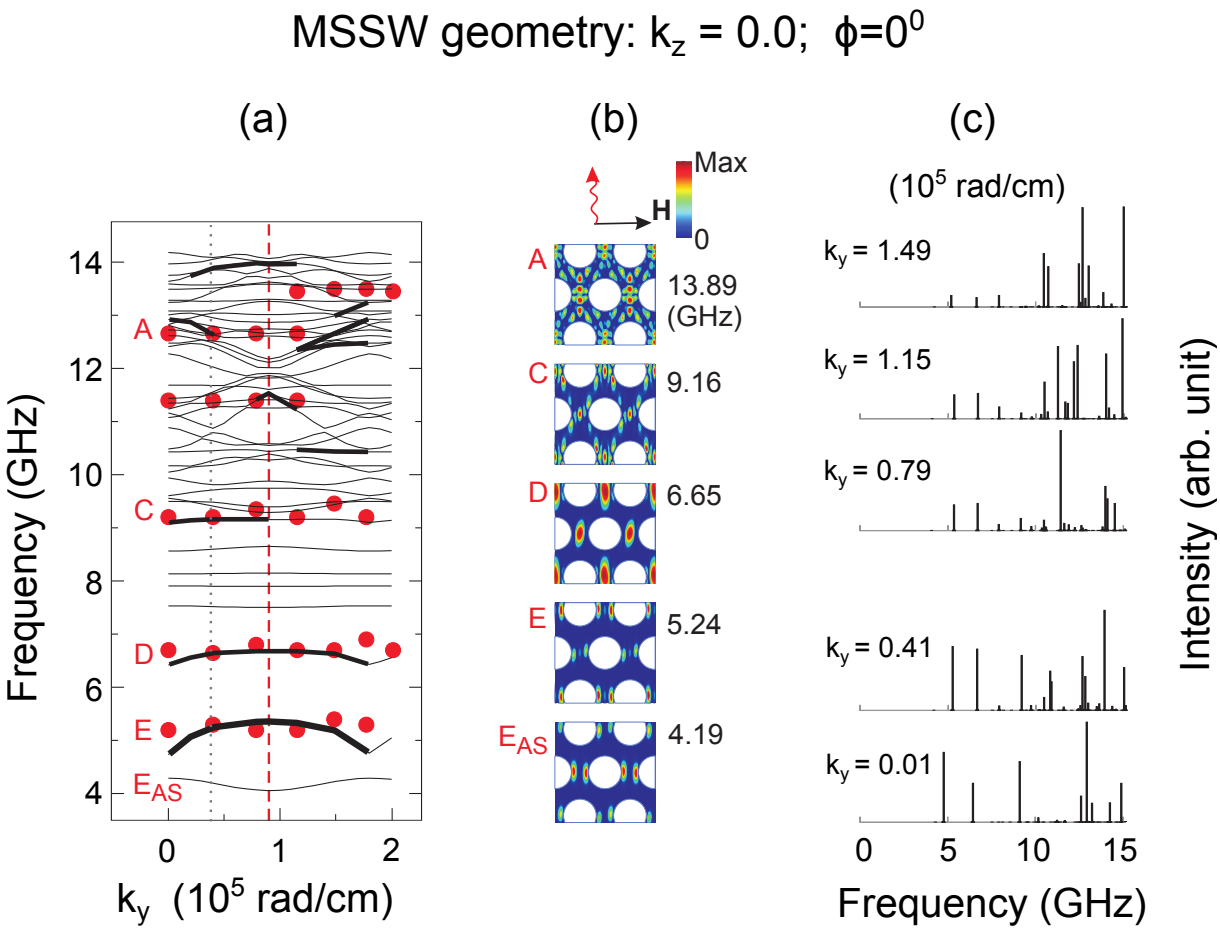

Figure 30. (a) Magnonic band structure in the MSSW geometry for $\phi = 0°$ ($k_z = 0$). Circles represent peaks of the BLS spectra. The thin lines are the results of the PWM calculations. Bold lines emphasize modes with high intensities calculated by the PWM. The vertical dashed line marks the border of the 1st BZ (i.e. the M point) while the dotted line indicates the wave vector where mode profiles of panel b) are calculated. (b) Color maps show modulus of m_x of the modes E_{AS}, E, D, C and A for the case of $\phi = 0°$ and $k_y = 0.41 \cdot 10^5$ rad/cm. The modes E_{AS} and E are edge excitations of different symmetries. (c) Relative values of BLS intensities predicted by the PWM for different values of k_y that are given in 10^5 rad/cm units. There is a good agreement between the results of the PWM calculations and BLS data for the edge excitations: mode E_{AS} is extremely weak while mode E has a significant intensity.

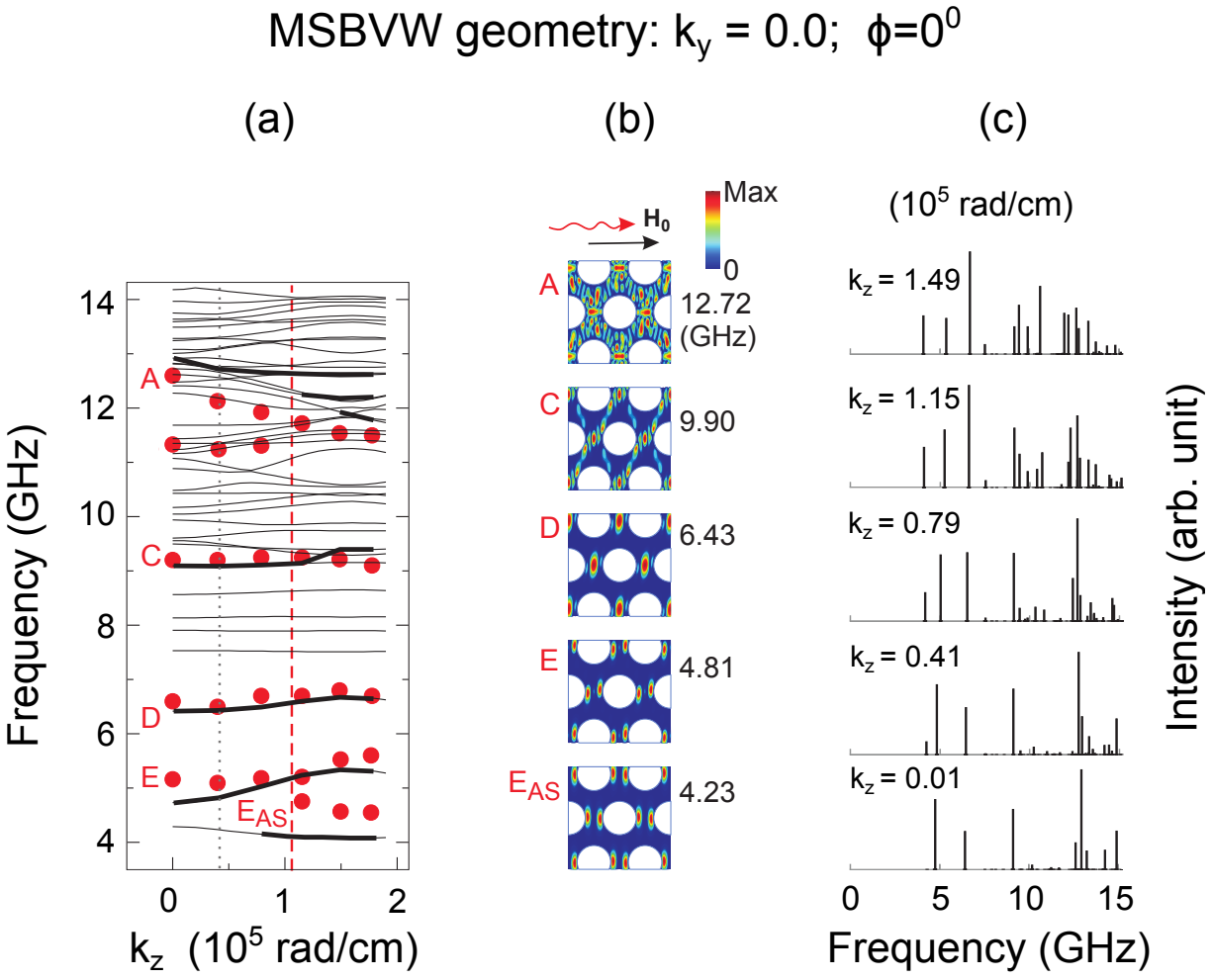

Figure 31. (a) Magnonic band structure in the MSBVW geometry ($k_y = 0$) for the case of $\phi = 0°$. Circles represent the points from the BLS measurements, whilst the thin lines are the results of the PWM calculations. Bold lines emphasize the modes with high intensities as predicted by the PWM. The vertical dashed line marks the border of the 1st BZ (i.e. the K point) while the dotted line indicates the wave vector where mode profiles of panel b) are calculated. (b) Color maps show modulus of m_x of the most intense modes E_{AS}, E, D, C and A for the case when $\phi = 0°$ and $k_z = 0.41 \cdot 10^5$ rad/cm. (c) Relative values of BLS intensities calculated using the PWM for SWs propagating along $\hat{z}$-axis for different values of k_z that are given in 10^5 rad/cm units.

3.7. Limitations of the developed PWM. Test of the assumed approximations

Any method of investigation of a real object in science has its own limits. Always when a scientist models any natural phenomenon he/she classifies and orders by relevance all its features. Thereafter he/she selects the most relevant ones under the particular conditions of the studied object. Of course there is always some information about the considered structure that is lost in the model, therefore each model has its validity range where it describes the object or phenomenon with sufficient accuracy.

During the current research of planar MCs there has been done several approximations that should be subjected to testing:

- Uniformity of the demagnetizing field across the thickness of the MC.
- Absence of the stray field perpendicular to the external field.
- Use of nonzero but small value of the saturation magnetization of a nonmagnatic medium.

The magnetostatic field has been calculated analytically in subsection 2.1. In a general case of a planar 2D MC the static component of the internal magnetic field is given by equation (55a). In order to justify assumptions mentioned above for the wider range of material parameters the dots are chosen to be surrounded by air (or any other nonmagnetic material). This will increase the magnetization saturation and exchange contrasts to their maximum values.

The system to be considered is represented by a periodic array of squared Py dots surrounded by air. Width of the dots, period of the lattice and thickness of the slab are $q = 450$ nm, $a = 520$ nm and $d = 30$ nm, respectively. The magnetic parameters of Py are assumed as follows: $M_{\mathrm{S,Py}} = 0.82 \cdot 10^6$ A/m for the saturation magnetization and $A_{\mathrm{Py}} = 1.3 \cdot 10^{-11}$ J/m for the exchange constant. The calculations are performed according to (55a) with $N = 401$ reciprocal lattice vectors taken into account. Fourier coefficients of the saturation magnetization of the studied MC can be found in (70).

The dependence of the component of the stray field parallel to the direction of the applied field on the position along the $\hat{z}$-axis in a Py dot is shown in Fig. 32. The red line represents the field calculated at the middle of the dot, whilst the blue dashed line is its value taken at the surface of the considered structure. As one can see the difference between these lines is visible only at the edges of the dot while in the middle the field is almost uniform and independent on the position across the thickness. Obviously, the mismatch in the vicinity of the interface between two different magnetic materials will decrease with the decrease of their magnetization saturation contrast.

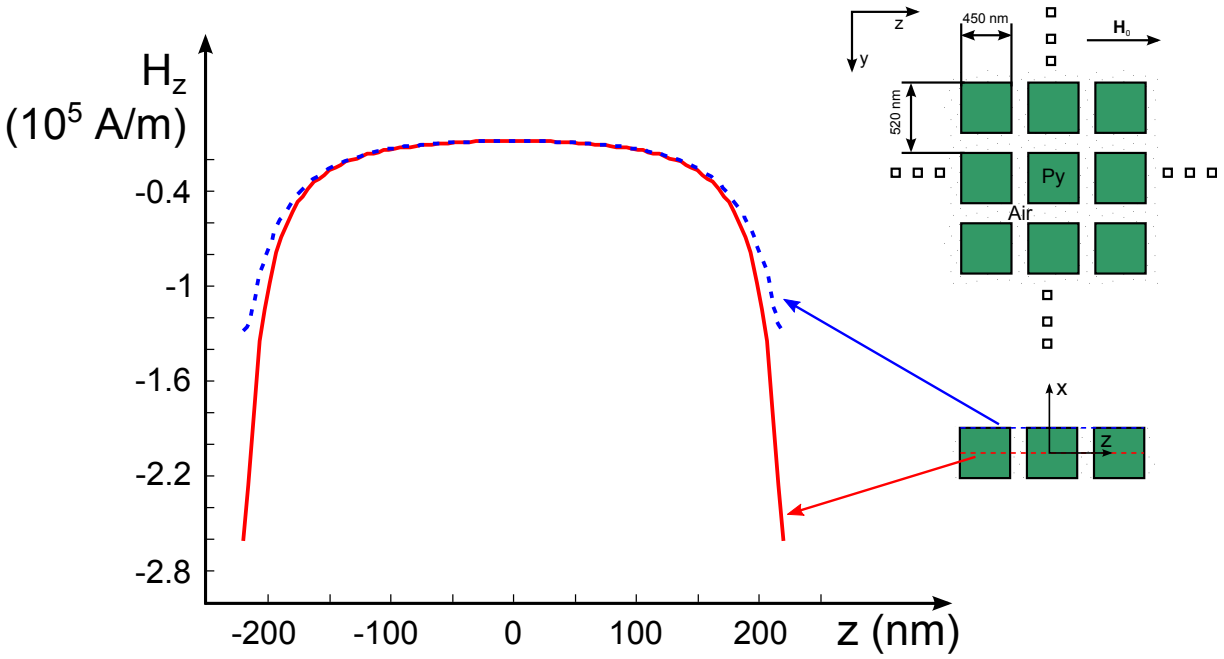

Figure 32. The component of the demagnetizing field parallel to the direction of the external field in dependence on the position along the $\hat{z}$-axis. The red solid line represents the field taken at the middle of the slab, whilst the blue dashed line is its value taken at the surface of the MC.

In addition to the analytical method of studying MCs the Nmag micromagnetic simulation package [183] is employed. Nmag is a flexible finite element micromagnetic simulation package with an user interface based on the Python programming language. This software has been developed at the University of Southampton.

Calculations are performed on the example of a 2D planar MC which unit cell is shown in Fig. 33. It is comprised of a 3×3 array of squared Py dots of $q = 450$ nm width and $d = 30$ nm thickness. The distance between the dots is $p = 70$ nm. Fourier coefficients $M_{\mathrm{S}}(\mathbf{G}_{\parallel})$ of the saturation magnetization used in (55a) can be calculated analytically for the considered structure as follows:

$$M_{\mathrm{S}}(\mathbf{G}_{\parallel}) = \begin{cases} 9\dfrac{q^2}{a^2}(M_{\mathrm{S,Py}} - M_{\mathrm{S,air}}) + M_{\mathrm{S,air}}, & \text{for } \mathbf{G}_{\parallel} = 0 \\ \dfrac{4}{a^2 G_x G_y} \dfrac{\sin(\frac{3}{2}G_x D)\sin(\frac{3}{2}G_y D)\sin(G_x \frac{q}{2})\sin(G_y \frac{q}{2})}{\sin(G_x \frac{D}{2})\sin(G_y \frac{D}{2})}(M_{\mathrm{S,Py}} - M_{\mathrm{S,air}}), & \text{for } \mathbf{G}_{\parallel} \neq 0 \end{cases} \tag{74}$$

where $D = p + q$.

The demagnetizing field perpendicular to the direction of the applied field in dependence of the position inside the central dot along the $\hat{y}$-axis is shown in Fig. 34. The calculations are performed according to (55a) with $N = 1001$ reciprocal lattice vectors taken into account. The data obtained in micromagnetic simulations is represented by the red and blue lines whilst the results of analytical calculations are demonstrated by

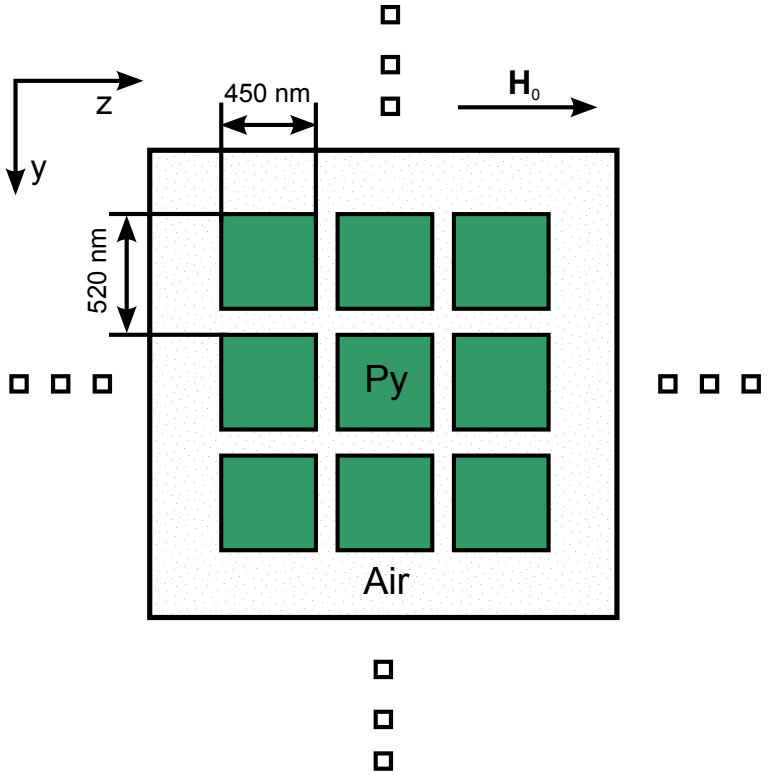

Figure 33. Geometry of a supercell of the studied planar structure. It comprised of a 3×3 array of squared Py dots of $q = 450$ nm width and $d = 30$ nm thickness that are surrounded by air. Distance between the dots is $p = 70$ nm and width of the supercell is $a = 50(q + p)$.

the black and green lines. As one can see a good agreement obtained between the results of both approaches - micromagnetic simulations and analytical modeling. As in the case of the stray field parallel to the external field here a significant mismatch is observed only at the edges of the Py dot. Apart from that the field retains 0 value everywhere in the middle of the central dot.

Concerning the dynamic component of demagnetizing field $\mathbf{h}(\mathbf{r})$ it is necessary first to calculate the dynamic magnetization vector $\mathbf{m}_{\mathbf{k}_\parallel}(\mathbf{G}_\parallel)$ from the LL equation (56). Then using obtained values one can calculate the dynamic stray field given by (55b) and (55c). It is quite complicated task, however due to similar structure of the formulas in (55) one can conclude that the result for the dynamic components of the internal magnetic field won't differ much from the one discussed above.

Another issue in the PWM is absence of the convergence of the solution of an eigenvalue problem for the case of a MC with nonmagnetic inclusions. In order to overcome this problem one can use small but nonzero values of magnetic parameters of the nonmagnetic medium. Influence of this assumption on the static demagnetizing field is shown in Fig. 35. The ADL structure studied in subsection 3.5 is considered here (see, Fig. 35(a)). Diameter of the holes is $2R = 460$ nm, period of the lattice is $a = 630$ nm and thickness of the film is $d = 30$ nm. Material parameters of Py are the same as in previous subsection. The

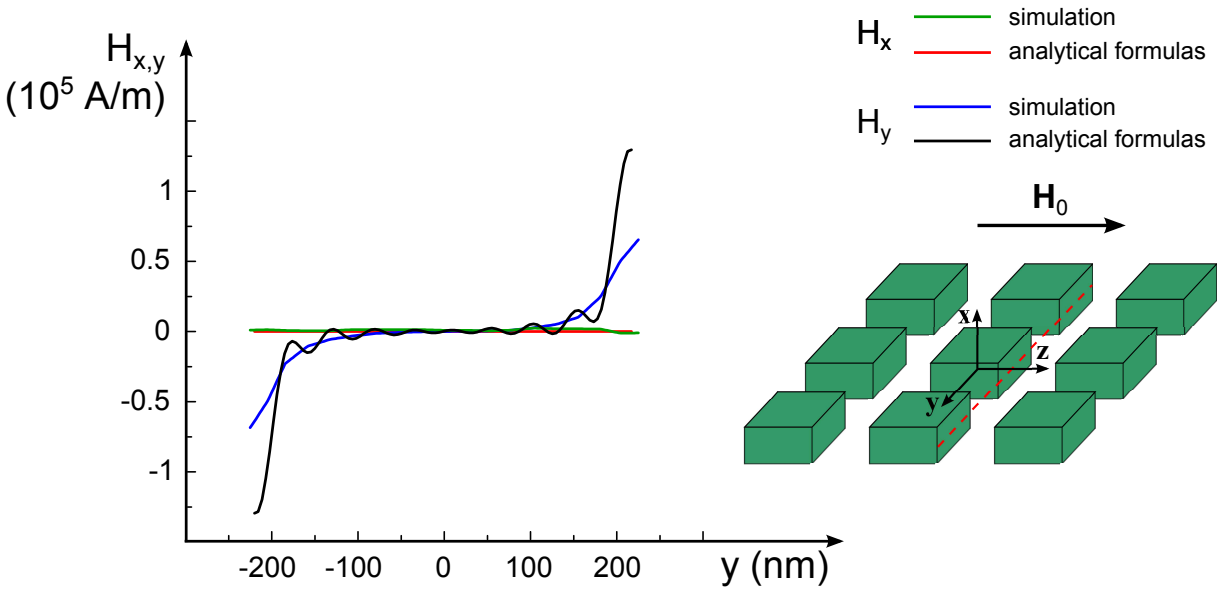

Figure 34. Components of the stray field perpendicular to the direction of the applied field versus position inside the central dot along the $\hat{y}$-axis. The red and blue lines represent data obtained in micromagnetic simulations whilst the black and green lines are the results of the analytical calculations. The red dashed line in the right inset shows the path in the structure along which the demagnetizing field is calculated.

component of the demagnetizing field parallel to the external field is calculated according to (55a). As one can see from Figs. 35(b),(c),(d) the difference between its values for the cases of purely nonmagnetic material of the "holes" with $M_S = 0$ A/m and when the "holes" are modelled as a magnetic medium with $M_S = 0.1 \cdot M_{S,Py}$ A/m is minor reproducing the shape and value of the demagnetizing field with less than 10% error.

Generally speaking, the problem of nonmagnetic inclusions is more complicated. The difficulties lie in the very formulation of the LL equation for inhomogeneous media. This equation describes the dynamics of the magnetization vector in magnetic materials; in nonmagnetic media the magnetization is zero, and the LL equation becomes undefined. It implies the occurrence of nonphysical solutions which describe the dynamic components of the magnetization vector in the nonmagnetic material in the total set of solutions. In the ADL under consideration the static magnetization cuts across the borders between a ferromagnet and a nonmagnetic material. This results in the large locally observed decrease of the internal magnetic field in the magnetic material by the inhomogeneous static demagnetizing field. At the same time, the stray field substantially increases the value of the internal magnetic field in the holes. It can be observed in the color map shown in Fig. 35(c). In other words, the stray field causes the nonphysical solutions to shift up to higher frequencies. The exact frequency range in which the nonphysical solutions occur depends on the structure of the MC. If the shift is not sufficient to push apart in the frequency scale the nonphysical solutions, a further shift is required. For this purpose,

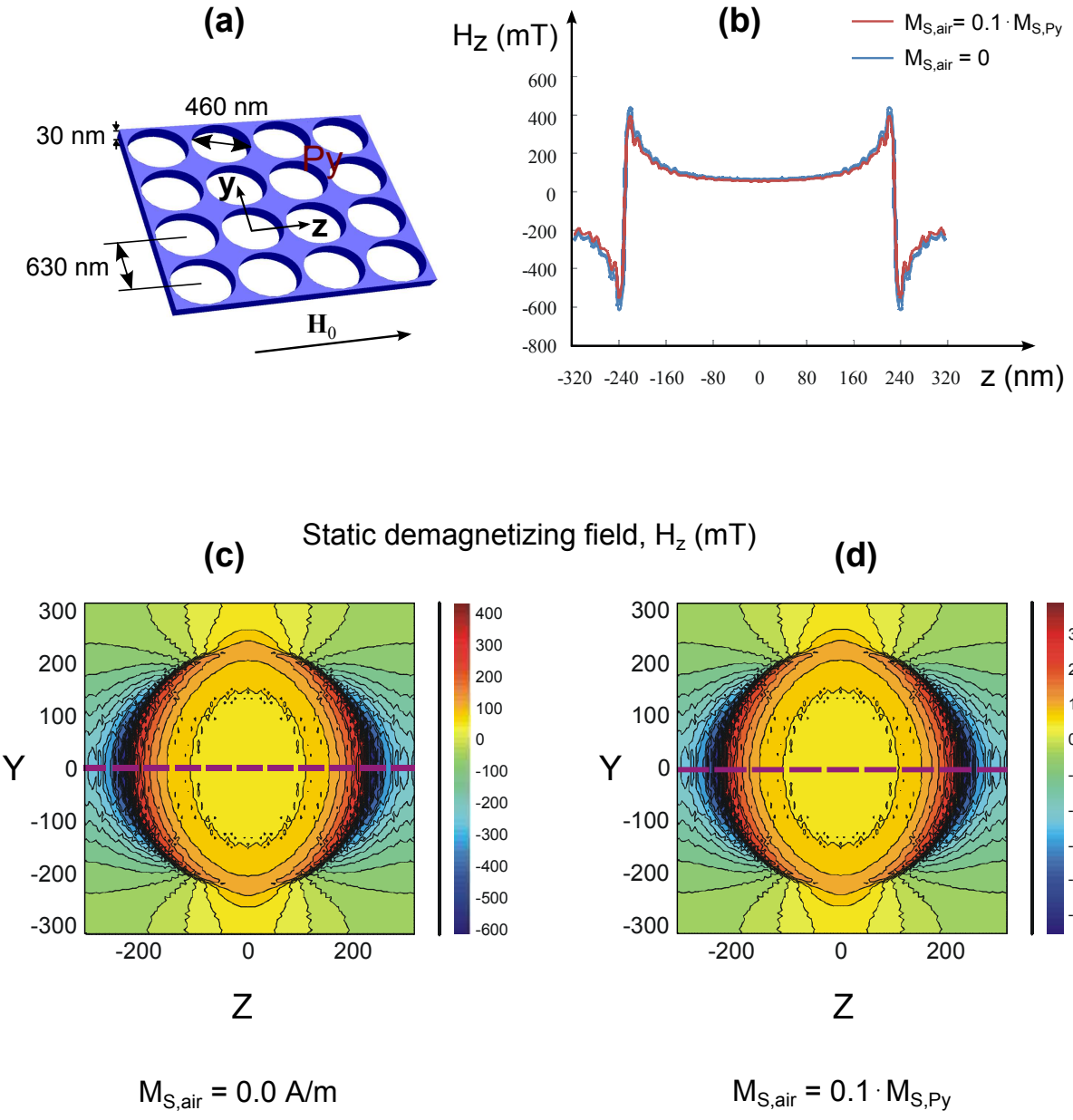

Figure 35. Distribution of the static demagnetizing field in the considered ADL structure calculated according to (55a). (a) Geometry of the studied MC. Diameter of the holes is $2R = 460$ nm, period of the lattice is $a = 630$ nm and thickness of the film is $d = 30$ nm. The saturation magnetization of Py is $M_{\mathrm{S,Py}} = 0.86 \cdot 10^6$ A/m. (b) Comparison of the values of the static component of the demagnetizing field between the cases of purely nonmagnetic material (blue line) of the "holes" with $M_{\mathrm{S}} = 0$ A/m and when the "holes" are modelled as a magnetic medium (red line) with $M_{\mathrm{S}} = 0.1 \cdot M_{\mathrm{S,Py}}$ A/m. Distribution of the static demagnetizing field in a unit cell of the considered ADL structure shown in the cases of purely nonmagnetic material (c) of the "holes" and when they are modelled as a magnetic medium (d) with $M_{\mathrm{S}} = 0.1 \cdot M_{\mathrm{S,Py}}$ A/m.

introduction of an inhomogeneous field of the uniaxial anisotropy along the direction of the applied magnetic field is proposed. By using an appropriate value of this field for the considered structure one can push the nonphysical solutions out of the studied frequency range of the SW spectrum, while frequencies of the other solutions remain unaffected. The detailed analysis of this issue is out of scope of this thesis and a further investigation is required.

The relevance of this formalism goes beyond the system of MCs: similar challenges are encountered in the application of the PWM to the calculation of band structures of phononic crystals consisting of a solid and a liquid or gas [184, 185]. Similarly to the SWs confined to magnetic material in the MC, in phononic crystals transverse vibrations do not occur in constituting liquids and gases. The abrupt vanishing of these vibrations at the border between the solid and the gas leads to nonphysical extra solutions in the PWM.

In summary, the main assumptions of the developed PWM have been verified on the example of a 2D planar MC. In order to cover wider range of possible realizations of the structure the calculations have been performed for the MC comprised of magnetic and nonmagnetic materials. Uniformity of the static component of the demagnetizing field parallel to the external field in the middle of the Py dot and its independence on the position across the thickness of the film has been shown. A good agreement between the results of micromagnetic simulations and analytical calculations has been obtained for the case of the stray field perpendicular to the applied field. The issue of nonmagnetic inclusions in the PWM has been studied. It has been shown that the replacement of the nonmagnetic medium by the magnetic one with ten times lower value of the saturation magnetization than in the bulk material is sufficient to reproduce the shape and value of the static demagnetizing field with a good accuracy. The problem of examining the dynamic component of the internal magnetic field has been discussed.

4. SW interferometer as a promising basic element for the future SW logic devices

The continuing search for new logic paradigms alternative to those based upon semiconductors has led to a suggestion that propagating SWs [47, 50, 51, 186–188] could create basis for such logic devices. In logic elements based on a Mach-Zehnder interferometer, microwave power is split into two waveguide arms containing YIG phase shifters [47, 50, 186]. The phase accumulated by the magnetostatic SWs on their paths to the detector is controlled by applying different dc currents to the arms. Depending upon the induced phase shift, either constructive or destructive interference is observed. The phase shifter could be created by introducing a domain wall [187, 189] or by a local modification of magnetic parameters, e.g., magnetic anisotropy. The challenge is to realize such a barrier that would induce 180° phase shift to the SW while leaving its amplitude unchanged.

The frequency range of the magnetostatic SWs is limited to the tenth of GHz, that makes it impossible to employ these waves as information carriers in nanoscale devices. As the opposite, the exchange SWs, which frequencies lie in the THz range, can offer such possibility of designing and fabrication all-spin-wave logic devices in the nanoscale. However, excitation and detection of the exchange SWs are still challenging.

Here, a theoretical investigation of the exchange SWs scattering by a nonuniformity of the value of the uniaxial anisotropy and/or of the bias magnetic field is performed. The results of this study were published in [55].

Let us consider a SW interferometer shown in Fig. 36(a). The interferometer consists of a SW emission source, a SW waveguide, and a SW detector. The SW guide represents a loop with two arms. One arm (1) represents a stripe of uniform magnetic material and serves as a "reference". The other arm (2) is made of a stripe of magnetic material with a local decrease of the magnetic anisotropy (a "well"), and serves as a SW "phase shifter". The value of the uniaxial anisotropy in the reference arm is equal to β_0, while that in the phase shifter depends upon the coordinate x along the length of the waveguide as

$$\beta = \beta_0 - \frac{\beta_1}{\cosh^2(x/d)}, \tag{75}$$

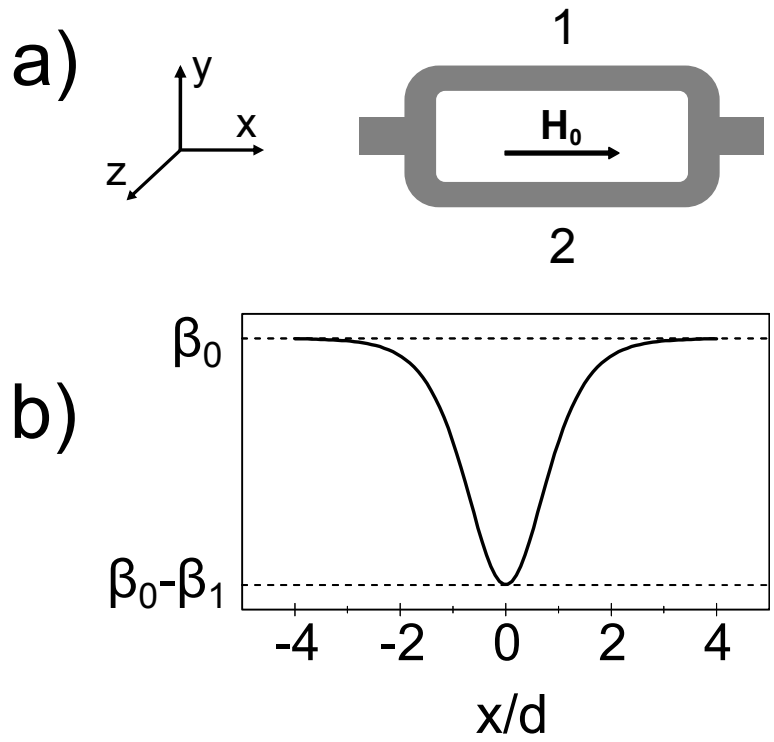

Figure 36. (a) The SW interferometer is shown schematically. The values of the magnetic parameters are constant in the reference arm (1), while the value of the uniaxial magnetic anisotropy in the phase shifter (2) has the profile shown in (b).

where β_1 and d are the "depth" and the characteristic "width" of the well, respectively. The graph of function (75) is shown in Fig. 36(b). The detector receives the total signal which results from interference of the two SWs transmitted through the phase shifter and the reference. The spontaneous magnetization and the exchange parameter are assumed to be equal to the same values M_S and α in both arms, respectively. The discussion below applies to the straight parts of the interferometer only, while the phase shifts induced to SWs within its curved parts are equal in both arms. The easy axis of the uniaxial anisotropy and the directions of the internal magnetic field $\mathbf{H}_0$ and of the static magnetization M_S are all parallel to the $\hat{x}$-axis within the straight regions.

The dynamics of magnetization $\mathbf{M}(x,t)$ is described by the LL equation (29), with the effective magnetic field defined in the exchange approximation as

$$\mathbf{H}_{\text{eff}}(x,t) = [H_0 + M_S\beta(x)]\,\hat{x} + \alpha\Delta\mathbf{M}(x,t). \tag{76}$$

Let us consider small deviations $\mathbf{m}(x,t)$ of the magnetization from the ground state. For this purpose, magnetization can be represented as

$$\mathbf{M}(x,t) = M_S\hat{x} + \mathbf{m}(x,t), \quad \text{where} \quad |\mathbf{m}(x,t)| \ll M_S.$$

Introducing new variables $m_{\pm}(x,t) = m_x(x,t) \pm i m_y(x,t)$ and seeking solutions in the form of harmonic waves $m_{\pm}(x,t) = m_{\pm}(x) \cdot \exp(i\omega t)$, one can obtain the following linearised equation[5]:

$$\frac{d^2 m(x)}{dx^2} + \frac{1}{\alpha}\left(\Omega - \tilde{h} - \beta_0 + \frac{\beta_1}{\cosh^2(x/d)}\right) m(x) = 0, \tag{77}$$

where $\Omega = \omega/\gamma\mu_0 M_S$ and $\tilde{h} = H_0/M_S$ are the dimensionless wave number, frequency, and magnetic field, respectively. This equation can be reduced to the hypergeometrical Gauss equation, whose general solution may be written as [190]

$$\begin{aligned} m(x) = {} & C_1 F\left[0.5(\lambda + ikd);\ 0.5(\lambda - ikd);\ 0.5 - \sinh^2(x/d)\right] \\ & + iC_2 \sinh(x/d)\, F\left[0.5(1 + \lambda + ikd);\ 0.5(1 + \lambda - ikd);\ 1.5;\ -\sinh^2(x/d)\right], \end{aligned} \tag{78}$$

where C_1 and C_2 are arbitrary constants, F is the hypergeometrical function, and λ is determined from equation

$$\beta_1 d^2 = \alpha\lambda(\lambda - 1). \tag{79}$$

The wave number k of the SW propagating in the uniform arm of the studied interferometer is given by

$$k = \sqrt{\frac{\Omega - \tilde{h} - \beta_0}{\alpha}}. \tag{80}$$

Far enough from the well, solution (78) can be asymptotically represented as

$$X(G_j) \sim \begin{cases} e^{ikx} + Re^{-ikx}, & x \to -\infty \\ Te^{ikx}, & x \to +\infty \end{cases} \tag{81}$$

where factors R and T are the amplitude coefficients of reflection and transmission of SWs, respectively, and can be written as

$$R = \frac{\exp\{2i\Theta\} + \exp\{2i\Xi\}}{2}, \qquad T = \frac{\exp\{2i\Theta\} - \exp\{2i\Xi\}}{2}, \tag{82}$$

where Θ and Ξ are given by

[5] For the sake of simplicity the subscript $\pm$ is omitted.

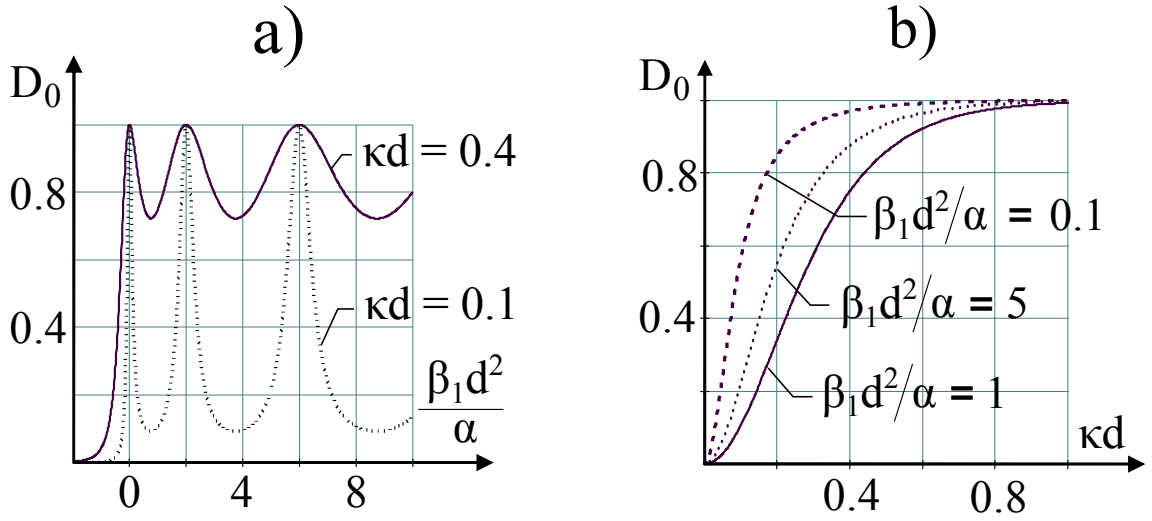

Figure 37. (Copyright © 2007 American Institute of Physics. This figure is taken from [55]) The dependence of the intensity transmission coefficient D_0 upon the wave number of the SW and upon the parameters of the well is shown.

$$\begin{aligned}\Theta &= \arg \frac{\Gamma\left(ikd\right)\exp\left\{-ikd\ln 2\right\}}{\Gamma\left(0.5\lambda+0.5ikd\right)\Gamma\left[0.5\left(1-\lambda\right)+0.5ikd\right]},\\ \Xi &= \arg \frac{\Gamma\left(ikd\right)\exp\left\{-0.5ikd\ln 2\right\}}{\Gamma\left[0.5\left(\lambda-1\right)+0.5ikd\right]\Gamma\left(1-0.5\lambda+0.5ikd\right)}.\end{aligned} \tag{83}$$

Using (82) and (83), for the intensity transmission coefficient $D_0 = |T|^2$, one can obtain

$$D_0 = \sinh^2\left(\pi kd\right)\left[\sinh^2\left(\pi kd\right)+\sin^2\left(\pi\lambda\right)\right]^{-1}. \tag{84}$$

The dependence of D_0 upon the wave number and the parameters of the well are demonstrated in Fig. 37. Note that $D_0 \equiv 1$, when condition

$$\lambda = 1, 2, 3, \ldots \tag{85}$$

is fulfilled, i.e., SWs pass the well without reflection. Well profiles satisfying condition (85) are known as reflectionless Pöschl-Teller well potential[6] [190]. Phases (83) are then related as

$$\Theta - \Xi = \frac{\pi}{2}. \tag{86}$$

Even in the absence of reflection, the phase of the transmitted SW is modified by the well. Therefore, the SW intensity $D_0^{(d)}$ registered by the detector at the output of the

[6] The analogy between propagation of an exchange SW in a nonuniform effective magnetic field and motion of an electron in a nonuniform potential was considered, for example, by E. Schlömann in [191].

interferometer after the interference of the waves transmitted through the phase shifter and the uniform arm has occured is equal to

$$D_0^{(d)} = \frac{1}{4}\left|1+T\right|^2. \tag{87}$$

Using equations (82), (86), and (87), the reflectionless well profiles can be written as:

$$D_0^{(d)} = \sin^2(\Xi). \tag{88}$$

Let us now discuss in some detail the influence of the parameters of the phase shifter, the frequency of the SW, and the applied magnetic field on the output of the interferometer. From equations (82), (83), and (87) it is easy to see that the output is a function of self-similar variables kd and λ. To take advantage of this, let us plot $D_0^{(d)}(kd,\lambda)$ as a 2D grayscale map demonstrated in Fig. 38. In Fig. 38, the black and white regions correspond to a destructive and constructive interference of the SWs from the two arms, respectively. However, a full transmission or a total extinction of the signal can be observed only when the amplitudes of the two SWs are equal, that is only for integer values of λ (horizontal lines), unless the SW in the reference arm is accordingly attenuated. The dependence of $D_0^{(d)}$ upon k (and hence upon Ω, $\tilde{h}$, and β_0) and λ (and hence upon β_1) for the other self-similar parameters fixed is represented by the horizontal and vertical cross sections of the 2D surface $D_0^{(d)}(kd,\lambda)$, respectively. To study the dependence of $D_0^{(d)}$ upon α and d, one has to take into account that both kd and λ depend upon another self-similar variable, α/d^2. Excluding the latter from (79) and (80), one can obtain equation of lines, different points of which are obtained by varying α/d^2 for fixed values of Ω, $\tilde{h}$, β_0, and β_1

$$k^2d^2\beta_1 = \left(\Omega - \tilde{h} - \beta_0\right)\lambda(\lambda-1). \tag{89}$$

The dependences of $D_0^{(d)}$ upon α and d are then represented by the projections of the cross sections of the 2D surface $D_0^{(d)}(kd,\lambda)$ by line (89) upon the vertical and horizontal axes. In doing so, one needs to note that $\alpha = \beta_1 d^2/\lambda(\lambda-1)$

In order to use the interferometer as a magnetic-field-controlled logic element, one must be able to shift from the black to the white along one of the horizontal lines corresponding to an integer λ by varying the value of $\tilde{h}$ and hence kd. The required variation of the bias magnetic field depends upon the derivative

$$\frac{\partial k}{\partial \tilde{h}} = -\frac{\dfrac{\partial \Omega}{\partial \tilde{h}}}{\dfrac{\partial \Omega}{\partial k}} = -\frac{1}{v_g}\frac{\partial \Omega}{\partial \tilde{h}}, \tag{90}$$

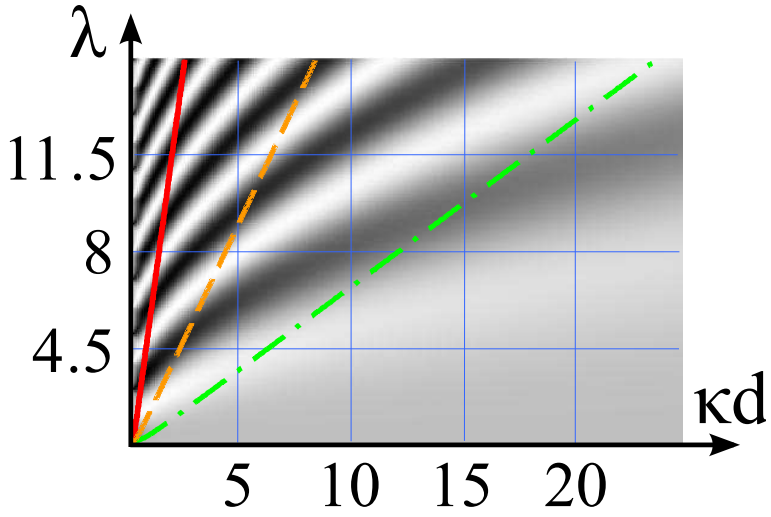

Figure 38. (Copyright © 2007 American Institute of Physics. This figure is taken from [55]) The output of the SW interferometer $D_0^{(d)}(kd, \lambda)$ is plotted as a grayscale map. The white and black regions correspond to 0 and 1, respectively. The dependence of $D_0^{(d)}$ upon k and λ for the other parameters fixed is represented by the horizontal and vertical cross sections of the surface $D_0^{(d)}(kd, \lambda)$, respectively. The dependences of $D_0^{(d)}$ upon α and d are represented by the projections of the cross sections of the surface $D_0^{(d)}(kd, \lambda)$ along curves defined by (89) upon the vertical and horizontal axes. Three such curves are plotted for $\beta_0 = 5$ and $\beta_1 = 1$, while $\Omega - \tilde{h}$ is equal to 5.2 (red, solid), 5.7 (orange, dash), and 7 (green, dash-dot).

where v_g is the group velocity of the SW. For exchange SWs, $\Omega = \tilde{h} + \beta_0 + \alpha k^2$, and so $\partial k / \partial \tilde{h} = -1/2\alpha k$. Thus, the shorter the wavelength of the SW is, the larger is the change of the bias magnetic field required to change the output of the interferometer from "0" to "1", which is also apparent from Fig. 38[7]. This may present a serious limitation for the desired miniaturization of SW logic devices of this type. Furthermore, since the group velocity of SWs appears in the denominator of (90), one may also need to compromise between the efficiency of the magnetic field control and the speed of operation of such a device. Due to the general nature of (90), one may also notice that the most efficient control by the bias magnetic field is achieved for dipole-exchange SWs in the backward volume geometry [168], which have a characteristic minimum in their frequency at a particular finite value of the wave number. For example, magnetostatic backward volume SWs were used in the millimeter-sized SW logic devices from [47]. Alternatively, in a nanoscale device, one could use MCs with periodically modulated magnetic properties instead of the homogeneous materials considered here. In MCs, the dispersion of SWs contains so-called band gaps and regions of reduced group velocity in their vicinity [90, 92, 98]. Hence, the use of MCs within SW interferometers and of SWs with frequency near the bandgap edges as signal carriers could lead to more efficient and miniature SW

[7] Note that the developed theory might fail at longer wavelengths due to the need to take into account the dynamical magnetostatic interaction that is neglected here.

logic devices. However, investigation of such devices is beyond the scope of the present work.

In summary, the scattering of exchange SWs by a localized nonuniformity of the effective magnetic field has been investigated. It has been shown that certain profiles of the effective magnetic field are characterized by a total transmission of the amplitude while inducing large phase shifts required for operation of SW logic devices. At the same time, limitations imposed upon the size and the speed of operation of such devices by a requirement that it be controlled by an external magnetic field have been demonstrated.

Summary

In summary, this thesis presents a study of the spin-wave dynamics in planar periodic magnetic structures. The investigation has been performed by the PWM, suitably adapted for this purpose. The study takes one of the challenges in the PWM-based calculations of the SW spectrum by taking into account the magnetostatic field. Only its dynamic component has been taken into account in the PWM so far. In this dissertation the total magnetostatic field has been calculated analytically for the general case of a planar 2D MC. The obtained result has been successfully implemented, with several approximations, to the PWM calculations of the SW spectrum of the considered structures. The limitations of the developed adaptation of the PWM have been studied and discussed.

Another issue addressed in this thesis is that of nonmagnetic inclusions in the PWM. The assumption of a magnetic medium with a saturation magnetization value ten times lower than in the bulk material, in place of the nonmagnetic inclusions, has been demonstrated to suffice for reproducing the shape and the value of the static demagnetizing field with good accuracy. This simple idea has been applied to the calculations of the magnonic band structure in planar MCs, yielding results in good agreement with experimental data.

The improved method has been tested on many examples of 1D and 2D planar periodic structures and compared with various experimental data. For example, in a 1D MC composed of alternate Py and Co nanostripes in direct contact disposed periodically with a period of 500 nm the observed SWs have been verified to be of magnetostatic nature. The magnetostatic coupling of edge modes in square ADL structures, represented by a homogeneous magnetic film with nanoholes periodically drilled on the surface, has been found to create minibands with strikingly large propagation velocities. This opens up interesting vistas in the field of nanoscale magnonic devices.

The PWM has been adapted for the calculation of the SW spectrum of thin MCs with a metallic screen on top. A significant increase in group velocity of the SWs and a shift of the first bandgap to higher frequencies have been observed in the considered structures. These features could be exploited in a spin-wave Mach-Zehnder interferometer, or other magnonic devices based on the phase shift of SWs.

On the basis of well-known microscopic models the exchange field in composite materials with two or more ferromagnetic constituents in direct contact has been derived in

the linear approximation. For large lattice constants the magnonic band structure proves not to depend on the formulation used, due to the predomination of the magnetostatic interactions over the exchange ones. However, in the range of small lattice constants the bandgap can occur or not in the magnonic band structure, depending on the form of the exchange field. Numerical calculations have shown a close relation between various formulations of the exchange field and the boundary conditions at the interfaces between two ferromagnetic materials. Further investigation is necessary to establish the proper form of the exchange field that would fulfill the physical boundary conditions imposed on the dynamic components of the magnetization vector in MCs.

The continued search for alternative logic paradigms beyond those based on semiconductors has led to the suggestion that propagating SWs could provide a basis of such logic devices. A simple spin-wave interferometer of the Mach-Zehnder type, employing a local nonuniformity of the effective magnetic field, has been proposed and studied in this thesis. The restrictions concerning the size and the operation speed of such a device when controlled with a uniform external magnetic field have been discussed, too.

Bibliography

[1] F. Bloch, Z. Phys. A **61**, 206 (1930).

[2] A. I. Akhiezer, V. G. Bar'yakhtar, and S. V. Peletminskii, *Spin Waves* (Amsterdam, North-Holland Pub. Co, 1968).

[3] A. G. Gurevich and G. A. Melkov, *Magnetization Oscillations and Waves* (CRC-Press, 1996).

[4] T. Holstein and H. Primakoff, Phys. Rev. **58**, 1098 (1940).

[5] F. J. Dyson, Phys. Rev. **102**, 1217 (1956).

[6] J. H. E. Griffiths, Nature **158**, 670 (1946).

[7] J. R. Eshbach, Phys. Rev. Lett. **8**, 357 (1962).

[8] M. Covington, T. M. Crawford, and G. J. Parker, Phys. Rev. Lett. **89**, 237202 (2002).

[9] A. A. Serga, S. O. Demokritov, B. Hillebrands, and A. N. Slavin, Phys. Rev. Lett. **92**, 117203 (2004).

[10] Z. Liu, F. Giesen, X. Zhu, R. D. Sydora, and M. R. Freeman, Phys. Rev. Lett. **98**, 087201 (2007).

[11] V. E. Demidov, M. P. Kostylev, K. Rott, P. Krzysteczko, G. Reiss, and S. O. Demokritov, Appl. Phys. Lett. **95**, 112509 (2009).

[12] Y. Gorobets and S. Reshetnyak, Tech. Phys. **43**, 188 (1998).

[13] S. Reshetnyak, Phys. Solid State **46**, 1061 (2004).

[14] A. V. Vashkovsky and E. H. Lock, Phys.-Usp. **49**, 389 (2006).

[15] S.-K. Kim, S. Choi, K.-S. Lee, D.-S. Han, D.-E. Jung, and Y.-S. Choi, Appl. Phys. Lett. **92**, 212501 (2008).

[16] V. E. Demidov, S. O. Demokritov, D. Birt, B. O'Gorman, M. Tsoi, and X. Li, Phys. Rev. B **80**, 014429 (2009).

[17] S. Choi, K.-S. Lee, and S.-K. Kim, Appl. Phys. Lett. **89**, 062501 (2006).

[18] K. Perzlmaier, G. Woltersdorf, and C. H. Back, Phys. Rev. B **77**, 054425 (2008).

[19] D. R. Birt, B. O'Gorman, M. Tsoi, X. Li, V. E. Demidov, and S. O. Demokritov, Appl. Phys. Lett. **95**, 122510 (2009).

[20] S. O. Demokritov, A. A. Serga, A. André, V. E. Demidov, M. P. Kostylev, B. Hillebrands, and A. N. Slavin, Phys. Rev. Lett. **93**, 047201 (2004).

[21] A. Kozhanov, D. Ouellette, M. Rodwell, S. J. Allen, A. P. Jacob, D. W. Lee, and S. X. Wang, J. Appl. Phys. **105**, 07D311 (2009).

[22] D. D. Stancil, B. E. Henty, A. G. Cepni, and J. P. Van't Hof, Phys. Rev. B **74**, 060404 (2006).

[23] V. Vlaminck and M. Bailleul, Science **322**, 410 (2008).

[24] F. Morgenthaler, IEEE Trans. Magn. **8**, 550 (1972).

[25] M. Bauer, C. Mathieu, S. O. Demokritov, B. Hillebrands, P. A. Kolodin, S. Sure, H. Dötsch, V. Grimalsky, Y. Rapoport, and A. N. Slavin, Phys. Rev. B **56**, R8483 (1997).

[26] V. Veerakumar and R. Camley, IEEE Trans. Magn. **42**, 3318 (2006).

[27] V. E. Demidov, S. O. Demokritov, K. Rott, P. Krzysteczko, and G. Reiss, Phys. Rev. B **77**, 064406 (2008).

[28] A. Kosevich, B. Ivanov, and A. Kovalev, Phys. Rep. **194**, 117 (1990).

[29] Y. Fetisov, C. Patton, and V. Synogach, JETP Lett. **83**, 488 (2006).

[30] M. Wu, P. Krivosik, B. A. Kalinikos, and C. E. Patton, Phys. Rev. Lett. **96**, 227202 (2006).

[31] V. V. Kruglyak and R. J. Hicken, J. Magn. Magn. Mater. **306**, 191 (2006).

[32] S. Neusser and D. Grundler, Adv. Mater. **21**, 2927 (2009).

[33] V. V. Kruglyak, S. O. Demokritov, and D. Grundler, J. Phys. D: Appl. Phys. **43**, 264001 (2010).

[34] M. N. Baibich, J. M. Broto, A. Fert, F. N. Van Dau, F. Petroff, P. Etienne, G. Creuzet, A. Friederich, and J. Chazelas, Phys. Rev. Lett. **61**, 2472 (1988).

[35] G. Binasch, P. Grünberg, F. Saurenbach, and W. Zinn, Phys. Rev. B **39**, 4828 (1989).

[36] P. F. Carcia, A. D. Meinhaldt, and A. Suna, Appl. Phys. Lett. **47**, 178 (1985).

[37] P. F. Carcia, J. Appl. Phys. **63**, 5066 (1988).

[38] A. Saib, D. Vanhoenacker-Janvier, I. Huynen, A. Encinas, L. Piraux, E. Ferain, and R. Legras, Appl. Phys. Lett. **83**, 2378 (2003).

[39] I. L. Lyubchanskii, N. N. Dadoenkova, M. I. Lyubchanskii, E. A. Shapovalov, and T. Rasing, J. Phys. D: Appl. Phys. **36**, R277 (2003).

[40] M. Inoue, K. Arai, T. Fujii, and M. Abe, J. Appl. Phys. **85**, 5768 (1999).

[41] G. Gubbiotti, S. Tacchi, G. Carlotti, P. Vavassori, N. Singh, S. Goolaup, A. O. Adeyeye, A. Stashkevich, and M. Kostylev, Phys. Rev. B **72**, 224413 (2005).

[42] Z. K. Wang, V. L. Zhang, H. S. Lim, S. C. Ng, M. H. Kuok, S. Jain, and A. O. Adeyeye, Appl. Phys. Lett. **94**, 083112 (2009).

[43] Z. K. Wang, V. L. Zhang, H. S. Lim, S. C. Ng, M. H. Kuok, S. Jain, and A. O. Adeyeye, ACS Nano **4**, 643 (2010).

[44] S. Tacchi, M. Madami, G. Gubbiotti, G. Carlotti, H. Tanigawa, T. Ono, and M. P. Kostylev, Phys. Rev. B **82**, 024401 (2010).

[45] S. Neusser, G. Duerr, S. Tacchi, M. Madami, M. L. Sokolovskyy, G. Gubbiotti, M. Krawczyk, and D. Grundler, Phys. Rev. B **84**, 094454 (2011).

[46] S. Tacchi, B. Botters, M. Madami, J. W. Kłos, M. L. Sokolovskyy, M. Krawczyk, G. Gubbiotti, G. Carlotti, A. O. Adeyeye, S. Neusser, and D. Grundler, "Mode conversion from quantized to propagating spin waves in a rhombic antidot lattice supporting spin wave nanochannels," (2012), submitted for publication.

[47] M. P. Kostylev, A. A. Serga, T. Schneider, B. Leven, and B. Hillebrands, Appl. Phys. Lett. **87**, 153501 (2005).

[48] A. Khitun and K. L. Wang, in *Proceedings of the Third International Conference on Information Technology: New Generations*, ITNG '06 (IEEE Computer Society, Washington, DC, USA, 2006) pp. 747–752.

[49] S. Choi, K.-S. Lee, K. Y. Guslienko, and S.-K. Kim, Phys. Rev. Lett. **98**, 087205 (2007).

[50] T. Schneider, A. A. Serga, B. Leven, B. Hillebrands, R. L. Stamps, and M. P. Kostylev, Appl. Phys. Lett. **92**, 022505 (2008).

[51] K.-S. Lee and S.-K. Kim, J. Appl. Phys. **104**, 053909 (2008).

[52] K.-S. Lee, D.-S. Han, and S.-K. Kim, Phys. Rev. Lett. **102**, 127202 (2009).

[53] S.-K. Kim, K.-S. Lee, and D.-S. Han, Appl. Phys. Lett. **95**, 082507 (2009).

[54] A. Khitun, M. Bao, and K. L. Wang, J. Phys. D: Appl. Phys. **43**, 264005 (2010).

[55] S. V. Vasiliev, V. V. Kruglyak, M. L. Sokolovskii, and A. N. Kuchko, J. Appl. Phys. **101**, 113919 (2007).

[56] J. Åkerman, Science **308**, 508 (2005).

[57] J. Joannopoulos, *Photonic Crystals: Molding the Flow of Light* (Princeton University Press, 2008).

[58] H. Grahn, *Semiconductor Superlattices: Growth and Electronic Properties* (World Scientific, 1995).

[59] W. L. Barnes, A. Dereux, and T. W. Ebbesen, Nature **424**, 824 (2003).

[60] M. S. Kushwaha, P. Halevi, L. Dobrzynski, and B. Djafari-Rouhani, Phys. Rev. Lett. **71**, 2022 (1993).

[61] T.-T. Wu, Z.-G. Huang, and S. Lin, Phys. Rev. B **69**, 094301 (2004).

[62] C. Elachi, Proc. IEEE **64**, 1666 (1976).

[63] R. E. Camley, T. S. Rahman, and D. L. Mills, Phys. Rev. B **27**, 261 (1983).

[64] P. Grünberg and K. Mika, Phys. Rev. B **27**, 2955 (1983).

[65] L. Dobrzynski, B. Djafari-Rouhani, and H. Puszkarski, Phys. Rev. B **33**, 3251 (1986).

[66] R. E. Camley and M. G. Cottam, Phys. Rev. B **35**, 189 (1987).

[67] J. Barnaś, J. Phys. C: Solid State Phys. **21**, 1021 (1988).

[68] J. Barnaś, J. Phys. C: Solid State Phys. **21**, 4097 (1988).

[69] B. Hillebrands, Phys. Rev. B **41**, 530 (1990).

[70] R. L. Stamps and B. Hillebrands, Phys. Rev. B **44**, 5095 (1991).

[71] J. Barnaś, Phys. Rev. B **45**, 10427 (1992).

[72] Y. I. Gorobets, Z. A. E., A. N. Kuchko, and K. D. Shedzhuri, Fiz. Tverd. Tela **34**, 1486 (1992), [Sov. Phys. Solid State **34**, 790 (1992)].

[73] B. Li, J. Yang, J.-L. Shen, and G.-Z. Yang, Phys. Rev. B **50**, 9906 (1994).

[74] Y. I. Gorobets, A. N. Kuchko, and R. S. A., Fiz. Tverd. Tela **38**, 575 (1996), [Phys. Solid State **38**, 315 (1996)].

[75] V. A. Ignatchenko, Y. I. Mankov, and A. A. Maradudin, Phys. Rev. B **62**, 2181 (2000).

[76] M. Krawczyk, J.-C. Lévy, D. Mercier, and H. Puszkarski, Phys. Lett. A **282**, 186 (2001).

[77] S. A. Nikitov, P. Tailhades, and C. S. Tsai, J. Magn. Magn. Mater. **236**, 320 (2001).

[78] V. V. Kruglyak and A. N. Kuchko, Physica B **339**, 130 (2003).

[79] V. V. Kruglyak, A. N. Kuchko, and V. I. Finokhin, Phys. Solid State **46**, 867 (2004).

[80] N. Y. Grigorieva and B. A. Kalinikos, Tech. Phys. **54**, 1196 (2009).

[81] A. N. Kuchko, M. L. Sokolovskii, and V. V. Kruglyak, Physica B **370**, 73 (2005).

[82] V. V. Kruglyak, M. L. Sokolovskii, V. S. Tkachenko, and A. N. Kuchko, J. Appl. Phys. **99**, 08C906 (2006).

[83] A. N. Kuchko, M. L. Sokolovskii, and V. V. Kruglyak, Phys. Met. Metal. **101**, 513 (2006).

[84] H. Al-Wahsh, A. Akjouj, B. Djafari-Rouhani, J. O. Vasseur, L. Dobrzynski, and P. A. Deymier, Phys. Rev. B **59**, 8709 (1999).

[85] H. Al-Wahsh, E. H. El Boudouti, B. Djafari-Rouhani, A. Akjouj, T. Mrabti, and L. Dobrzynski, Phys. Rev. B **78**, 075401 (2008).

[86] H. Al-Wahsh, Phys. Rev. B **69**, 012405 (2004).

[87] J. O. Vasseur, A. Akjouj, L. Dobrzynski, B. Djafari-Rouhani, and E. H. E. Boudouti, Surf. Sci. Rep. **54**, 1 (2004).

[88] E. L. Albuquerque and M. G. Cottam, Phys. Rep. **376**, 225 (2003).

[89] P. Monceau and J.-C. S. Lévy, Phys. Letter. A **374**, 1872 (2010).

[90] J. O. Vasseur, L. Dobrzynski, B. Djafari-Rouhani, and H. Puszkarski, Phys. Rev. B **54**, 1043 (1996).

[91] M. Krawczyk and H. Puszkarski, Acta Phys. Pol. A **93**, 805 (1998).

[92] H. Puszkarski and M. Krawczyk, Solid State Phenom. **94**, 125 (2003).

[93] O. Kasyutich, A. Sarua, and W. Schwarzacher, J. Phys. D: Appl. Phys. **41**, 134022 (2008).

[94] O. Kasyutich, D. Tatchev, A. Hoell, F. Ogrin, C. Dewhurst, and W. Schwarzacher, J. Appl. Phys. **105**, 07B528 (2009).

[95] P. Chu, D. L. Mills, and R. Arias, Phys. Rev. B **73**, 094405 (2006).

[96] E. Tartakovskaya, W. Kreuzpaintner, and A. Schreyer, J. Appl. Phys. **103**, 023913 (2008).

[97] M. Krawczyk and H. Puszkarski, Cryst. Res. Technol. **41**, 547 (2006).

[98] M. Krawczyk and H. Puszkarski, Phys. Rev. B **77**, 054437 (2008).

[99] S. S. Kalarickal, P. Krivosik, M. Wu, C. E. Patton, M. L. Schneider, P. Kabos, T. J. Silva, and J. P. Nibarger, J. Appl. Phys. **99**, 093909 (2006).

[100] F. Giesen, J. Podbielski, B. Botters, and D. Grundler, Phys. Rev. B **75**, 184428 (2007).

[101] M. Belmeguenai, T. Martin, G. Woltersdorf, M. Maier, and G. Bayreuther, Phys. Rev. B **76**, 104414 (2007).

[102] G. Gubbiotti, S. Tacchi, M. Madami, G. Carlotti, A. O. Adeyeye, and M. Kostylev, J. Phys. D: Appl. Phys. **43**, 264003 (2010).

[103] A. Borovik-Romanov and N. Kreines, J. Magn. Magn. Mater. **15–18, Part 2**, 760 (1980).

[104] G. Gubbiotti, S. Tacchi, G. Carlotti, N. Singh, S. Goolaup, A. O. Adeyeye, and M. Kostylev, Appl. Phys. Lett. **90**, 092503 (2007).

[105] S. Tacchi, M. Madami, G. Gubbiotti, G. Carlotti, S. Goolaup, A. O. Adeyeye, N. Singh, and M. P. Kostylev, Phys. Rev. B **82**, 184408 (2010).

[106] A. A. Stashkevich, Y. Roussigné, A. I. Stognij, N. N. Novitskii, M. P. Kostylev, G. A. Wurtz, A. V. Zayats, and L. Lutsev, Phys. Rev. B **78**, 212404 (2008).

[107] A. A. Stashkevich, Y. Roussigné, P. Djemia, S. M. Chérif, P. R. Evans, A. P. Murphy, W. R. Hendren, R. Atkinson, R. J. Pollard, A. V. Zayats, G. Chaboussant, and F. Ott, Phys. Rev. B **80**, 144406 (2009).

[108] J. F. Cochran, Phys. Rev. B **64**, 134406 (2001).

[109] V. V. Kruglyak, P. S. Keatley, A. Neudert, R. J. Hicken, J. R. Childress, and J. A. Katine, Phys. Rev. Lett. **104**, 027201 (2010).

[110] W. K. Hiebert, A. Stankiewicz, and M. R. Freeman, Phys. Rev. Lett. **79**, 1134 (1997).

[111] R. J. Hicken, A. Barman, V. V. Kruglyak, and S. Ladak, J. Phys. D: Appl. Phys. **36**, 2183 (2003).

[112] C. Back, D. Pescia, and M. Buess, in *Spin Dynamics in Confined Magnetic Structures III*, Topics in Applied Physics, Vol. 101, edited by B. Hillebrands and A. Thiaville (Springer Berlin / Heidelberg, 2006) pp. 137–160, and references therein.

[113] J. Li, M.-S. Lee, W. He, B. Redeker, A. Remhof, E. Amaladass, C. Hassel, and T. Eimuller, Rev. Sci. Instrum. **80**, 073703 (2009).

[114] P. S. Keatley, V. V. Kruglyak, A. Neudert, M. Delchini, R. J. Hicken, J. R. Childress, and J. A. Katine, J. Appl. Phys. **105**, 07D308 (2009).

[115] M. L. Schneider, J. M. Shaw, A. B. Kos, T. Gerrits, T. J. Silva, and R. D. McMichael, J. Appl. Phys. **102**, 103909 (2007).

[116] C. G. Sykes, J. D. Adam, and C. J. H., Appl. Phys. Lett. **29**, 388 (1976).

[117] P. Kolodin and B. Hillebrands, J. Magn. Magn. Mater. **161**, 199 (1996).

[118] N. I. Polushkin, S. A. Michalski, L. Yue, and R. D. Kirby, Phys. Rev. Lett. **97**, 256401 (2006).

[119] Y. V. Gulyaev, S. A. Nikitov, L. V. Zhivotovskii, A. A. Klimov, P. Tailhades, L. Presmanes, C. Bonningue, C. S. Tsai, S. L. Vysotskii, and Y. A. Filimonov, JETP Lett. **77**, 567 (2003).

[120] T. Maehira, T. Hotta, K. Ueda, and A. Hasegawa, Phys. Rev. Lett. **90**, 207007 (2003).

[121] M. Topsakal and S. Ciraci, Phys. Rev. B **85**, 045121 (2012).

[122] J. O. Vasseur, P. A. Deymier, B. Djafari-Rouhani, Y. Pennec, and A.-C. Hladky-Hennion, Phys. Rev. B **77**, 085415 (2008).

[123] S.-C. S. Lin and T. J. Huang, Phys. Rev. B **83**, 174303 (2011).

[124] M. Krawczyk, J. Kłos, M. L. Sokolovskyy, and S. Mamica, J. Appl. Phys. **108**, 093909 (2010).

[125] R. Skomski, *Simple Models of Magnetism*, Oxford Graduate Texts (Oxford University Press, 2008).

[126] S. Chikazumi and C. Graham, *Physics of Ferromagnetism*, International series of monographs on physics (Oxford University Press, 2009).

[127] M. Sokolovskyy and M. Krawczyk, J. Nanopart. Res. **13**, 6085 (2011).

[128] J. W. Kłos, M. Krawczyk, and M. Sokolovskyy, J. Appl. Phys. **109**, 07D311 (2011).

[129] M. Krawczyk, M. L. Sokolovskyy, J. W. Kłos, and S. Mamica, "On the formulation of the exchange field in the landau-lifshitz equation for spin-wave calculation in magnonic crystals," (2012), accepted for publication.

[130] M. L. Sokolovskyy, J. W. Kłos, S. Mamica, and M. Krawczyk, J. Appl. Phys. **111**, 07C515 (2012).

[131] T. Balcerzak and I. Łużniak, Physica A **388**, 357 (2009).

[132] T. Balcerzak and K. Szałowski, Phys. Rev. B **80**, 144404 (2009).

[133] D. Stancil and A. Prabhakar, *Spin Waves: Theory and Applications* (Springer, 2009).

[134] D. Prather, *Photonic Crystals: Theory, Applications, and Fabrication* (Wiley, 2009).

[135] V. Laude, M. Wilm, S. Benchabane, and A. Khelif, Phys. Rev. E **71**, 036607 (2005).

[136] A. Raman and S. Fan, Phys. Rev. Lett. **104**, 087401 (2010).

[137] R. P. Tiwari and D. Stroud, Phys. Rev. B **81**, 220403 (2010).

[138] S. Neusser, H. G. Bauer, G. Duerr, R. Huber, S. Mamica, G. Woltersdorf, M. Krawczyk, C. H. Back, and D. Grundler, Phys. Rev. B **84**, 184411 (2011).

[139] H. Yang, G. Yun, and Y. Cao, J. Appl. Phys. **111**, 013908 (2012).

[140] V. A. Ignatchenko, H. Kronmüller, and M. Grönefeld, J. Magn. Magn. Mater. **89**, 229 (1990).

[141] G. Rowlands, J. Magn. Magn. Mater. **118**, 307 (1993).

[142] J. Kaczér and L. Murtinová, Phys. Stat. Sol. A **23**, 79 (1974).

[143] T. Mizoguchi and G. S. C. III, J. Appl. Phys. **50**, 3570 (1979).

[144] V. A. Ignatchenko, I. S. Edelman, and D. A. Petrov, Phys. Rev. B **81**, 054419 (2010).

[145] A. A. Kusov, S. S. Jaswal, and Z. S. Shan, Phys. Rev. B **46**, 3123 (1992).

[146] J. Dubowik, Phys. Rev. B **54**, 1088 (1996).

[147] C. S. Lin, H. S. Lim, Z. K. Wang, S. C. Ng, and M. H. Kuok, Appl. Phys. Lett. **98**, 022504 (2011).

[148] V. L. Zhang, H. S. Lim, C. S. Lin, Z. K. Wang, S. C. Ng, M. H. Kuok, S. Jain, A. O. Adeyeye, and M. G. Cottam, Appl. Phys. Lett. **99**, 143118 (2011).

[149] A. Zyuzin, S. Sabaev, and V. Radaikin, Phys. Met. Metal. **102**, 478 (2006).

[150] F. Hoffmann, Phys. Stat. Sol. **41**, 807 (1970).

[151] M. Vohl, J. Barnaś, and P. Grünberg, Phys. Rev. B **39**, 12003 (1989).

[152] J. Barnaś, J. Magn. Magn. Mater. **102**, 319 (1991).

[153] J. F. Cochran and B. Heinrich, Phys. Rev. B **45**, 13096 (1992).

[154] D. L. Mills, Phys. Rev. B **45**, 13100 (1992).

[155] S. Vysotskii, G. Kazakov, Y. Filimonov, and A. Maryakhin, Tech. Phys. **43**, 834 (1998).

[156] C. W. Sandweg, M. B. Jungfleisch, V. I. Vasyuchka, A. A. Serga, P. Clausen, H. Schultheiss, B. Hillebrands, A. Kreisel, and P. Kopietz, Rev. Sci. Instrum. **81**, 073902 (2010).

[157] V. S. Tkachenko, V. V. Kruglyak, and A. N. Kuchko, J. Magn. Magn. Mater. **307**, 48 (2006).

[158] V. S. Tkachenko, V. V. Kruglyak, and A. N. Kuchko, Metamaterials **3**, 28 (2009).

[159] V. L. Zhang, F. S. Ma, H. H. Pan, C. S. Lin, H. S. Lim, S. C. Ng, M. H. Kuok, S. Jain, and A. O. Adeyeye, Appl. Phys. Lett. **100**, 163118 (2012).
[160] S. Seshadri, Proc. IEEE **58**, 506 (1970).
[161] R. E. D. Wames and T. Wolfram, J. Appl. Phys. **41**, 5243 (1970).
[162] W. L. Bongianni, J. Appl. Phys. **43**, 2541 (1972).
[163] T. W. O'Keeffe and R. W. Patterson, J. Appl. Phys. **49**, 4886 (1978).
[164] J. Owens, C. Smith, S. Lee, and J. Collins, IEEE Trans. Magn. **14**, 820 (1978).
[165] G. Duerr, M. Madami, S. Neusser, S. Tacchi, G. Gubbiotti, G. Carlotti, and D. Grundler, Appl. Phys. Lett. **99**, 202502 (2011).
[166] J. Topp, D. Heitmann, M. P. Kostylev, and D. Grundler, Phys. Rev. Lett. **104**, 207205 (2010).
[167] J. Jorzick, S. O. Demokritov, C. Mathieu, B. Hillebrands, B. Bartenlian, C. Chappert, F. Rousseaux, and A. N. Slavin, Phys. Rev. B **60**, 15194 (1999).
[168] B. A. Kalinikos and A. N. Slavin, J. Phys. C: Solid State Phys. **19**, 7013 (1986).
[169] A. V. Chumak, A. A. Serga, B. Hillebrands, and M. P. Kostylev, Appl. Phys. Lett. **93**, 022508 (2008).
[170] A. V. Chumak, T. Neumann, A. A. Serga, B. Hillebrands, and M. P. Kostylev, J. Phys. D: Appl. Phys. **42**, 205005 (2009).
[171] S. Neusser, G. Duerr, H. G. Bauer, S. Tacchi, M. Madami, G. Woltersdorf, G. Gubbiotti, C. H. Back, and D. Grundler, Phys. Rev. Lett. **105**, 067208 (2010).
[172] S. Neusser, B. Botters, and D. Grundler, Phys. Rev. B **78**, 054406 (2008).
[173] M. Kostylev, G. Gubbiotti, G. Carlotti, G. Socino, S. Tacchi, C. Wang, N. Singh, A. O. Adeyeye, and R. L. Stamps, J. Appl. Phys. **103**, 07C507 (2008).
[174] S. Tacchi, M. Madami, G. Gubbiotti, G. Carlotti, A. Adeyeye, S. Neusser, B. Botters, and D. Grundler, IEEE Trans. Magn. **46**, 172 (2010).
[175] S. Tacchi, M. Madami, G. Gubbiotti, G. Carlotti, A. Adeyeye, S. Neusser, B. Botters, and D. Grundler, IEEE Trans. Magn. **46**, 1440 (2010).
[176] M. P. Kostylev and N. A. Sergeeva, in *Magnetic Properties of Laterally Confined Nanometric Structures*, edited by G. Gubbiotti (Transworld Research Network, 2006) pp. 183–207.
[177] M. P. Kostylev and A. A. Stashkevich, Phys. Rev. B **81**, 054418 (2010).
[178] G. Gubbiotti, S. Tacchi, M. Madami, G. Carlotti, A. O. Adeyeye, and M. Kostylev, J. Phys. D: Appl. Phys. **43**, 264003 (2010).
[179] A. Vovk, L. Malkinski, V. Golub, S. Whittenburg, C. O'Connor, J.-S. Jung, and S.-H. Min, J. Appl. Phys. **97**, 10J506 (2005).
[180] A. Barman, J. Phys. D: Appl. Phys. **43**, 195002 (2010).
[181] V. N. Krivoruchko and A. I. Marchenko, J. Appl. Phys. **109**, 083912 (2011).

[182] C. Mathieu, J. Jorzick, A. Frank, S. O. Demokritov, A. N. Slavin, B. Hillebrands, B. Bartenlian, C. Chappert, D. Decanini, F. Rousseaux, and E. Cambril, Phys. Rev. Lett. **81**, 3968 (1998).

[183] T. Fischbacher, M. Franchin, G. Bordignon, and H. Fangohr, IEEE Trans. Magn. **43**, 2896 (2007).

[184] C. Goffaux and J. P. Vigneron, Phys. Rev. B **64**, 075118 (2001).

[185] Y. Pennec, J. O. Vasseur, B. Djafari-Rouhani, L. Dobrzyński, and P. A. Deymier, Surf. Sci. Rep. **65**, 229 (2010).

[186] Y. Fetisov, C. Patton, and V. Synogach, IEEE Trans. Magn. **35**, 4511 (1999).

[187] R. Hertel, W. Wulfhekel, and J. Kirschner, Phys. Rev. Lett. **93**, 257202 (2004).

[188] A. Ustinov and B. Kalinikos, Tech. Phys. Lett. **32**, 353 (2006).

[189] C. Bayer, H. Schultheiss, B. Hillebrands, and R. Stamps, IEEE Trans. Magn. **41**, 3094 (2005).

[190] S. Flügge, *Practical Quantum Mechanics*, Classics in Mathematics (Springer, 1994).

[191] E. Schlömann, J. Appl. Phys. **35**, 159 (1964).